

Copyright © 1996, by the author(s).
All rights reserved.

Permission to make digital or hard copies of all or part of this work for personal or classroom use is granted without fee provided that copies are not made or distributed for profit or commercial advantage and that copies bear this notice and the full citation on the first page. To copy otherwise, to republish, to post on servers or to redistribute to lists, requires prior specific permission.

**DETECTOR AND ELECTRONICS DESIGN
CONSIDERATIONS FOR AN EMISSION-
TRANSMISSION MEDICAL IMAGING SYSTEM**

by

Joseph Anthony Heanue

Memorandum No. UCB/ERL M96/39

24 June 1996

**DETECTOR AND ELECTRONICS DESIGN
CONSIDERATIONS FOR AN EMISSION-
TRANSMISSION MEDICAL IMAGING SYSTEM**

by

Joseph Anthony Heanue

Memorandum No. UCB/ERL M96/39

24 June 1996

ELECTRONICS RESEARCH LABORATORY

College of Engineering
University of California, Berkeley
94720

Abstract

Detector and Electronics Design Considerations
for an
Emission-Transmission Medical Imaging System

by

Joseph Anthony Heanue

Doctor of Philosophy in Engineering - Electrical Engineering
and Computer Sciences

University of California at Berkeley

Professor Bernhard E. Boser, Chair

Radionuclide imaging is a valuable clinical tool with applications in cardiac medicine and cancer diagnosis. Capable of simultaneous x-ray and nuclear-medicine imaging, the emission-transmission computed tomography (ETCT) system is a unique approach to the problems of quantitation and localization in radionuclide measurements. Full realization of the system's potential requires a flexible and practical design of the front-end detector and electronics that takes into account the limitations imposed by physical perturbations. Thus, several front-end improvements are assessed in terms of their benefit for quantitative measurements.

A "triple-mode" detector readout circuit has been designed to provide excellent scatter rejection without sacrificing flexibility. The circuit can be operated in three modes: a slow pulse-counting mode for detection of radionuclide events at low count rates with excellent energy resolution, a fast pulse-counting mode for simultaneous

acquisition of emission and transmission data or for acquisition of dual-energy x-ray data at high rates with moderate energy resolution, and current-mode operation for acquisition of x-ray transmission data. A CMOS prototype demonstrates the feasibility of the triple-mode approach and offers the practical benefits of small size, low cost, and low power consumption.

Although the electronics were designed for a high-purity germanium (HPGe) diode radiation detector, recent attention has been focused on cadmium telluride (CdTe) and cadmium zinc telluride (CZT) detectors. These materials offer room temperature operation, large size, and good stopping efficiency; unfortunately, they also exhibit somewhat limited energy resolution, slow charge transport, and incomplete charge collection. For the ETCT system, it is shown that their most serious limitation is low photopeak efficiency. Thus, three methods for reduction of charge trapping losses are proposed. First, singular value decomposition can be used for post-acquisition processing of spectra. Alternatively, dual time-constant sampling offers real-time trapping correction. Finally, an efficient numerical model predicts that a small-anode geometry yields increased photopeak efficiency.

Next, the benefits of excellent scatter rejection are evaluated. Although scatter introduces a measurable error, the effects of attenuation and collimator blur are more significant. In addition, at an energy resolution of several keV, the error due to scatter is small compared to the statistical uncertainty in quantitative measurements.



Professor Bernhard E. Boser
Dissertation Committee Chair

Acknowledgements

I could not have completed this work without the help of many people. First, I want to thank my research advisor, Bruce Hasegawa. Bruce has let my mind wander in many interesting directions; yet, he has always known when to steer me back along the forward path. I cannot imagine a better role model both as a faculty member and as a person. The rest of my thesis committee has also been very helpful. Stan Prussin has asked countless insightful questions; his imagination and his enthusiasm have been an inspiration. Bernhard Boser helped me learn about integrated circuits and signed dozens of forms as my official advisor. In addition to reading my thesis. David Attwood taught a very enjoyable x-ray physics class.

I also must thank my friends and colleagues at the UCSF Physics Research Lab, especially Keenan Brown, Roger Tang, Steve Blankespoor, Kathrin Kalki, and Xiang Wu. While contributing to my research, they also somehow managed to make it fun to work at an industrial-park lab in South San Francisco.

Genevieve Thiebaut, Mary Byrnes, Ruth Gjerde, and especially Heather Brown Levien deserve thanks for their work in the EE grad office. Without them, I would probably be stuck at Berkeley filling out paperwork for another year.

Len Chen, Mike Goodwin, Tom and Cheryl Donnelly, Sae Woo Nam, and Eliot Mason have helped me more than they realize by diverting me from work. I have also enjoyed trips to the Bay Area by Gail Standish, Hope Cooper, and Pam Keegan.

My family deserves the biggest thanks. The encouragement and support of my Mom and Dad have been a motivation throughout my education. My Aunt Bobbi and Uncle Dan have been supportive and have been kind enough to visit the Bay Area several times. Very special thanks go to my brother John. I have always been able to count on his help and his friendship. It has been great to have him and my

sister-in-law Catherine (with her great sense of humor) across the Bay. Finally. I want to thank my wife Luisa. She has endured trips to lab to fill the cryostats, my weird work hours, and my endless complaints about the Bay-Bridge commute. Her smile has cheered me up after many disappointments. I cannot thank her enough for her love, her friendship, and her support.

This work was supported by grant # 2 R01 CA 50539 from the National Cancer Institute and by a grant from the UCSF Radiology Research and Education Foundation. Funding from the Whitaker Foundation and from the American Heart Association has also supported the UCSF Physics Research Lab during the course of this work.

Contents

List of Figures	viii
List of Tables	x
1 Introduction	1
1.1 Single Photon Emission Computed Tomography	3
1.1.1 Limitations of SPECT	5
1.1.2 Detector and Readout Requirements of SPECT	10
1.2 X-ray Computed Tomography	10
1.2.1 Detector and Readout Requirements of X-ray CT	12
1.3 Emission-Transmission Computed Tomography	13
1.3.1 Description of the Prototype System	14
1.3.2 Limitations	17
1.4 Research Overview	18
2 The “Triple-Mode” Detector Readout Integrated Circuit	21
2.1 Circuit Design	24
2.1.1 The Preamplifier	24
2.1.2 The Slow Pulse Shaper	25
2.1.3 The Fast Pulse Shaper	26
2.2 Experimental Results	27
2.2.1 Implementation History	27
2.2.2 Performance	29
2.3 Discussion	38
3 Behavior of Cd(Zn)Te Detectors	39
3.1 Imaging Characteristics	41
3.1.1 Photopeak Efficiency	41
3.1.2 Scatter-Rejection Capability	47
3.2 Count-Rate Limitations	48
3.2.1 Current Mode Operation	50

3.3	Correction for Charge-Trapping Losses	51
3.3.1	A Singular-Value Decomposition Method	52
3.3.2	A Hardware-Based Scheme	55
3.4	Measurements with CdTe Test Devices	57
3.5	Discussion	57
4	The Role of Device Geometry in Charge Trapping	60
4.1	Detector Model	61
4.1.1	Potential Calculations	64
4.1.2	Radiation Transport	68
4.1.3	Charge Transport	68
4.2	Simulation Results	71
4.3	Conclusion	76
5	Simulation Studies of Scatter	78
5.1	The Physics of Photon Scatter	80
5.2	Simulation Methods	82
5.2.1	Projection Data Analysis of a Myocardial Phantom	82
5.2.2	Image Reconstructions of a Myocardial Phantom	86
5.2.3	Point-Spread-Function Simulations	87
5.3	Results	88
5.3.1	Projection Data Analysis	88
5.3.2	Analysis of Reconstructed Images	91
5.3.3	Point Spread Function Analysis	96
5.4	Conclusion	97
6	Experimental Studies of Scatter	99
6.1	Methods	100
6.2	Results	103
6.2.1	The Concentric Cylinder Phantom	103
6.2.2	The Cold-Lesion Phantom	107
6.2.3	The Thorax Phantom	109
6.3	Scatter Correction vs. Scatter Rejection	112
6.4	Discussion	115
7	Conclusion	117
7.1	Results	117
7.2	Future Work	118
A	Publications	121
	Bibliography	123

List of Figures

1.1	The principle of SPECT imaging	4
1.2	The collimation process	9
1.3	A typical x-ray CT imaging geometry	11
1.4	The ETCT system	15
1.5	ETCT images	17
2.1	Conceptual design of the “triple-mode” circuit	23
2.2	The preamplifier circuit	24
2.3	The slow pulse shaper circuit	25
2.4	The fast pulse shaper	26
2.5	Oscillation in the slow mode operation of the second chip prototype .	28
2.6	Pulse-mode oscilloscope traces	30
2.7	Current-mode waveforms	32
2.8	The count rate limits of the slow and fast modes	33
2.9	Fast and slow mode spectra	35
3.1	Electron and hole transport within a detector	41
3.2	Simulated spectra from Cd(Zn)Te detectors	43
3.3	Electric field geometries	44
3.4	The photopeak efficiency at 140 keV	45
3.5	Photopeak efficiency at 140 keV vs. $\mu_h\tau_h$	47
3.6	CdTe charge collection time	49
3.7	Linear systems spectral representation	52
3.8	The results of SVD trapping correction	54
3.9	The hardware-based correction scheme	55
3.10	Simulated hardware-based correction results	56
4.1	An arbitrary electrode geometry	62
4.2	The strip detector geometry	64
4.3	The strip detector boundary conditions	65
4.4	The discrete column geometry	69

4.5	The calculated weighting potential for a detector with $w = 1$ mm, $s = 1$ mm, and $L = 8$ mm	72
4.6	Simulated spectra from 8 mm-thick detectors with different strip widths and negligible interstrip space	72
4.7	Simulated spectra from detectors with constant strip pitch and different interstrip spacing	74
4.8	Simulated spectra from detectors of different thickness	74
4.9	Temporal signal corresponding to planar and small-anode geometries	76
5.1	The Compton scattering process	81
5.2	The relationship between the scattering angle and the energy of the scattered photon	81
5.3	The angular distribution of Compton scattered photons	82
5.4	The myocardial perfusion phantom	83
5.5	Projection and scatter images corresponding to different energy resolutions	84
5.6	Reconstructed myocardial phantom images	87
5.7	Scatter point spread functions	88
5.8	χ^2 results	89
5.9	Profiles taken from reconstructed images	92
5.10	The effect of various errors on measurements of total myocardial activity and contrast.	93
5.11	Mean activity in the myocardium as a function of system energy resolution.	94
5.12	Statistical uncertainty as a function of ROI size.	95
5.13	The energy resolution required to maintain a given PSF width.	96
6.1	Phantoms used in the experiments	101
6.2	Concentric cylinder phantom images	104
6.3	Activity in the concentric cylinder phantom as a function of energy resolution	105
6.4	Images of the cold lesion phantom	108
6.5	Contrast as a function of lesion size	109
6.6	The SNR as a function of energy resolution for the cold lesion phantom	110
6.7	Images of the thorax phantom	110
6.8	Object widths in the thorax phantom images	111
6.9	Contrast in the cold lesion phantom for scatter rejection and scatter correction	114
6.10	Background noise levels corresponding to scatter correction and scatter rejection	115

List of Tables

3.1	Typical mobilities and trapping lifetimes for CdTe, CZT, and Si. . . .	43
4.1	Calculated photopeak efficiency at 140 keV for various detector parameters	75

Chapter 1

Introduction

Researchers have devised a number of techniques to peer inside the human body. For example, a conventional radiography study measures the attenuation of x rays as they are transmitted through the patient. Because this attenuation depends on the composition of the body tissue, the resulting image reveals anatomical structure. On the other hand, nuclear-medicine imaging involves the measurement of radiation emitted from an *in vivo* pharmaceutical tracer; these images provide a measure of the physiological processes that determine the relative concentration of the tracer. X-ray computed tomography (CT) and single photon emission computed tomography (SPECT) are three-dimensional extensions of planar radiography and nuclear imaging, respectively. Other imaging modalities in routine use include magnetic resonance imaging (MRI), positron emission tomography (PET), and ultrasound.

As medical imaging matures both as a diagnostic tool and as an instrument for monitoring the treatment of disease, there is increasing need for correlation of information from different imaging modalities. Frequently, both anatomical im-

ages (from x-ray CT, MRI, or ultrasound) and physiological data (from SPECT or PET) influence diagnosis. Although a physiological image will reveal the existence of a functional abnormality, an anatomical image is often necessary to identify the afflicted structure. Similarly, as imaging technology improves, there is greater demand for quantitative measures of disease states rather than for simple qualitative images. Indeed, many clinical applications demand both correlation of complementary data and quantitative accuracy. In tumor imaging, for example, assessment of tissue metabolism calls for a quantitative measure of pharmaceutical uptake from a functional imaging technique such as SPECT. At the same time, localization of the malignant tissue requires that the SPECT image be correlated with data from an anatomical imaging technique such as x-ray CT [1]. Similarly, assessment of myocardial perfusion requires that a quantitative measure of blood flow be obtained with a radiotracer technique; however, proper quantitation demands knowledge of the anatomical structure of the thorax [2]. A final example is brain imaging for assessment of neuropsychiatric disorders such as dementia. In this case, functional abnormalities are best quantified by PET, while localization is best achieved by correlating the PET images with data from MRI [3].

The emission-transmission computed tomography (ETCT) system is a unique approach to the problems of image quantitation and image correlation. Capable of simultaneous x-ray CT and SPECT, the ETCT system offers anatomical and physiological imaging with a single instrument. In addition, the x-ray data can be used for correction of several physical perturbations in the SPECT data. Thus, the system offers the potential for improved quantitation.

The goals of this thesis project were threefold. The first was to determine the relative importance of physical perturbations that affect the quantitative accuracy

of ETCT measurements. The second was to investigate electronics and detector technologies that could possibly add to both the quantitative capability and the clinical practicality of the next ETCT prototype. Finally, the third goal was to demonstrate the utility and quantitative performance of an ETCT system configured around the new electronics. The next three sections provide a discussion of the medical imaging background and an explanation of emission-transmission imaging that place these goals in perspective. Following a description of the first ETCT prototype, potential improvements are detailed. Finally, the chapter ends with an overview of the thesis research.

1.1 Single Photon Emission Computed Tomography

In a SPECT study, a radiopharmaceutical is administered to the patient by injection, by ingestion, or through inhalation. In general, the pharmaceutical properties are chosen such that the tracer is metabolized and is accumulated by a single type of tissue. The decay of the radioactive isotope leads to the emission of gamma ray photons of a characteristic energy. For example, ^{99m}Tc , the most commonly used isotope, decays to its ground state by emitting a 140 keV gamma ray with a 6 hour half life. The gamma rays are detected externally with a collimated detector as shown in figure 1.1. The collimator defines the direction of travel of the detected radiation. Nearly all SPECT systems employ an Anger-camera detector, which comprises a sodium iodide (NaI) scintillator coupled to an array of photomultiplier tubes. In order to obtain cross-sectional views of the patient, two-dimensional planar projections are collected at a number of angles. Tomographic image reconstruction is used to transform the two-dimensional projections into a three-dimensional data

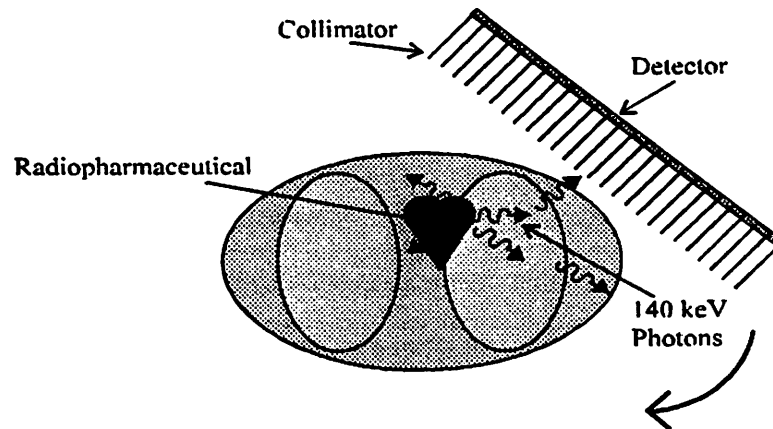


FIGURE 1.1: The principle of SPECT imaging. Gamma rays emitted from an *in vivo* tracer are collected by a collimated detector over a range of angles.

set. (Alternatively, a one-dimensional strip detector can be used to collect the data. In this case, the one-dimensional projections are tomographically reconstructed to form a two-dimensional cross section. The process must be repeated if a full three-dimensional data set is desired.) The image reconstruction can be carried out either with an analytic technique called filtered back projection (FBP) or with iterative numerical techniques. With an iterative technique, an initial estimate of the radionuclide distribution is “projected” forward to generate estimated projection data. This estimated projection data is then compared to the measured data, and a new set of estimated projection data is generated. This new set of projection data is then “back-projected” to obtain a new estimate of the radionuclide distribution. These steps are then repeated until a stopping criterion is satisfied. Although FBP has the advantage of computational simplicity, iterative techniques usually offer greater accuracy since the projector/back-projector pair can realistically model the physical imaging process.

Emission tomography with positron (rather than gamma-ray) emitters is also possible. In PET, decay of the radiotracer leads to the emission and prompt annihilation of a positron. The annihilation produces two 511 keV photons which travel in opposite directions. The detection of these photons in coincidence defines a line along which the decay occurred. Thus, no collimator is necessary.

A number of features make SPECT an attractive diagnostic tool. First, because the distribution of the radiopharmaceutical is a function of biochemical kinetics and flow, the resulting SPECT image provides an indication of patient physiology. Second, SPECT is sensitive to very small concentrations of material; the total mass of radioisotope used in a typical study is a few nanograms [4]. Thus, the use of the tracer does not perturb the system under study. In addition, due to the high tissue specificity of many pharmaceuticals, the image contrast can be significant. Next, while the clinical use of PET is generally restricted to major research institutions, SPECT systems are readily available in small community hospitals. Finally, unlike many positron emitters, single-photon agents are relatively inexpensive, readily available, and do not require an on-site cyclotron. Unfortunately, these advantages are offset by a number of physical perturbations including attenuation, scatter, limited spatial resolution, and photon noise. As a result, image quantitation and image correlation are particularly difficult problems in SPECT.

1.1.1 Limitations of SPECT

Attenuation

The most important physical factor affecting SPECT is the attenuation of photons in the body [5]. Attenuation refers to the loss of photons, either through photoelectric absorption or Compton scattering, as they travel from the radiophar-

maceutical source to the detector. For a typical SPECT study using ^{99m}Tc -labelled pharmaceuticals, the attenuation effect can reduce the number of detected counts to 20-25% of the unattenuated number [6]. As a result, sources deep within the body are imaged with less activity than is actually present. Furthermore, because attenuation is a function of the composition and thickness of the medium, the effect is highly object-dependent. The clinical implications of attenuation can be significant. For instance, the confusion of attenuation artifacts with myocardial defects in cardiac images leads to a 30% rate of false positive diagnoses [7].

There are two classes of algorithms intended to correct for photon attenuation. The algorithms in the first class operate under the assumption that the attenuation coefficient is uniform throughout the volume being imaged. Examples are the Bellini method [8] and the Chang method [9], which apply average attenuation correction factors to the projection data and to the reconstructed images, respectively. Although these methods have the advantage of computational simplicity and work well in brain imaging, they do not work well for imaging the more variable anatomy of the thorax (*i.e.* heart, lung, ribs, and spine). In this case, the second class of algorithms, based on iterative reconstruction techniques, is preferred. Maximum likelihood-expectation maximization (ML-EM) [10] and weighted least squares-conjugate gradient (WLS-CG) [11] techniques fall in this category. These algorithms model attenuation in the projector/back-projector pair based on an object-specific map of the attenuation distribution. This attenuation map can be derived from transmission CT [2] or from correlated MRI [12]. It can also be estimated using segmentation techniques in which the image is divided into regions associated with particular tissue types. In a three-level segmentation, for example, an image pixel may be labelled as either soft tissue, air (*i.e.* lung tissue), or bone.

Scatter

When a Compton scattering event occurs, the original photon is absorbed, and a scattered photon is emitted in a new direction with a corresponding energy loss. Despite their lower energy, scattered photons are detected within the photopeak window due to the finite energy resolution of the detector. The full-width, half-maximum (FWHM) energy resolution of a modern Anger camera is approximately 12-13 keV at 140 keV, and a 20-24 keV energy window is placed around the spectrum photopeak in order to record counts. As a result, 20-40% of the total counts in a typical SPECT study are due to scattered photons [6]. Photon scatter produces long tails in the system point spread function (PSF) that lead to a loss of contrast in the reconstructed images as well as a quantitative error. A discussion of the physics of photon scatter and a detailed analysis of the role of scatter in SPECT imaging are given in chapter 5.

The SPECT literature details many scatter correction algorithms; an overview is given in reference [13]. Perhaps the most commonly used technique is the dual energy window method, in which a fraction of the counts detected in a low-energy scatter window is subtracted from the photopeak projection data on a pixel-by-pixel basis [14]. Unfortunately, because the noise in the two data sets is added in quadrature, the subtraction process increases the noise in the reconstructed images. Another possibility is to include the object-dependent scatter PSF in the projector/back-projector pair of iterative reconstruction algorithms [15]. Although this technique exhibits favorable noise properties, it is computationally expensive. Even more computationally demanding, though potentially more accurate, are techniques that use Monte Carlo methods to estimate the object-dependent scatter during the reconstruction process [16].

Collimator Blur

Although the intrinsic spatial resolution of an Anger camera is on the order of 3-4 mm, the diverging field of view of the collimator introduces a significant loss of resolution. The width of the geometric response function of a typical low-energy, general-purpose (LEGP) collimator at 10 cm from the collimator face is 8.7 mm; it is 6.6 mm for a low-energy, high-resolution (LEHR) collimator [6]. While hampering the delineation of fine details and the separation of small regions of interest in SPECT images, the collimator blurring also complicates the measurement of areas and volumes. Small objects are smeared over a larger volume in image space than their actual volume. The resulting quantitative error is therefore often called the "partial volume effect." In addition, the depth-dependent nature of the blurring leads to artifacts in the reconstructed images. For example, cardiac images taken with an elliptic orbit, which is used to maximize sensitivity, sometimes exhibit wall thickness artifacts that mimic myocardial defects [17].

Researchers have proposed several software post-processing methods to compensate for the collimator response. For instance, stationary Metz and Wiener filters, which assume an average response independent of depth, have been shown to provide some improvement in spatial resolution [6]. More recently, non-stationary, analytic filters have been developed to reduce collimator blur [15]. Also, iterative reconstruction techniques can compensate for image blurring by explicitly modeling the collimator response in the projector/back-projector pair [11]. These iterative techniques tend to give better quantitative results than stationary filters.

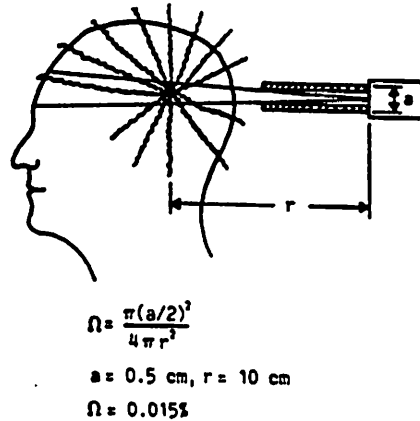


FIGURE 1.2: Collimation is used to localize the activity; the small solid angle leads to poor geometric efficiency.

Noise

Because a collimator must be used to define the direction of detected radiation, SPECT systems have an extremely low geometric efficiency. As figure 1.2 shows, only 0.015% of the emitted radiation is transmitted through the apertures of a typical parallel-hole collimator onto the scintillation crystal [18]. In addition, the total amount of tracer activity is usually limited so that the critical-organ radiation dose to the patient is reasonably low.¹ Also, the fraction of the injected dose that is delivered to the organ of interest can be small due to limited tracer specificity. As a result, SPECT images are “photon-starved”; a typical image contains 5×10^5 photons distributed across 4096 pixels. Although adequately described by Poisson statistics for projection images, the noise is generally amplified by the reconstruction process in the final images [19]. Thus, some form of filtering or statistical signal processing is often applied to suppress noise effects [15].

¹For instance, a 30 mCi intravenous dose of ^{99m}Tc -sestamibi results in an absorbed dose of 4.8 rad to the upper large intestine.

1.1.2 Detector and Readout Requirements of SPECT

For any medical imaging front-end system, the important design parameters include detection efficiency, spatial resolution, energy resolution, and count rate. Because the number of available photons is quite low, SPECT demands large-area detectors with high intrinsic efficiency; a modern Anger camera measures $30 \times 40 \text{ cm}^2$ and has a intrinsic detection efficiency greater than 90% at 140 keV. The blur introduced by the collimator usually dominates any degradation introduced by the intrinsic detector spatial resolution. Thus, the Anger camera's 3 mm spatial resolution is adequate for most applications. Next, photon-counting (pulse-mode) electronics are used to allow the rejection of scattered photons through energy discrimination.² Unfortunately, the Anger camera's energy resolution falls short of the desired performance. As stated above, the 12.5 keV (at 140 keV) energy resolution results in a large number of detected scatter counts. If the energy resolution were improved to 2 keV FWHM, the scatter fraction for a typical study would fall to approximately 7% [21]. Finally, a state-of-the-art gamma camera can achieve count rates in excess of 3×10^5 counts per second (cps) over the face of the detector with approximately 20% dead-time loss. Since the average count rate for a typical SPECT study is limited to approximately 10^4 cps by the amount of injected activity, this count rate performance is acceptable.

1.2 X-ray Computed Tomography

While SPECT is used to investigate physiology, x-ray CT is used to image anatomical structure. In an x-ray CT study, photons ranging from approximately

²A detailed discussion of photon-counting and current-mode detector readout circuits has been presented previously [20].

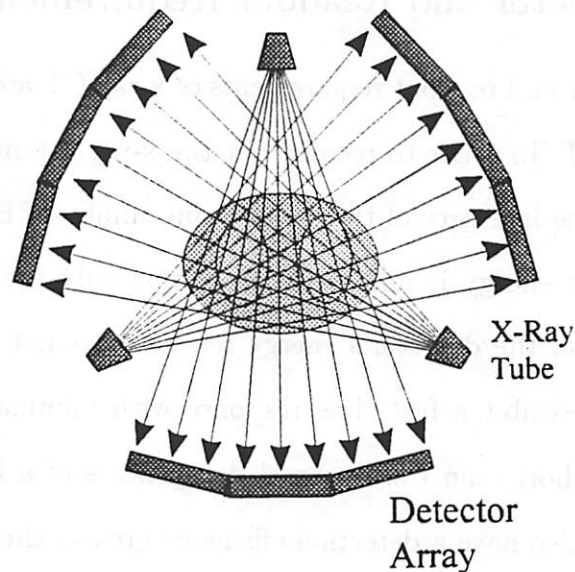


FIGURE 1.3: A typical x-ray CT imaging geometry. Three different angular positions of the x-ray tube and detector are shown.

20 to 120 keV are transmitted through the patient from an x-ray tube to a detector as shown in figure 1.3. As the x-ray beam travels through the patient, some of the photons are attenuated by body tissue. Measurements of the attenuation over a range of angles can be reconstructed with a filtered back-projection algorithm to form a two-dimensional map of attenuation coefficients. Because the attenuation coefficients at a given spot in the body are determined by the tissue composition at that point, the attenuation map represents an image of the patient's anatomy. Because the radiation is directed, there is no need for absorptive collimation to provide position information. Thus, the signal level in x-ray CT is several orders of magnitude higher for a given patient dose than that in SPECT. The increased signal-to-noise ratio allows the use of smaller detectors in order to obtain better spatial resolution. State-of-the-art CT scanners produce images with approximately 1 mm spatial resolution with scan times of 1 sec or less per slice.

1.2.1 Detector and Readout Requirements of X-ray CT

The detector and readout requirements of x-ray CT are somewhat different than those of SPECT. In order to reconstruct the x-ray attenuation map, one needs to measure only the intensity of the x-ray beam; unlike SPECT, knowledge of the individual photon energy is not essential. Thus, only the average detector current is measured, and the detector's energy resolution is not important. However, the detector must exhibit a fast time response with minimal "afterglow" in order to accommodate short scan times; signal decay times of a few μsec are typical. The detector must also have a detection efficiency greater than 90% at diagnostic energies to avoid excess patient dose. Also, the spatial resolution must be good enough to allow sub-millimeter resolution in the reconstructed images. In practice, scintillation crystals such as cadmium tungstate (CdWO_4) meet these requirements at a reasonable cost.

The most stringent demand of x-ray CT is the dynamic range required in the electronics. During a CT study, the peak detector current occurs when there is no patient between the x-ray tube and the detector; the x-ray beam is attenuated only by air. Because x-ray attenuation is exponential, the signal level changes dramatically when a patient is placed in the x-ray path. A typical attenuation along a skull path is on the order of 100 or 200. Through the chest, the attenuation is typically around 10^3 ; the attenuation can be as high as 10^4 through the abdomen of an obese person. In addition, the mathematics of image reconstruction demand that these signal levels be measured with uncertainties in the range of 0.1 to 1%. Thus, many modern CT scanners are designed with a dynamic range of $10^6:1$ [22], although $10^4 - 10^5$ is sufficient for a small laboratory instrument. Fortunately, the bandwidth requirements of x-ray CT are modest. The x-ray signal can change only

as fast as the x-ray tube is rotated around the patient. Thus, signal frequencies are limited to several hundred Hertz.

1.3 Emission-Transmission Computed Tomography

Several groups have proposed creative methods to improve image quantitation and image correlation in SPECT. For example, software image correlation techniques have been used with both CT and MRI images to provide both anatomical markers for localization and attenuation maps for correction of SPECT images [1, 3, 23]. In these "image fusion" studies, the patient is scanned with two separate systems, and the resulting images are superimposed with computational algorithms. These techniques show promise for a range of applications in brain imaging since the skull preserves the anatomical relationships of internal structures; however, their ability to cope with the variable anatomy and physiological motion of the thorax has yet to be proven.

Other groups have mounted an external radionuclide source on conventional SPECT systems to provide transmission CT data [2, 24]. In these systems, the emission detector is used to measure photons transmitted through the patient from the external source as well as emission photons. The transmission data is then reconstructed to form a cross-sectional image of attenuation coefficients as in x-ray CT. Although this technique appears to work well for attenuation correction, the low source flux precludes high-resolution transmission imaging since noise considerations demand an adequate photon density in each pixel. Thus, this method does not offer tremendous improvement in anatomical localization or region-of-interest definition.

The ETCT system is a different approach to the problems of quantitation in SPECT and correlation between x-ray CT and SPECT images. Capable of simultaneous x-ray CT and SPECT, the system employs an energy-dispersive detector array and fast pulse-counting electronics to record both x-ray photons from an external transmission source and higher-energy gamma-ray photons from an internally administered radionuclide source. Energy discrimination circuitry is used to distinguish the emission and transmission photons. The high photon flux from the x-ray tube allows transmission CT images with 1.5 mm spatial resolution. As a result, the transmission images reveal anatomical detail not visible in radionuclide CT. In addition, the x-ray measurements can be used to generate an accurate attenuation map at the radionuclide photopeak energy. The attenuation correction improves the quantitative accuracy of the radionuclide image [25]. Also, the x-ray CT images can potentially be used in region-of-interest (ROI) generation and scatter-correction algorithms to further enhance the quantitative accuracy of the SPECT measurement.

1.3.1 Description of the Prototype System

The ETCT system has been described extensively elsewhere [26, 27, 28], and an overview will be given here. Figure 1.4a shows a block diagram of the ETCT system, and figure 1.4b shows the imaging geometry. The key elements of the system are the detector and associated electronics, the x-ray tube, and the custom-built gantry.

At the heart of the system is a 6 mm-thick, high-purity germanium (HPGe), linear strip detector which has 23 elements and a 2 mm pitch. The advantages of HPGe include a potential energy resolution better than 2 keV and a short 50 nsec charge collection time that allows count rates in excess of 10^6 cps/channel. In order to achieve energy discrimination, the detector is operated in pulse-counting mode in

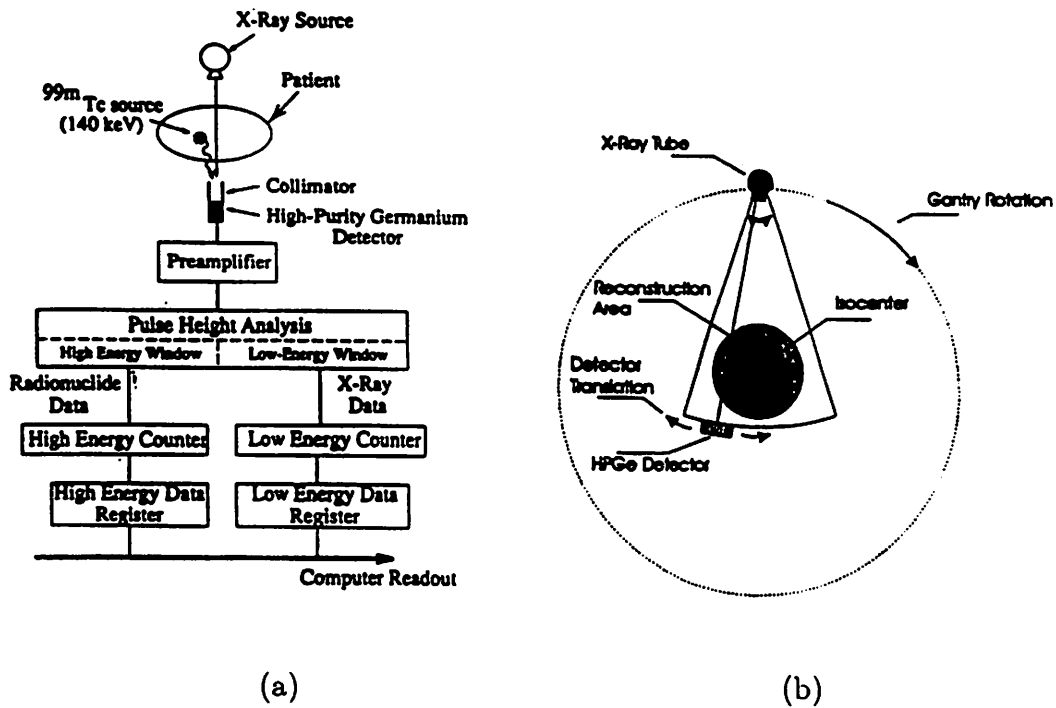


FIGURE 1.4: (a) A block diagram of the ETCT system. A pulse-height analysis circuit is used to distinguish x rays from gamma rays. (b) The ETCT imaging geometry. The detector moves along an arc to simulate a full fan-beam array, and the detector/x-ray tube assembly rotates around the patient to allow tomographic data acquisition.

conjunction with custom-designed, board-level electronics [29]. The pulse-shaping time constant is chosen to match the 50 nsec charge-collection time in order to accommodate the high count rate of the incoming x-rays. The shaped detector signal is delivered to two pulse-height analysis circuits in order to discriminate high-energy radionuclide photons from lower-energy x-ray photons.

Unlike radionuclide transmission sources, the ETCT system's x-ray tube offers high intensity, relatively low cost, and good long-term stability. It is operated at 100 to 120 kVp with approximately 1 mA of tube current. If desired, the beam can be filtered with 0.5 to 1.0 mm of samarium or gadolinium foil in order to produce a bimodal spectrum which is suitable for dual-energy x-ray imaging. In this case, the pulse-height analysis electronics are used to separate low and high-energy x rays rather than to distinguish x rays from gamma rays.

The x-ray tube, detector, and electronics move around the object of interest on a custom-designed gantry with a 22 cm reconstruction circle. Because the detector is only 4.6 cm long, it is translated along a 30° circular arc to achieve a third-generation x-ray CT geometry. The entire x-ray tube and detector assembly is then rotated around the patient for tomographic imaging.

The ETCT system has been tested extensively on both phantoms and animals. Figure 1.5 shows sample images. The spatial resolutions are 1.5 mm and 6 mm for x-ray CT and SPECT, respectively. The ETCT data acquisition system achieves measured count rates up to 10^6 cps/channel with an energy resolution of approximately 15 keV FWHM at 140 keV. The combination of the HPGe detector and the analog electronics should deliver an energy resolution of 7 keV FWHM; however, the system energy resolution is degraded by digital noise coupling through a poorly designed back-plane on the data acquisition boards. Animal studies have shown that

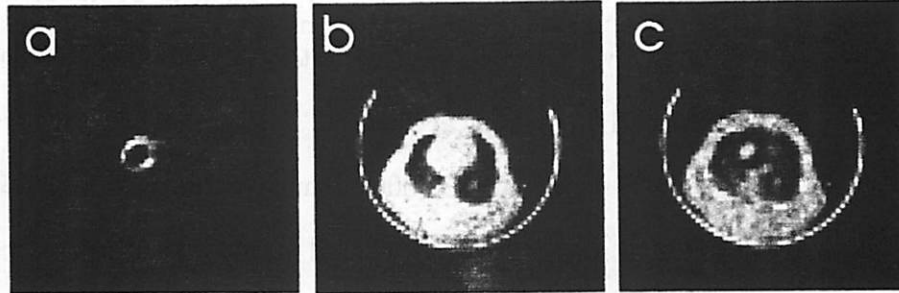


FIGURE 1.5: (a) SPECT image of a pig thorax made with the ETCT system. (b) The correlated x-ray CT image. (c) The two images overlaid.

the ETCT system offers better accuracy for myocardial perfusion measurements than traditional SPECT systems [30].

1.3.2 Limitations

The principal limitations of the ETCT system are imposed by the electronics and by the detector. Configured for x-ray photon counting, the analog electronics sacrifice noise performance in favor of high count rates. Although this type of operation is suitable for simultaneous collection of x-ray and gamma-ray photons or for acquisition of dual-energy x-ray data, it is not optimized for SPECT or x-ray CT alone. Photon counting with excellent energy resolution at low rates is optimum for SPECT, while x-ray CT is generally performed with current-mode detector readout. Improved energy resolution for SPECT would offer increased scatter rejection and presumably better quantitative accuracy. Additional drawbacks of the ETCT electronics include the high cost, large area, and high power consumption associated with the board-level implementation.

The detector also limits the utility of the ETCT system. In particular, HPGe is difficult to fabricate in large areas and is quite expensive. The estimated production

cost for the small detector used in the ETCT system is \$18,000, and a full 300-element detector array would cost approximately \$225,000 [31]. For comparison, the Anger camera head in a typical SPECT system measures 30 cm \times 40 cm, and the cost-of-goods is less than \$30,000 including the photomultiplier tubes and associated readout electronics. An additional drawback of HPGe is the need for liquid nitrogen cooling (77 °K) in order to avoid excess leakage currents. In short, alternative front-end implementations are needed to make the ETCT approach more practical.

1.4 Research Overview

The purpose of this research was to develop approaches to overcome the detector and electronics limitations of the ETCT prototype and to evaluate their clinical utility. Chapter 2 describes the “triple-mode” electronics that were developed in order to provide excellent scatter rejection without sacrificing flexibility. Designed specifically for use with the HPGe detector, the readout circuit can be operated in three different modes. The first provides slow pulse counting for detection of radionuclide events at low count rates with excellent energy resolution. Next, there is a fast pulse-counting mode for simultaneous acquisition of emission and transmission data or for acquisition of dual-energy x-ray data at high count rates with moderate energy resolution. Finally, current mode (or energy integration mode) operation allows fast acquisition of x-ray transmission data. The triple-mode circuit was implemented as an application-specific integrated circuit (ASIC) in a 2 μ m CMOS technology that offers low cost, small size, and low power consumption. The noise performance of the prototype was somewhat worse than expected; yet, the 4 keV energy resolution

that was achieved represents a significant improvement in scatter rejection for the ETCT system. Thus, the new electronics provide both increased capabilities and improved practicality.

Chapter 3 addresses the feasibility of replacing the HPGe detectors with cadmium telluride (CdTe) or cadmium zinc telluride (CZT) detectors. These compound semiconductor materials offer the advantages of room temperature operation, large size, and a high effective atomic number for good stopping efficiency; unfortunately, they also exhibit somewhat limited energy resolution, slow charge transport, and incomplete charge collection. For the ETCT system, it is shown that the most serious limitation of these detectors is low photopeak efficiency for radionuclide imaging. Thus, both software and hardware methods for reduction of charge trapping losses are proposed. Of course, modification of the detector devices themselves is the best method to reduce charge trapping. Chapter 4 discusses the influence of device geometry on trapping behavior.

Next, chapter 5 discusses simulations that investigate the role of scatter rejection in SPECT; in particular, the benefit of the new low-noise electronics is evaluated. The importance of scatter rejection is assessed in relation to attenuation errors, collimator blur, and photon noise. Experimental measurements described in chapter 6 corroborate the simulation results. It is shown that in many cases, scatter is a secondary effect. Attenuation contributes the largest quantitative error, and collimator blur is the primary determinant of spatial resolution and contrast. An energy resolution of several keV is often sufficient to render the scatter error small compared to the statistical uncertainty due to photon noise. In addition, scatter-correction techniques can approach the performance of scatter-rejection methods with better image noise properties.

Finally, chapter 7 summarizes the contributions of this thesis project and presents suggestions for future work.

Chapter 2

The “Triple-Mode” Detector Readout Integrated Circuit

While emission-transmission imaging offers unique capabilities, it also places unique demands on the detector and on the readout electronics. As stated earlier, the ETCT prototype employs a high-purity germanium (HPGe) detector and pulse-counting electronics in order to achieve count rates up to 10^6 cps/channel and an energy resolution of approximately 7 keV. The count rate is sufficient to accommodate the high x-ray flux, and the energy resolution is adequate for discrimination of x rays from higher-energy gamma rays. Thus, the electronics are optimized for truly simultaneous emission-transmission imaging. Simultaneity, however, is not necessarily desirable. Early experiments with the ETCT system revealed that there can be significant contamination of the SPECT data by x-ray pile-up events [32]. Sequential collection of the emission and transmission data can overcome this problem. Note that the entire x-ray scan can be performed before the SPECT scan, or x-ray and gamma-ray data can be collected in sequence during each projection. The latter scheme may provide better image registration. Unfortunately, the electronics are not optimized for the collection of x-ray CT data or SPECT data alone. As discussed in the previous chapter, x-ray CT usually employs current-mode detector

readout, while SPECT calls for relatively slow photon counting.

Three distinct modes of operation are desired for the ETCT electronics. The first mode allows acquisition of radionuclide emission events with excellent energy resolution (≈ 2 keV) in order to provide good scatter rejection. Because emission events are detected at a low rate, the count rate requirements for this mode are modest; only $10^3 - 10^4$ cps are necessary. The second mode of operation permits simultaneous accumulation of x-ray transmission and radionuclide emission events or collection of dual-energy x-ray counts. The energy resolution requirement for this mode is not severe; 6-7 keV is needed to distinguish the two spectral components. However, the count rate must be fast enough - 10^6 cps - to accommodate the high transmission flux. Finally, a third mode of operation offers fast collection of x-ray transmission data. In this case, the instantaneous detector current is measured; there is no need to resolve individual photons. Yet, a dynamic range on the order of 10^5 is necessary due to the exponential variation of the x-ray transmission signal. In short, emission-transmission imaging can utilize three modes of operation: slow pulse counting, fast pulse counting, and current mode.

With conventional components, each mode of operation requires its own circuit with its own operating parameters. For instance, slow pulse mode operation requires a charge-sensitive preamplifier followed by pulse shaping circuitry. The pulse-shaping time constant must be fairly long ($\approx 6 \mu\text{sec}$) to provide the optimum noise performance [33]. The preamplifier must have a high bandwidth, but needs to accommodate only small signal sizes. Next, the fast pulse mode requires a similar circuit; however, the pulse-shaping time constant must be short (≈ 100 nsec) due to the high count rate. Hence, different pulse-shaping circuitry is required. Finally, current mode calls for a transimpedance circuit (an amplifier with a resistor in the

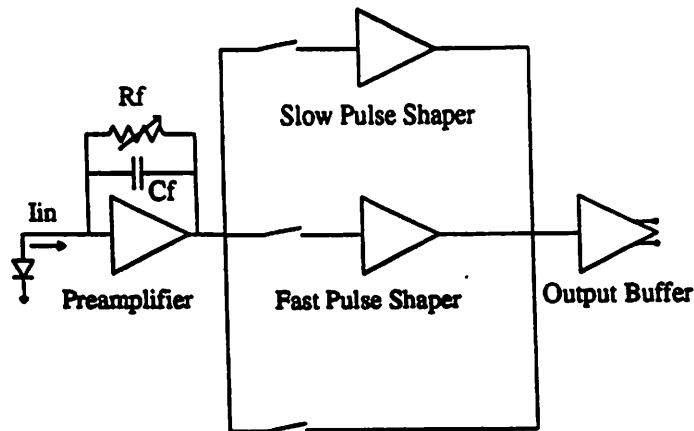


FIGURE 2.1: Conceptual design of the "triple-mode" circuit. Three different pulse-shaping paths provide the required flexibility.

feedback loop). Because the signal changes only as quickly as the x-ray source is rotated around the patient, the required bandwidth is only several hundred hertz.

Although the three modes of operation place different demands on the detector readout, a flexible design can accommodate all three types of measurements. The conceptual design of our "triple-mode" circuit is shown in figure 2.1. A single preamplifier is common to all three modes of operation. For high-frequency pulse-mode signals, the preamplifier functions as a charge-sensitive stage. For low-frequency current-mode signals, the feedback capacitor has little effect, and the preamplifier functions as a transimpedance stage. Next, three different signal paths are provided. In the pulse-counting modes, the signal is passed to a pulse shaper with an appropriate time constant. For current-mode operation, the signal is passed through to the output with no shaping; an external integrator is used to provide low-pass filtering. CMOS switches control the signal flow to the appropriate stage. Finally, a common output stage can be used to drive the signals off-chip. Alternatively, a separate output buffer can be provided for each pulse shaping path. The next section discusses

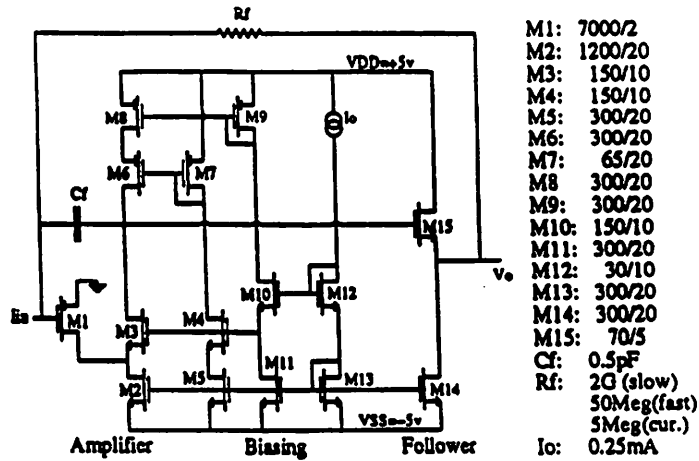


FIGURE 2.2: The preamplifier circuit. The device sizes are shown to the right.

the design of the key circuit building blocks.

2.1 Circuit Design

2.1.1 The Preamplifier

A comprehensive design review is given in reference [20], and only the key design features of each circuit are noted here. Figure 2.2 shows the preamplifier. It is a single-ended folded-cascode amplifier designed for low noise, high bandwidth, and large dynamic range. It can be shown that the total input-referred noise in the preamplifier is minimized if the input capacitance satisfies

$$C_{in,amp} \approx \frac{2}{3} (C_d + C_f + C_p), \quad (2.1)$$

where C_d , C_f , and C_p are the detector, feedback, and parasitic capacitances, respectively [34]. This matching condition determines the size of the input transistor. In addition, transistors $M2$ and $M8$ have long gate lengths to minimize their noise contribution [35]. Next, the transconductance g_m of the input transistor must be

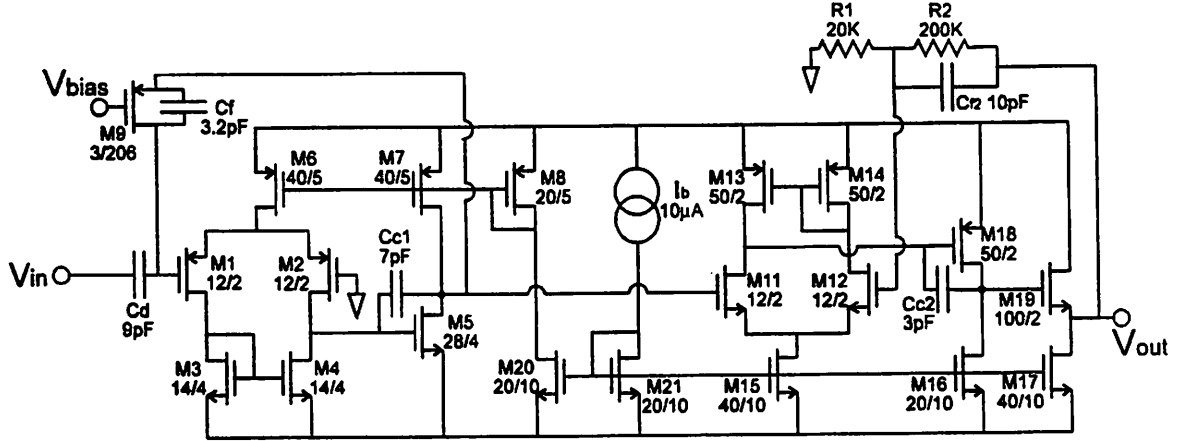


FIGURE 2.3: The slow pulse shaper circuit.

large in order to ensure a fast rise time for the preamplifier output pulse. The bias current in the circuit is chosen such that the rise time is approximately equal to the charge collection time of the detector (50-100 nsec). Finally, the biasing transistors $M10 - M13$ are arranged such that $M2$ and $M5$ are biased near the edge of saturation [35]. This biasing scheme maximizes the output voltage swing of the preamplifier and helps to extend its dynamic range. As a result, the preamplifier can accommodate the large signals encountered in current-mode operation.

2.1.2 The Slow Pulse Shaper

The slow pulse shaper is shown in figure 2.3 [36]; it comprises two amplifier stages. The transfer function of the first stage (devices $M1 - M9$) is

$$\frac{V_{out}}{V_{in}} = \frac{\frac{C_d^2}{g_m} (R_f C_f s - g_m R_f)}{1 + \left(R_f C_f + \frac{C_A}{g_m} \right) s + \frac{R_L}{g_m} C_A (C_f + C_{c1}) s^2} \quad (2.2)$$

where $C_A = C_d + C_{in} + C_{c1}$; R_f is the effective resistance of transistor $M9$, and $g_m = g_{m1} g_{m5}$. This transfer function reduces to that of a differentiator and an

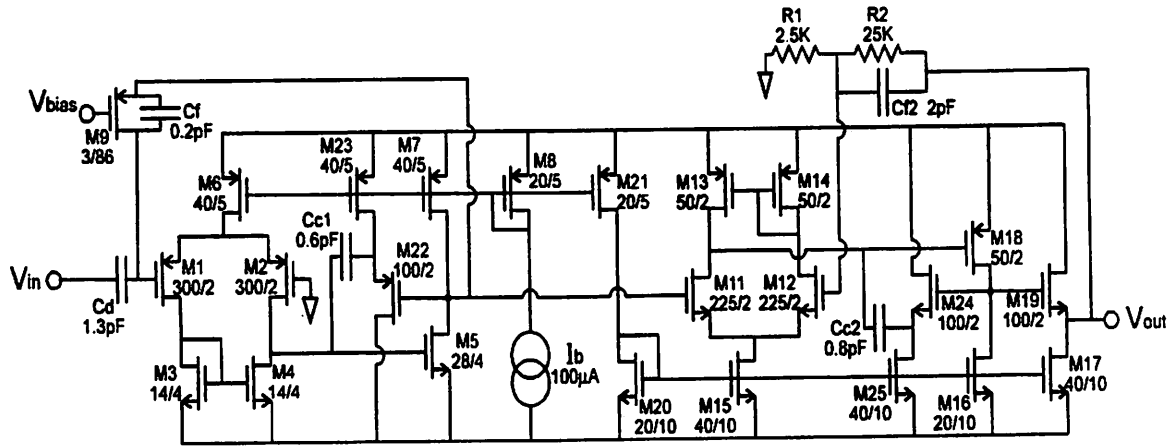


FIGURE 2.4: The fast pulse shaper.

integrator with pulse shaping constant τ_0 under the matching condition

$$\frac{1}{2} \left[R_f C_f + \frac{1}{g_m} (C_d + C_{in} + C_{c1}) \right] = \sqrt{\frac{R_f}{g_m} (C_d + C_{in} + C_{c1}) (C_f + C_{c1})} = \tau_0. \quad (2.3)$$

There is an extra zero at $f = \frac{g_m}{2\pi C_f}$. The gain of the circuit is given by $A_v = \frac{R_f C_d}{\tau_0}$. The second amplifier (devices $M11 - M19$) is effectively an integration stage that extends the peaking time and provides additional gain. The device sizes and bias currents are chosen such that the pulse-shaping (peaking) time τ is near the optimum value of 6 μsec . The width of the shaped pulse can be adjusted by changing the voltage V_{bias} .

2.1.3 The Fast Pulse Shaper

Figure 2.4 shows the fast pulse shaper. Although the circuit topology is essentially identical to that of the slow shaper, the pulse peaking time in this case is approximately 110 nsec. This value permits the use of HPGe detectors up to 1 cm thick in which the charge collection time is approximately 100 nsec; a shorter peaking time would result in signal degradation due to ballistic deficit [37].

Several further details of the design deserve to be noted. First, two source-follower circuits (devices *M22* – *25*) have been added in order to eliminate the feed-forward path through the compensation capacitor [35]. This addition moves the corresponding zero in the frequency response to infinite frequency in order to provide adequate phase margin for high-bandwidth operation. Second, although the second integration stage extends the peaking time, it also produces a shorter tail than a CR-RC shaper with a single integration stage. Finally, the bias currents in this circuit are relatively large in order to avoid slew-rate limiting at the output.

2.2 Experimental Results

2.2.1 Implementation History

The triple-mode circuit was implemented in an Orbit 2.0 μm CMOS process by the MOSIS service [38]. The active area of the chip is approximately 2 mm², and it is contained in a standard 40-pin ceramic dual in-line package. Several iterations were necessary in order to produce a fully working chip. The first version of the chip was completely non-functional for several reasons. For instance, a custom-designed input pad, which was intended to provide electrostatic discharge protection, contained diodes with mismatched leakage currents; the difference current overloaded the first-stage preamplifier. In addition, the power supply and ground routing on the chip did not sufficiently isolate different circuits. Most importantly, the initial fabrication run served mainly as a learning experience. Thus, the chip layout reflected a poor (and quite naive) design methodology in addition to the specific errors.

Although the second prototype chip functioned, it was prone to oscillation at approximately 30 kHz when operated in the slow pulse-counting mode as shown in

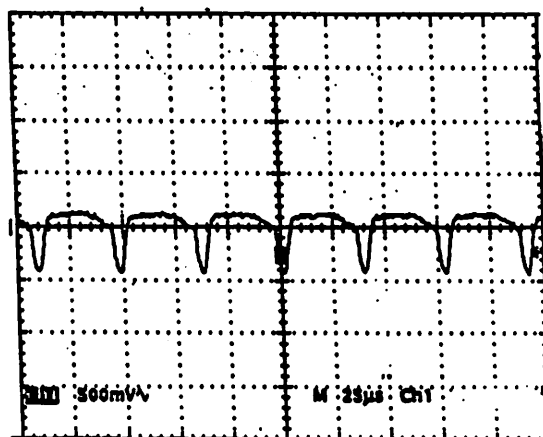


FIGURE 2.5: Oscillation in the slow mode operation of the second chip prototype.

figure 2.5. The most likely cause of the oscillation was positive feedback from the output to the input from parasitic capacitance in the package or on the board. Several observations support this hypothesis. First, the oscillations were very sensitive to the ground pattern on the circuit board. In fact, for two of the four individual chips, the oscillations could be eliminated by placing a grounded copper lid over the entire chip package. In addition, SPICE simulations showed that a 0.5 pF capacitor placed from the output to the input could induce instability.

The third prototype functioned without any tendency towards oscillation. Several considerations in the design process ensured robust operation. First, the slow pulse shaper was implemented with a two-stage design that had somewhat reduced gain.¹ These changes allowed the use of smaller capacitors and transistors with presumably reduced parasitics. Second, a stacked transistor layout methodology was used throughout the chip [39]. Stacked transistors share drain and source connections in order to reduce the required area as well as the associated parasitics.

¹The design shown in this thesis is the final design; the original design has been presented elsewhere [20].

The layout also included the liberal use of guard rings and ground metallization for isolation of circuit elements. Next, the input and output pins were placed on opposite sides of the chip and were carefully shielded. Finally, individual power and ground pins were used to supply each amplifier block (*i.e.* the preamplifier, the two shapers, and the output buffer), and the supplies were decoupled with ceramic capacitors placed close to the chip package.

The investigation of charge-trapping correction schemes for use with CdTe detectors began shortly after fabrication of the third chip prototype. As part of this investigation, the chip was redesigned with a separate output buffer for each signal path in order to ensure compatibility with a hardware-based correction technique that will be described in chapter 4. This fourth prototype implementation allowed investigation of cross-talk effects between the slow and fast pulse shapers. The experimental results described in the next section reflect the performance of this fourth prototype; the behavior of the third prototype is essentially identical.

2.2.2 Performance

In order to investigate the performance of the triple-mode IC, the chip was placed on a custom-designed printed-circuit board and connected to the HPGe strip detector. Because the detector must be kept in a cryostat, a feed-through connector provides the path from the detector to the circuit board. A grounded metal box encloses the circuit board and makes contact with the metal cryostat structure. The detector was irradiated with 122 keV photons from a sealed ^{57}Co source, and waveforms were recorded with an oscilloscope. The top trace in figure 2.6 shows an example of a slow-mode photon pulse on a 10 μsec time scale, and the middle trace is a sample fast-mode photon pulse on a 0.5 μsec time scale. Each waveform

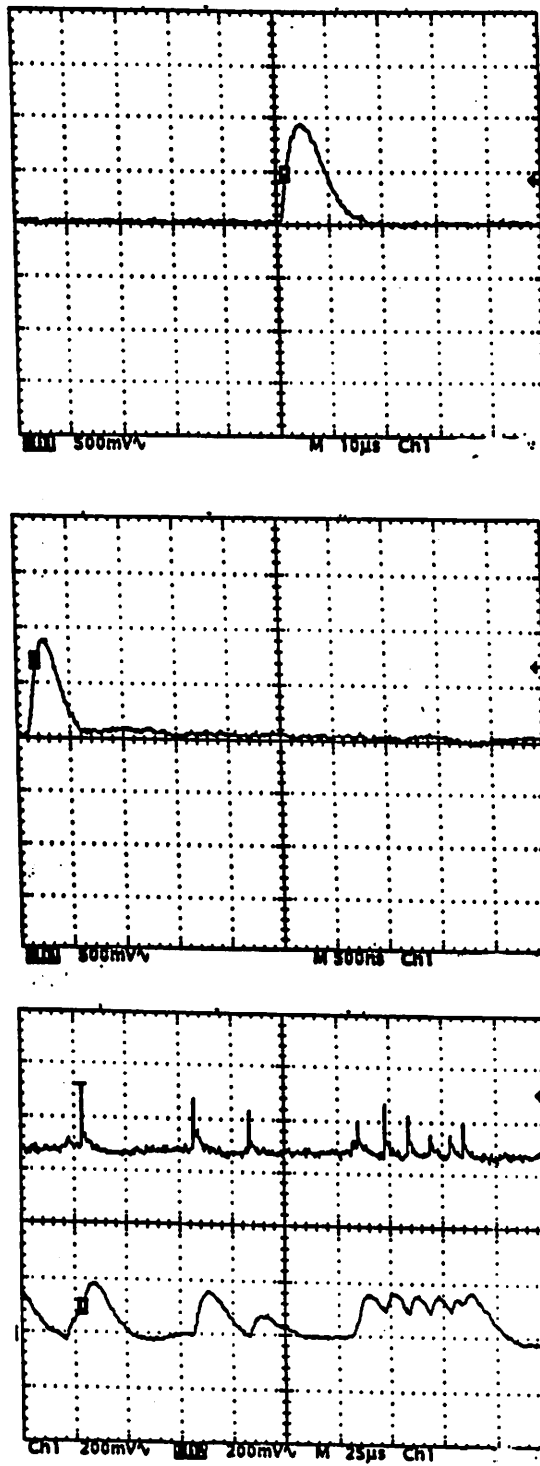


FIGURE 2.6: Pulse-mode oscilloscope traces. The top trace is the response to a 122 keV photon in the slow mode, and the middle trace is the output of the fast mode. The bottom trace shows both modes simultaneously.

was recorded with only a single shaper in the signal path; in other words, the fast and slow modes were not run simultaneously. The rise time of the slow mode signal is approximately 5 μsec ; the fast mode exhibits a 110 nsec rise time. The bottom of figure 2.6 shows waveforms that were recorded while both modes were operating simultaneously. The figure illustrates the essential differences between the two modes of operation. Although the fast mode can separate closely spaced pulses, its noise level is higher than that of the slow mode. The figure also reveals an unexpected design flaw in the chip. Simultaneous operation of the two modes introduces a long tail in the fast mode pulse. Presumably, the slow pulse shaper's differentiation capacitor represents an excess load at the input of the fast pulse shaper. This flaw can be corrected in a future implementation by placing buffer amplifiers between the preamplifier output and the shaper inputs.

Figure 2.7 shows waveforms recorded during current-mode operation. The top trace represents the response to a single test pulse from an external signal generator. The fast rise and slow decay of the preamplifier output is clearly evident. The bottom signal is the response to randomly spaced test pulses at approximately 25 MHz. At this high rate, pulse counting is impossible; yet, the current mode operation reveals the time variation of the detector signal.

Count Rate

The count-rate capabilities of the two pulse-counting modes will be determined by the back-end electronics used to process the shaped signals. Since suitable high-rate back-end electronics were not available in the laboratory, count-rate measurements were impossible. However, the width of the shaped pulse represents a fundamental limit to the count rate which can be estimated under the assumption that

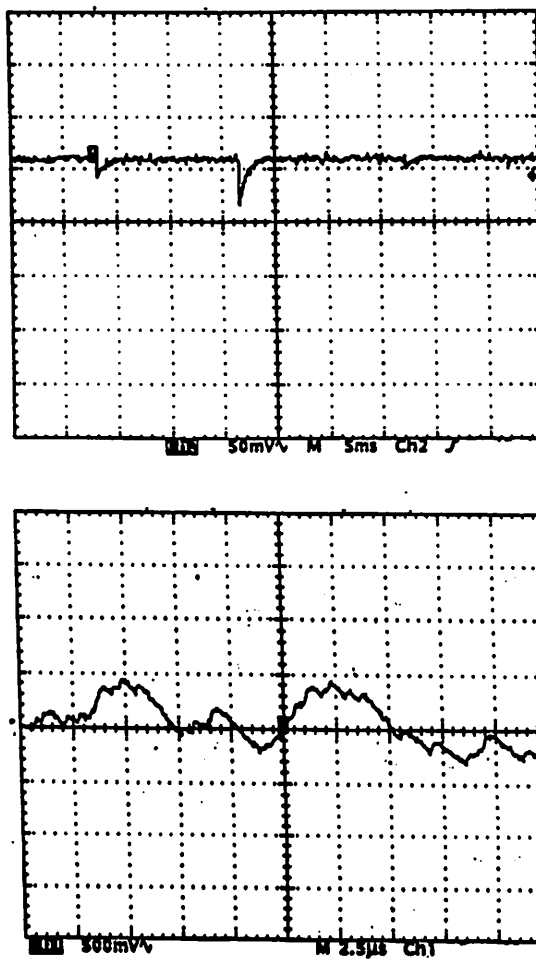


FIGURE 2.7: Current-mode waveforms. The top trace shows the response to an isolated test pulse, and the bottom trace is the output in response to randomly-spaced test pulses at approximately 25 MHz.

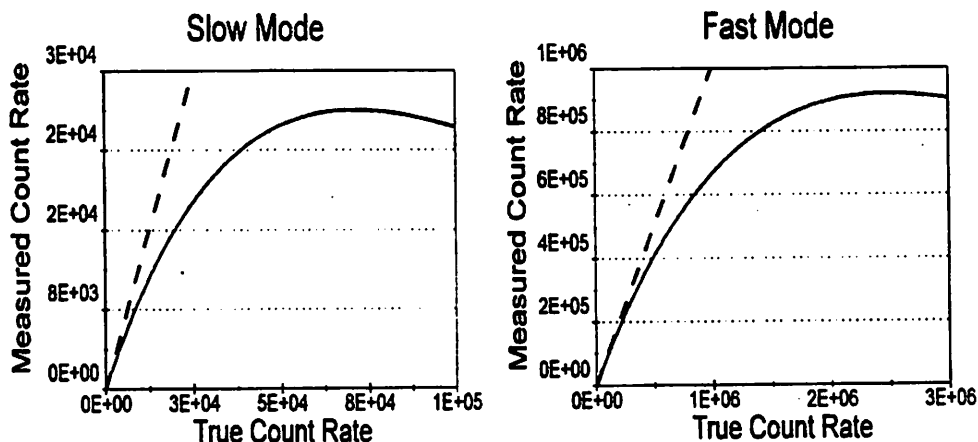


FIGURE 2.8: The count rate limits of the slow and fast modes assuming a paralyzable model. The dashed lines represent the count rate without dead-time losses.

the back-end electronics contribute no dead time to the measurement. In this case, the pulse shaper represents a paralyzable system. In other words, a true interaction occupies the electronics for some dead time τ . The value τ is approximately equal to the full width of the shaped pulse. Although any event that occurs during this dead time is lost due to pulse pile-up, the event extends the dead time by another period τ following the lost event. The relationship of the measured count rate m to the true interaction rate n is given by [37]

$$m = ne^{-n\tau}. \quad (2.4)$$

With $\tau = 14 \mu\text{sec}$ and $\tau = 400 \text{ nsec}$ for the slow and fast modes respectively, equation 2.4 yields the graphs shown in figure 2.8. The maximum count rate is approximately 2.6×10^4 cps for the slow mode and 9.2×10^5 cps for the fast mode. Of course, the experimental maximum count rates may be somewhat lower due to the inherent delay of the back-end electronics. The present analysis is intended merely as an order-of-magnitude estimate of the count-rate limitations.

Noise

As a preliminary estimate of the noise performance of the chip, the slow mode noise level was measured with the chip and circuit board disconnected from the detector and placed in an isolated test box. The chip input was left open-circuited and was loaded with a 20 pF capacitor to simulate the capacitance of the detector and cryostat feed-through connectors. An rms voltmeter was used to measure the noise at the output of the chip. Because the overall gain of the circuit was known from previous measurements, this noise voltage was easily converted to an energy resolution in units of keV. The measurement yielded a voltage noise equivalent to 2.4 keV. Addition (in quadrature) of an estimated 0.9 keV from detector shot noise and 0.6 keV from quantum noise² yields an energy resolution estimate of 2.6 keV FWHM at 122 keV, which is higher than the 2.0 keV noise level predicted by SPICE simulations.

In order to measure more accurately the noise performance in both pulse modes, the chip was returned to the system. The detector was irradiated with a ⁵⁷Co source, and the shaped signals were fed off-board through a discrete line-driver to a multi-channel analyzer (MCA), which recorded the pulse-height spectrum of the shaped pulses. Figure 2.9 shows sample spectra for both the slow and the fast mode. A spectrum from a General Electric 600 XR/T scintillation camera is also shown for comparison. The full width of the 122 keV line measured at half of its maximum

²As discussed in reference [20], the noise in a nuclear pulse counting system arises from four basic sources: series noise, parallel noise, flicker noise, and quantum noise. The rms noise figures corresponding to these component noise sources are added in quadrature to determine the overall system noise. Thermal noise in the input transistor dominates the series noise. Next, parallel noise comprises both detector shot noise and thermal noise in the feedback resistor. Finally, flicker noise is generated in the input transistor, and quantum noise arises from the discrete production of charge carriers within the detector. The 0.9 keV shot noise estimate is taken from the earlier analysis.

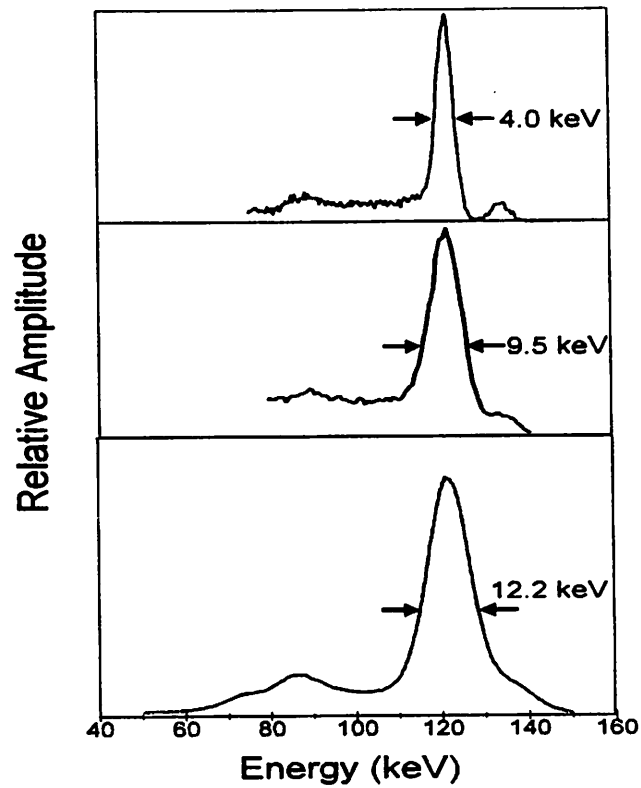


FIGURE 2.9: The top figure shows a spectrum made from the slow-mode response to a ^{57}Co source, and the middle figure shows the fast-mode response. A spectrum from a GE gamma camera is shown for comparison.

value provides a measure of the system energy resolution. The triple-mode chip achieves approximately 4.0 keV and 9.5 keV FWHM energy resolution in the slow and fast modes, respectively. These values are higher than the 2.0 keV and 6.3 keV predicted from SPICE simulations. Although the noise is somewhat higher than expected, the energy resolution of the system exceeds that of a standard gamma camera. Note that the 136.5 keV ^{57}Co line is easily distinguished in the slow-mode spectrum, but blends into the 122.1 keV line in the Anger camera spectrum.

To determine the noise level during current-mode operation, the chip output was passed through a discrete low-pass filter with a -3 dB bandwidth of 500 Hz to an rms voltmeter, and the output voltage with no input signal was recorded. A signal-generator input was then used to determine the maximum signal amplitude that could be measured. The ratio of these values yielded a signal-to-noise ratio (SNR) of approximately 5×10^4 . Once again, the measured noise exceeded that predicted by simulations, which gave a SNR of 10^5 .

Thus, there is a discrepancy among energy resolution estimates derived from simulations, from measurements made on the chip in isolation, and from measurements made with the chip connected to the detector. Several possible factors can explain this discrepancy. First, the noise model used in SPICE is inaccurate for very large transistor sizes [40]. In particular, the resistive polysilicon gate and the substrate contribute small amounts of excess noise. Second, spurious noise pick-up was not modeled in the simulation. The use of the standard DIP package of the test chips tends to increase noise coupling due to increased parasitics. It is possible that chip-on-board (COB) construction would yield better performance through both reduced lead lengths and placement of circuitry closer to the board ground plane [41]; COB construction also might have eliminated the oscillation problems that plagued

the second chip prototype. In addition, the circuit board material influences circuit performance. While the board was fabricated using standard FR4 epoxy resin, other groups have found it necessary to use Teflon in order to reduce excess flicker noise [42]. Next, the parasitic capacitance at the input was estimated to be 20 pF in the simulations. Because the capacitance arises from a distributed structure of wires and connectors, its value is difficult to measure; the original estimate may have been somewhat low. Finally, the grounding pattern of the cryostat assembly strongly influences the noise performance. In particular, both the amplifier power supply and the detector bias supply provide ground connections. Because these grounds are connected both through the cryostat assembly and at earth ground, excess noise can arise from two sources. First, a ground loop leads from earth ground to the detector ground, through the cryostat assembly to the amplifier ground, and back to earth ground through the amplifier power supply. The distributed structure of the cryostat assembly also leads to smaller ground loops since there are multiple connection points between the detector ground and the amplifier ground. These ground loops can radiate noise into the system. Next, the multiple connections between the amplifier ground and the detector ground produce a shared ground path. Any voltage drop along this path leads to the injection of noise charge from the detector into the amplifier electronics. Unfortunately, the cryostat was sealed when the detector was shipped from the European vendor; so, a thorough investigation of the internal grounding patterns was impossible. All in all, the grounding pattern is one of a number of factors that should be considered in a careful re-engineering of the triple-mode system implementation in order to improve the noise performance.

2.3 Discussion

The implementation of the triple-mode IC has achieved many of the original design goals. First, although the noise performance of the chip is somewhat less than the design specifications, the energy resolution of the system far exceeds that of a standard gamma camera. Thus, the achieved performance permits investigation of scatter rejection in SPECT as described in chapters 6 and 7. Next, it is clear that integrated-circuit technology provides enough flexibility to meet the conflicting requirements of emission-transmission imaging. In addition to the increased functionality, the new IC electronics are less expensive, consume less power, and occupy a smaller area than the original discrete ETCT electronics.

Chapter 3

Behavior of Cd(Zn)Te Detectors

When the original ETCT prototype was developed, high-purity germanium was an obvious choice as a detector material offering the potential for excellent energy resolution and high count rates. The high cost and the need for liquid nitrogen were viewed as unavoidable. In recent years, however, research into compound semiconductor materials has advanced significantly. In particular, cadmium telluride (CdTe) and cadmium zinc telluride ($\text{Cd}_{1-x}\text{Zn}_x\text{Te}$ or simply CZT) offer several potentially attractive features as detector materials both for the ETCT system and for medical imaging in general. While the large bandgap of these materials allows room temperature operation, recent improvements in fabrication processes permit development of large-area arrays with excellent spatial resolution [43, 44]. In addition, the high effective atomic number (50) results in good stopping power. Unfortunately, these advantages are offset by several major limitations. First, both CdTe and CZT (referred to collectively as Cd(Zn)Te) suffer from carrier recombination and trapping which lead to incomplete charge collection. The resulting spectra exhibit low-energy “tailing” that reduces the photopeak efficiency. Next, since Cd(Zn)Te detectors ex-

hibit relatively large leakage currents, their intrinsic energy resolution is not as good as that of silicon or germanium. Because CdTe tends to have a larger hole mobility and longer hole lifetime as well as higher leakage currents than CZT [44], spectra from CdTe devices are generally characterized by less tailing but greater photopeak broadening than those from CZT detectors. Finally, the behavior of these materials can be highly temperature dependent.

In order to gauge the suitability of these detectors for medical imaging, their behavior was simulated for the three modes of operation of the ETCT system. In addition to emission-transmission imaging, all three modes of operation are used independently in important potential applications of Cd(Zn)Te and must be differentiated in any analysis of these materials for medical imaging. For example, Cd(Zn)Te may be used in the slow pulse counting mode for a mobile SPECT system or for a small mammographic radionuclide imager. Alternatively, fast pulse counting with linear arrays of these detectors would be appropriate for bone densitometry systems. Finally, Cd(Zn)Te operated in current mode would offer an attractive "direct-detection" alternative to the scintillator-photodiode detectors used in current x-ray CT systems.

The detection efficiency, scatter-rejection capabilities, count-rate performance, and current-mode behavior of Cd(Zn)Te detectors were simulated within the context of these applications. This chapter discusses the results of these simulations; it is shown that the most significant limitation of these detectors is the loss of photopeak efficiency due to charge trapping. Therefore, the next part of this chapter introduces two techniques to overcome trapping losses. Finally, there is a brief discussion of experimental measurements made on prototype devices.

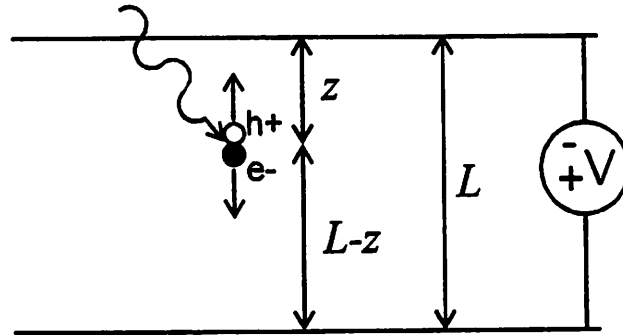


FIGURE 3.1: A conceptual diagram of electron and hole transport within a detector.

3.1 Imaging Characteristics

3.1.1 Photopeak Efficiency

Because the number of available photons is low, radionuclide imaging demands excellent detection efficiency. The EGS4 Monte Carlo Code [45] was used in a simulation to investigate the effective detection efficiency with various degrees of charge trapping. The simulation calculates the detector response to a beam of incident 140 keV photons distributed uniformly on the face of $2\text{ mm} \times 2\text{ mm}$ detector elements of varying thickness. (A detector pitch of 2 mm is currently used in the ETCT system.) The detectors are assumed to have a metal-semiconductor-metal (rather than a p-i-n) structure.¹ The simulation includes losses due to transmission, K x-ray escape, and Compton photon escape. A photon interaction at depth z produces electrons and holes which travel in opposite directions under the applied field as shown in figure 3.1. The fraction of deposited charge that is actually detected

¹In general, m-s-m structures yield better spectroscopic performance than p-i-n structures since it has proven difficult to fabricate high-quality n-type material in CdTe. In addition, most of the processes used to produce p-i-n devices are incompatible with high pressure Bridgeman growth, the technique of choice for production of high-quality CZT.

is computed from the Hecht relation [46]:

$$\frac{Q}{Q_0} = \frac{\mu_e \tau_e \xi}{L} \left(1 - e^{-\frac{(L-z)}{\mu_e \tau_e \xi}} \right) + \frac{\mu_h \tau_h \xi}{L} \left(1 - e^{-\frac{z}{\mu_h \tau_h \xi}} \right). \quad (3.1)$$

Q is the detected charge, and Q_0 is the amount of charge produced in the detector. The subscripts e and h denote electrons and holes; μ is the carrier mobility; τ is the mean time before trapping; ξ is the electric field, and L is the detector thickness. The Hecht model is an approximation that assumes a uniform probability of trapping per unit of distance travelled, which leads to the exponential behavior. Additional assumptions include a constant electric field, an isolated detector with lateral dimensions that are comparable to L , and no detrapping. Although more accurate models that account for electric-field variations [47, 48] and small pixel sizes [49] have been developed, the Hecht relation is adequate to describe the qualitative behavior of detectors in which the lateral dimension is comparable to the thickness.² Once the Monte Carlo transport code determines a deposited energy, the Hecht relation yields the detected energy. By repeating the calculation for many photon interactions, a detected spectrum is generated. The calculated efficiency is then defined as the fraction of the incident photons that are detected within an energy window centered around the photopeak. The energy window width is assumed to be twice the full-width, half maximum (FWHM) energy resolution.

The simulation was repeated for various combinations of detector parameters. In particular, since the values of the hole mobility and the hole lifetime determine the amount of charge trapping, a range of $\mu_h \tau_h$ values was used. Table 3.1 shows typical parameters for CdTe and CZT; the values for silicon at room temperature are provided for comparison. All of the detector parameters used in this work

²Chapter 4 presents a detector model which is quantitatively accurate for devices in which the lateral dimension is much smaller than the detector thickness.

Material	$\mu_e \left(\frac{\text{cm}^2}{\text{V}\cdot\text{sec}} \right)$	$\mu_h \left(\frac{\text{cm}^2}{\text{V}\cdot\text{sec}} \right)$	τ_e (sec)	τ_h (sec)
CdTe	1100	80 – 100	$9 \times 10^{-7} - 4 \times 10^{-6}$	$1.3 \times 10^{-7} - 4 \times 10^{-6}$
CZT	1100	80 – 100	$9 \times 10^{-7} - 3 \times 10^{-6}$	$8 \times 10^{-8} - 9 \times 10^{-7}$
Si	1350	480	2×10^{-5}	2×10^{-5}

TABLE 3.1: Typical mobilities and trapping lifetimes for CdTe, CZT, and Si.

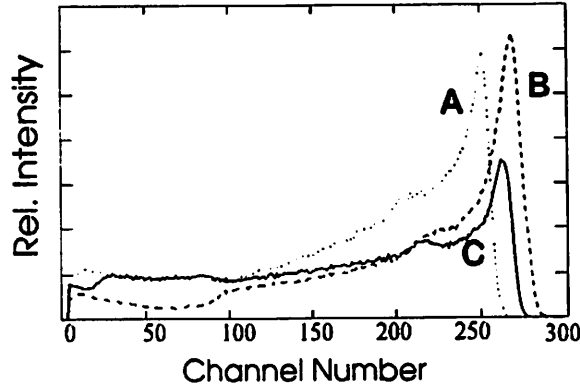


FIGURE 3.2: Simulated spectra from CdTe and CZT detectors. The dotted curve (A) represents a 3 mm $\text{Cd}_{0.9}\text{Zn}_{0.1}\text{Te}_1$ detector with $\mu_h\tau_h = 1.8 \times 10^{-5} \frac{\text{cm}^2}{\text{V}}$ and $\mu_e\tau_e = 2.3 \times 10^{-3} \frac{\text{cm}^2}{\text{V}}$, and the dashed curve (B) shows the response of a 3 mm CdTe detector with $\mu_h\tau_h = 8.0 \times 10^{-5} \frac{\text{cm}^2}{\text{V}}$ and $\mu_e\tau_e = 3.5 \times 10^{-3} \frac{\text{cm}^2}{\text{V}}$. The solid line (C) represents a 6 mm CZT detector.

are representative of those reported by various researchers [43, 50, 44, 51, 52]. In addition, the thickness was varied in the simulations in order to investigate its importance in determining the photopeak efficiency. Figure 3.2 shows the simulated response to 140 keV photons for several cases. The dotted curve (A) represents a 3 mm $\text{Cd}_{0.9}\text{Zn}_{0.1}\text{Te}_1$ detector with $\mu_h\tau_h = 1.8 \times 10^{-5} \frac{\text{cm}^2}{\text{V}}$ and $\mu_e\tau_e = 2.3 \times 10^{-3} \frac{\text{cm}^2}{\text{V}}$, and the dashed curve (B) shows the response of a 3 mm CdTe detector with $\mu_h\tau_h = 8.0 \times 10^{-5} \frac{\text{cm}^2}{\text{V}}$ and $\mu_e\tau_e = 3.5 \times 10^{-3} \frac{\text{cm}^2}{\text{V}}$. The solid line (C) represents a 6 mm CZT detector. In all three cases, the electric field is assumed to be 1300 V/cm parallel to the direction of the incident radiation. The energy resolution was assumed to be 4.5

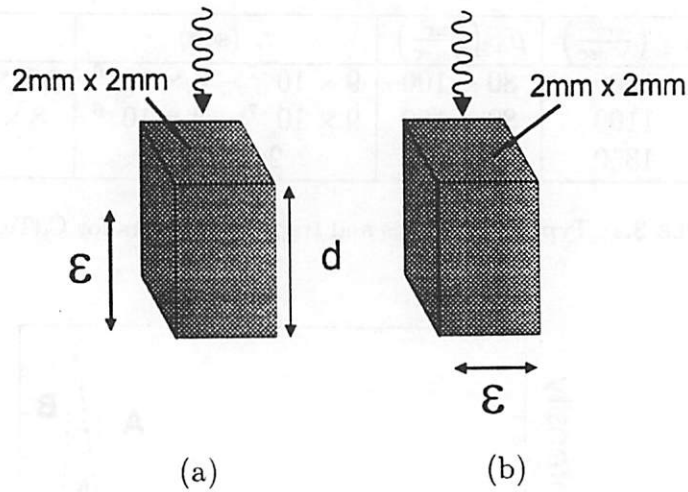


FIGURE 3.3: The simulations included both (a) parallel and (b) perpendicular electric field geometries.

keV for CZT and 6.0 keV for CdTe. Several general characteristics should be noted from the figure. First, the charge trapping results in both a photopeak shift and low energy tails that represent a loss of photopeak efficiency. Next, the tailing becomes worse for thick detectors. Finally, CdTe tends to have a larger $\mu_h\tau_h$ product and higher leakage currents than CZT[44]. Thus, the CdTe spectra are characterized by less tailing but greater photopeak broadening.

In addition to a variety of material parameters, the simulations considered two different electric field geometries as shown in figure 3.3. Although the electric field is parallel to the incident radiation direction in conventional detector geometries, a perpendicular electric field is also possible. Conceptually, the perpendicular electric field is preferred for detection of high energy (*e.g.* 662 keV) photons with thick detectors since the charge trapping is independent of the depth of interaction [53]. Thus, although there is still significant signal loss, the variation in the signal loss is less than in the case of a parallel electric field. The resulting spectra therefore

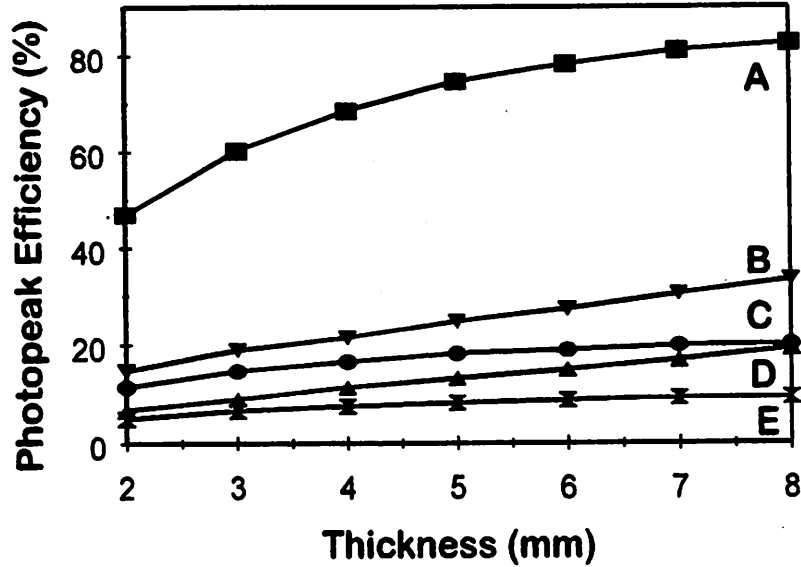


FIGURE 3.4: Variation of photopeak efficiency at 140 keV with thickness. Curve A shows the data for an ideal 2 mm \times 2 mm CdTe detector, and curve B represents a CdTe detector with $\mu_h\tau_h = 8.0 \times 10^{-5} \frac{\text{cm}^2}{\text{V}}$ and $\mu_e\tau_e = 3.5 \times 10^{-3} \frac{\text{cm}^2}{\text{V}}$ in which the electric field is parallel to the direction of the incident radiation. Curve C represents the same detector with a perpendicular electric field. Curves D and E correspond to CZT detectors with $\mu_h\tau_h = 1.8 \times 10^{-5} \frac{\text{cm}^2}{\text{V}}$ and $\mu_e\tau_e = 2.3 \times 10^{-3} \frac{\text{cm}^2}{\text{V}}$ in which the electric fields are parallel to and perpendicular to the incident radiation, respectively.

exhibit narrower tails. Figure 3.4 shows the photopeak efficiency at 140 keV for various detector parameters as a function of thickness. Curve A shows the data for an ideal 2 mm \times 2 mm CdTe detector with no charge trapping; in other words, this curve reflects the geometric contribution to efficiency loss. Note that the curve does not approach 100% detection efficiency as the thickness increases; rather, there is always some loss due to the escape of Compton and K x-ray photons from the side of the detector pixel. Thus, the use of a pixellated geometry will always result in somewhat lower efficiency than an Anger camera geometry. Curve B represents a 2 mm \times 2 mm CdTe detector with $\mu_h\tau_h = 8.0 \times 10^{-5} \frac{\text{cm}^2}{\text{V}}$ and $\mu_e\tau_e = 3.5 \times 10^{-3} \frac{\text{cm}^2}{\text{V}}$ in

which the electric field is parallel to the direction of the incident radiation. Curve C represents the same detector with the electric field perpendicular to the direction of incident radiation. Similarly, curves D and E correspond to CZT detectors with $\mu_h\tau_h = 1.8 \times 10^{-5} \frac{\text{cm}^2}{\text{V}}$ and $\mu_e\tau_e = 2.3 \times 10^{-3} \frac{\text{cm}^2}{\text{V}}$ in which the electric fields are parallel to and perpendicular to the incident radiation, respectively. The energy resolution was assumed to be 4.5 keV for CZT and 6.0 keV for CdTe. In reality, the energy resolution will vary somewhat with detector thickness; however, this variation does not significantly affect the photopeak efficiency results. With the electric field parallel to the incident radiation direction, it is assumed that the entrance face corresponds to the negative side of the detector. By comparing the realistic detector curves to the ideal curve, it can be seen that the benefit of high Z is offset by the charge-trapping effect. This loss of photopeak efficiency is a severe limitation of these detectors.

It is also interesting to note that orienting the electric field perpendicular to the incident radiation degrades the performance of the detector, contrary to results that have been reported for higher energies (*e.g.* 662 keV) [53]. With 140 keV photons incident parallel to the electric field, interactions occur preferentially near the negative electrode. Thus, on average, the holes travel a shorter distance than when the electric field is perpendicular to the incident radiation direction. Therefore, holes are less likely to be trapped, and the photopeak efficiency is better.

Figure 3.5 shows the photopeak efficiency at 140 keV as a function of $\mu_h\tau_h$ for a 4 mm-thick detector under the assumptions that the electric field is 1300 V/cm and that electron trapping is negligible. Significant improvement of $\mu_h\tau_h$ is necessary in order to obtain excellent photopeak efficiency.

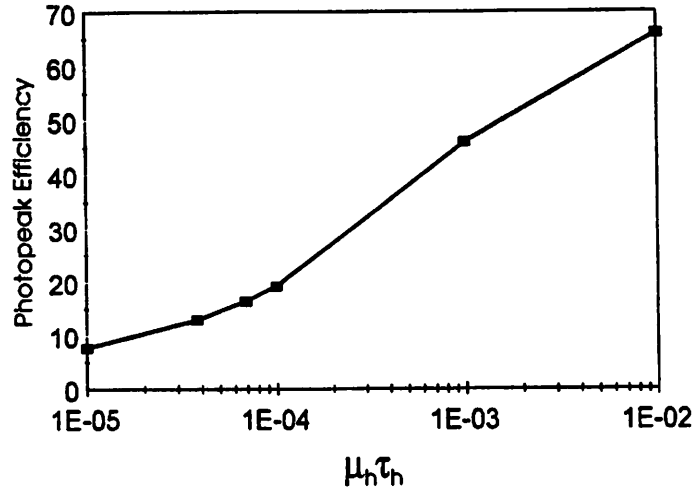


FIGURE 3.5: Photopeak efficiency of a 4 mm-thick detector at 140 keV vs. $\mu_h \tau_h$ assuming that the electric field is 1300 V/cm and that electron trapping is negligible.

3.1.2 Scatter-Rejection Capability

In addition to photopeak efficiency, scatter rejection is an important consideration for radionuclide imaging. In the absence of charge trapping, the ratio of scattered photons to primary photons in SPECT data is approximately a linear function of the FWHM energy resolution [54]. In order to determine if this relationship holds in the presence of trapping, the Monte Carlo simulation described previously was used to predict the response of a $2 \times 2 \times 5 \text{ mm}^3$ detector when irradiated by a point source of 140 keV photons imbedded within a 12 cm radius sphere of water for various values of $\mu_h \tau_h$. This geometry produces an incident spectrum representative of typical SPECT data. The scatter-to-primary ratio was determined for counts that appeared in an energy window centered on the photopeak. The results showed that trapping introduces only a negligible effect; the scatter fraction is primarily a function of energy resolution. This result is consistent with the observation that charge trapping losses increase slowly as the photon energy is increased.

An energy resolution of 3.2 keV FWHM with CdZnTe at room temperature has been reported for thin (≈ 1 mm) detectors [55]; thicker detectors exhibit resolutions approaching 5 keV. Moderately thick CdTe detectors can achieve an energy resolution of 6 keV at room temperature, and 2.5 keV with cooling to 5 °C [52]. Thus, these detectors cannot achieve the scatter-rejection performance of high-purity germanium detectors. However, their resolution is still significantly better than that of sodium iodide; so, a CdTe-based SPECT system should exhibit attractive scatter rejection potential. Chapters 5 and 6 contain further discussion of this point.

3.2 Count-Rate Limitations

For simultaneous collection of radionuclide and x-ray data, fast pulse counting is desired. The count-rate capabilities of a detector are ultimately limited by the charge collection process. For a detector without detrapping, the hole collection time is given by

$$T_C = \frac{z}{\mu_h \xi}, \quad (3.2)$$

where z is the distance from the photon interaction point to the cathode; a similar expression applies to electrons [37]. In other words, the charge carriers travel with a linear velocity across the detector. (Note that charge trapping changes the detector output pulse amplitudes, but not their duration.) Typical mobilities are $\mu_h = 95 \frac{\text{cm}^2}{\text{V}\cdot\text{sec}}$ and $\mu_e = 1100 \frac{\text{cm}^2}{\text{V}\cdot\text{sec}}$ for holes and electrons, respectively.

Assuming no detrapping, the Monte Carlo Code was used to calculate the mean charge collection time as a function of thickness for 100 keV (a typical diagnostic x-ray energy) photons incident on the negative side of a 2 mm \times 2 mm CdTe detector. In the simulation, the electron and hole collection times are calculated

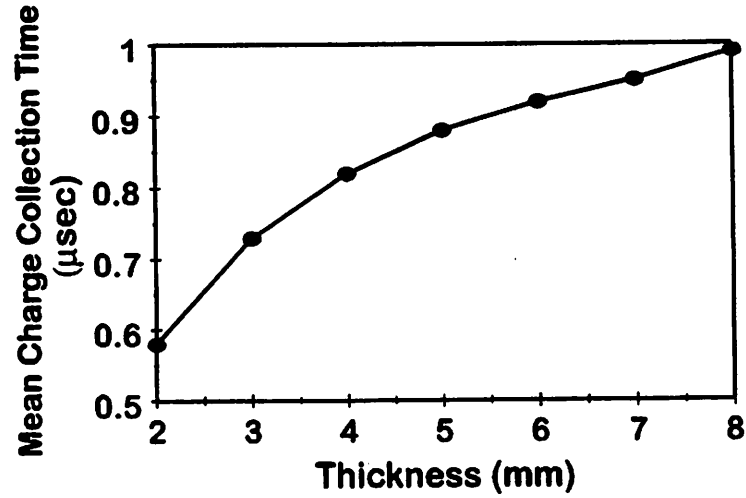


FIGURE 3.6: Variation of the mean charge collection time with thickness for a 2 mm \times 2 mm CdTe detector ($\mu_h \tau_h = 8.0 \times 10^{-5} \frac{\text{cm}^2}{\text{V}}$ and $\mu_e \tau_e = 3.5 \times 10^{-3} \frac{\text{cm}^2}{\text{V}}$) with the electric field parallel to the incident radiation.

from the interaction depth for each photon event; the longer of these two times is designated as the charge-collection time for the event. Averaging over a large number of photon histories yields the mean collection time. Figure 3.6 shows the results. Simulation of detectors with the electric field perpendicular to the incident radiation yielded a mean charge collection time of 1.6 μsec for a 2 mm \times 2 mm detector independent of thickness. Thus, at diagnostic energies the parallel electric field provides superior performance both in terms of photopeak efficiency and count rate capabilities.

Charge detrapping can further limit the collection time. When slow detrapping occurs, it can be shown [56] that the mean time T'_C required for a hole to traverse the detector is given by

$$T'_C = \left(\frac{\tau_h + \tau_D}{\tau_h} \right) T_C, \quad (3.3)$$

where T_C is the charge collection time from above; τ_h is the mean free drift time before trapping that was introduced earlier, and τ_D is the mean detrapping time. Detrapping times ranging from microseconds to days have been reported in the literature, although most measurements fall in the 10-100 μsec range. In general, the detrapping time for a batch of detectors should be measured before they are included in a system.

3.2.1 Current Mode Operation

Fast collection of x-ray CT data demands current-mode readout in which the detector current is converted to a voltage by a transimpedance amplifier. Under these circumstances, the noise floor is determined by the shot noise in the leakage current in the detector and by the input noise current of the transimpedance amplifier. In modern clinical CT systems, which employ cadmium tungstate (CdWO_4) scintillators and photodiodes for data acquisition, the noise is dominated by amplifier noise [22]. In these systems, the 1 pA input noise current of optimized amplifiers is equivalent to approximately 4 (70 keV) x-ray photons/msec. Setting this electronic noise equal to the quantum (Poisson) noise in the x-ray signal yields a noise floor of 16 photons/msec.

Cd(Zn)Te detectors exhibit leakage currents of 10-50 nA; generally, CZT detectors will have lower leakage than CdTe detectors. The shot noise current is given by

$$\langle I^2 \rangle = 2qI_L B, \quad (3.4)$$

where q is the electron charge, I_L is the leakage current, and B is the bandwidth. A 50 nA leakage current and a 500 Hz bandwidth yield an input noise current of approximately 2.8 pA. Adding (in quadrature) 5 pA input noise from our ampli-

fier gives a total noise current of 6 pA, which corresponds to 2.4 photons/msec in Cd(Zn)Te. The noise floor is therefore approximately 6 photons/msec. Thus, Cd(Zn)Te theoretically offers good performance for x-ray CT.

Unfortunately, the leakage current in both CdTe and CdZnTe is highly temperature dependent; variations in excess of 10 %/°C have been reported [57]. For proper calibration and zeroing of x-ray CT measurements, the fluctuation in the leakage current must be negligible compared to the x-ray CT signal in order to achieve the desired 10^6 dynamic range. Thus, some means of temperature control must be employed in order to allow current-mode x-ray CT with Cd(Zn)Te.

Another limitation of Cd(Zn)Te detectors for current mode operation is the de-trapping effect discussed earlier. The slow release of trapped charge can lead to "afterglow" in the x-ray signal. For some Cd(Zn)Te material, this delayed response can be worse than for CdWO₄ scintillators, in which signals typically decay within 10-20 μ sec. At least one group has used proprietary techniques to produce photovoltaic p-i-n CdTe detectors with very little afterglow for x-ray CT [58]; however, it is unlikely that their results can be transferred to the metal-semiconductor-metal devices of interest for the ETCT system.

3.3 Correction for Charge-Trapping Losses

The photopeak efficiency results shown earlier reveal that the benefit gained by the high atomic number of Cd(Zn)Te is offset by the charge trapping effect. In order to regain the intrinsic efficiency of the material, some correction scheme is necessary. Although several hardware-based correction techniques have been developed [59], many rely on rejection of pulses that are due mainly to hole transport; they do not

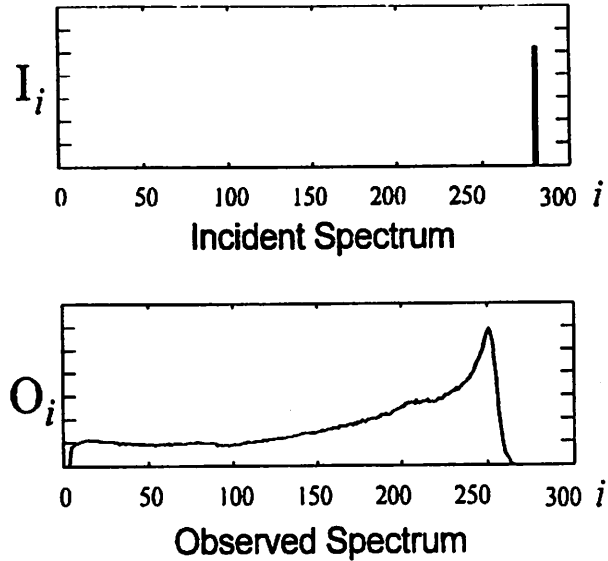


FIGURE 3.7: The linear systems representation of the incident (I) and observed (O) spectra in a Cd(Zn)Te detector for an ideal monoenergetic source.

recover any photopeak efficiency. Therefore, it is useful to investigate both software schemes and hardware techniques that do not reject counts.

3.3.1 A Singular-Value Decomposition Method

One possible correction scheme can be developed as follows. Suppose that the incident photon spectrum can be separated into discrete energy bins and represented by a column matrix I . The detected spectrum can be represented similarly by O . Figure 3.7 shows I and O for the case of a monoenergetic radioactive source. The relationship between the incident and detected spectra is given by

$$O = HI, \quad (3.5)$$

where H is a square matrix representing the detector response, which can be easily calculated from the Monte Carlo model described above. The model yields simulated

spectra corresponding to a monoenergetic source. If the simulation is repeated over a range of incident photon energies, each simulated spectrum represents a column of \mathbf{H} . Alternatively, one can measure the detector response function for a large number of photon energies in order to generate an empirical library. In this case, since a continuously tunable monoenergetic photon source does not exist, interpolation between available energies is necessary in order to generate the complete matrix \mathbf{H} .

In theory, the incident spectrum \mathbf{I} can be recovered from a measured spectrum \mathbf{O} by inverting the matrix \mathbf{H} . However, \mathbf{H} is usually ill-conditioned or singular, and therefore not invertible. The null space of \mathbf{H} is generally spanned by vectors with strong components in the high energy region where charge trapping is more severe. Fortunately, approximate solutions to this inverse problem can be developed. Eskin *et. al.* [60] have described a scheme based upon an expectation-maximization algorithm. Although this technique works quite well, it requires many iterations and is therefore somewhat impractical.

A more computationally efficient approach is possible. The first step is to carry out a singular value decomposition (SVD) [61] of \mathbf{H} in order to determine the "pseudo-inverse" $\tilde{\mathbf{H}}^{-1}$. The component of $\tilde{\mathbf{H}}^{-1}$ corresponding to small singular values is set to zero. An estimate of the incident spectrum is then calculated according to

$$\mathbf{I} = \tilde{\mathbf{H}}^{-1}\mathbf{O}. \quad (3.6)$$

In the final step, negative values of \mathbf{O}_i are set to zero. The SVD method has the advantage that the decomposition needs to be carried out only once for a given response matrix \mathbf{H} . The processing of individual spectra amounts only to relatively simple matrix multiplications.

Figure 3.8 demonstrates the performance of the algorithm with noisy experi-

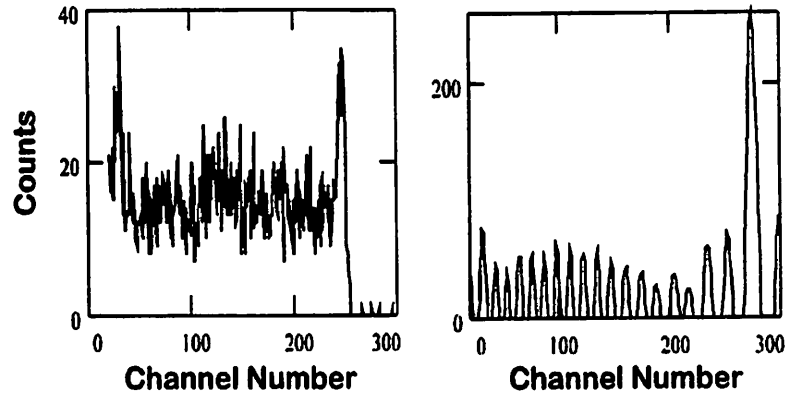


FIGURE 3.8: (a) An experimental spectrum from a ^{99m}Tc point source taken with a CdZnTe detector. (b) A corrected spectrum produced by SVD processing.

mental data. First, a $5 \times 5 \times 5 \text{ mm}^3$ CdZnTe detector (eV Products, Saxonburg, PA) was used to collect a spectrum with approximately 3500 counts from a ^{99m}Tc point source in air. This spectrum was then processed using the SVD method to give the result shown in the figure. In order to determine the transfer matrix \mathbf{H} , an initial spectrum with a large number of counts was collected. This spectrum was then compared with simulated spectra in order to estimate the appropriate $\mu\tau$ products. The model parameters used were $\mu_h\tau_h = 1.6 \times 10^{-5} \frac{\text{cm}^2}{\text{V}}$, $\mu_e\tau_e = 3 \times 10^{-3} \frac{\text{cm}^2}{\text{V}}$, and $\xi=1200 \text{ V/cm}$. While the measured spectrum contains approximately 320 photons in the photopeak, the photopeak in the recovered spectrum includes roughly 2500 counts. Thus, the algorithm recovers the photopeak rather well. Unfortunately, there is additional noise introduced into the processed spectrum. Smoothing the measured spectrum before processing will reduce the excess noise. Alternatively, a gradually decreasing weighting factor, rather than a sharp cut-off, can be applied to the components of $\tilde{\mathbf{H}}^{-1}$ corresponding to small singular values. In short, some optimization of the technique is necessary.

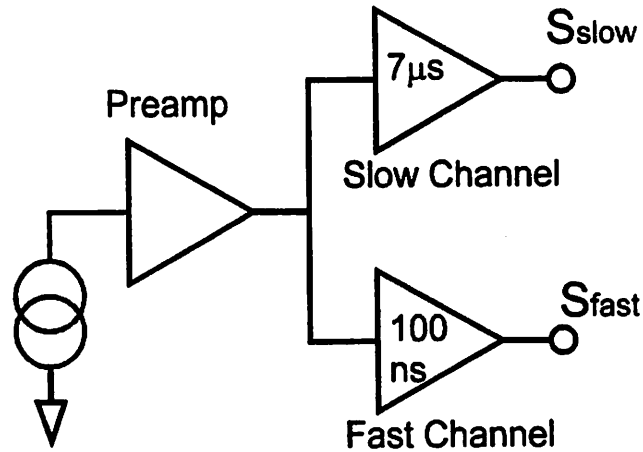


FIGURE 3.9: An implementation of a charge correction scheme using two semi-Gaussian pulse-shapers.

3.3.2 A Hardware-Based Scheme

Finger *et al.* [62] have proposed a hardware-based method to correct for charge-trapping which can be summarized as follows. The preamplifier signal is passed through both a fast and a slow processing channel. While the fast-channel signal corresponds primarily to the electron signal, both electrons and holes contribute to the slow-channel signal. Since the degree of hole trapping varies with the photon-interaction depth, the ratio of the two signals also varies with depth. Thus, once the fast and slow channel signal amplitudes are determined, their ratio can be used to estimate the depth of interaction within the detector. This estimate can be derived either empirically from a histogram of the data or from an adequate model of the detector. From the estimated depth of interaction, one can derive a correction factor for the slow pulse amplitude.

Finger *et al.* implemented their technique with a gated-integrator circuit. A simpler implementation involves using the circuit shown in figure 3.9, which represents a modification of the triple-mode chip discussed in chapter 2. The performance of

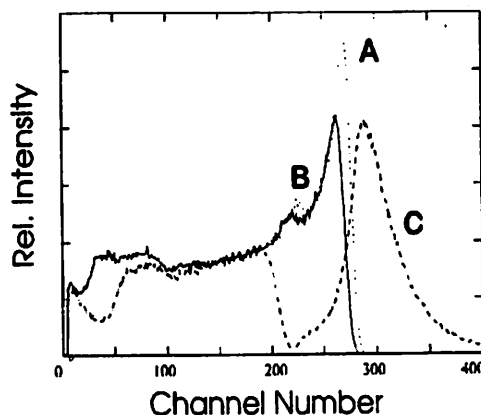


FIGURE 3.10: The slow channel (A) and fast channel (B) spectra were used to estimate the corrected spectrum (C).

this correction technique was simulated for a photon energy of 140 keV. Figure 3.10 shows the simulation results. Curve A represents the spectrum from a $2 \times 2 \times 2$ mm³ CdZnTe detector read out with a 7 μ sec semi-Gaussian pulse shaper; curve B represents the spectrum when a 100 nsec pulse shaping time is used. Note that the “fast” spectrum is degraded by both charge trapping and ballistic deficit. Appropriate levels of noise were added to both the fast and the slow signals, and their ratio was determined. A small random error was added to the ratio to account for timing jitter. The ratio was then used to estimate the depth of interaction based upon a model of the detector and the electronics. From this ratio, a correction factor was determined and was used to correct the slow signal amplitude.

The corrected spectrum is shown as curve C in figure 3.10. Although the low energy tailing is improved, there is significant photopeak broadening, which occurs because noise in the fast and slow pulse signals leads to uncertainty in their ratio and, in turn, to uncertainty in the correction factor. In this respect, the results at 140 keV are not as good as the results achieved by Finger *et al.* at 662 keV, where the signal-to-noise ratios are higher. Note that the correction factor was applied only

to events in channels above 200 because the signal-to-noise ratio is lowest for small-amplitude pulses. There is a trade-off between the choice of this channel threshold and the degree of photopeak broadening. Thus, further experimental work is needed in order to optimize this technique at diagnostic energies.

3.4 Measurements with CdTe Test Devices

In conjunction with UCSF, various test devices were fabricated and tested by Radiation Monitoring Devices, Inc. of Watertown, MA [63]. Devices measuring $2 \times 2 \times 2$ mm³ were operated with an electric field of approximately 2000 V/cm. At room temperature and with negligible pulse pile-up, the detectors achieved an energy resolution of 5.5 keV FWHM at 122 keV. At a count rate of 3×10^5 cps, the resolution was degraded to 7.5 keV due to pile-up effects related to slow charge collection. When cooled to -25 °C with a Peltier cooler, the detector exhibited an energy resolution of 3.1 keV at a count rate of 7×10^4 cps. Although the count-rate capability and energy resolution of the detectors were promising, the utility of the devices was limited by poor photopeak efficiency due both to the small size and to charge trapping.

3.5 Discussion

The critical detector design parameters for the ETCT system include energy resolution, count-rate capability, and photopeak efficiency. In terms of the first two parameters, germanium is an excellent detector material. As stated earlier, the prototype system's HPGe detector can achieve better than 2 keV FWHM energy resolution at low count rates; in addition, the detector allows measured count rates

in excess of 10^6 cps/channel with a sacrifice in energy resolution. Unfortunately, the relatively low atomic number of germanium limits the detection efficiency. The photopeak efficiency of the 6 mm-thick detector currently in use is approximately 39% at 140 keV.

The simulations described in this chapter provide estimates of the corresponding parameters for Cd(Zn)Te detectors with a lateral dimension of 2 mm and thicknesses on the order of 6 mm or less. First, energy resolutions of approximately 4.5 keV and 6 keV can be expected at room temperature for CZT and CdTe, respectively. Moderate cooling can improve the energy resolution to better than 3 keV in both materials. Although somewhat limited in comparison to HPGe, these resolutions are far better than that achieved in an Anger camera. Thus, the energy resolution performance of Cd(Zn)Te is probably acceptable for the ETCT system.

On the other hand, the count-rate performance is rather poor. One can expect a maximum count rate on the order of 10^5 cps, which is likely insufficient for fast x-ray pulse counting. Fortunately, it may be possible to sacrifice the fast mode operation of the ETCT system if current mode operation is available. In this case, the x-ray CT scan could be performed sequentially with the SPECT scan. The main question concerning current mode operation of Cd(Zn)Te is the afterglow arising from detrapping. Since the duration of an ETCT study is dictated mainly by the long SPECT scan, the x-ray CT scan can be performed slowly enough to tolerate moderate afterglow in the detectors.

The most serious weakness of Cd(Zn)Te is the loss of photopeak efficiency due to charge trapping. Typical geometries and material parameters yield photopeak efficiencies in the 20-30% range at 140 keV. Quite simply, this efficiency is unacceptable for the ETCT system. Thus, some means of trapping correction is necessary. The

singular value decomposition method and the dual time constant sampling technique are two possibilities that merit further experimental testing. Of course, the ideal correction method would involve improvements of the devices themselves. The next chapter focuses on possible modifications to the device geometry. Alternatively, research aimed at reducing both contact imperfections and bulk defects may lead to improved transport properties. If the photopeak efficiency can be improved, Cd(Zn)Te will likely be an acceptable ETCT detector material offering the practical advantages of room-temperature operation, large size, and potentially low cost.

Chapter 4

The Role of Device Geometry in Charge Trapping

The ideal method to overcome charge trapping is to eliminate its effect through improvement of the material or by modification of the device geometry. Although the materials research is progressing somewhat slowly, Barrett *et. al.* [49] have recently demonstrated that a detector with a pixellated geometry will exhibit little hole tailing if the pixel size is small compared to the thickness of the detector and if the pixellated side is the anode side of the detector. Other groups have shown that the same phenomenon occurs in strip detectors with thin anode strips [64, 65]. This “small-anode” effect is closely related to the coplanar-grid technique, in which the difference in signal between two thin adjacent strips is used to determine the charge signal [66]. The behavior can be understood as follows. Signal induction in a semiconductor detector occurs only when there is strong electrostatic coupling between a moving charge carrier and the sensing electrode. For a small pixel geometry, the coupling is strong only when the charge carrier is close to the pixel. Thus, the signal induction arises primarily due to electron motion in the vicinity of the anode. In effect, the sensing electrode does not “see” the hole motion. Therefore, the hole trapping has little effect on the observed spectra.

An accurate detector model is needed to study the influence of device geometry on charge-trapping. Earlier modeling work has focused on the case of detectors in which the pixel size is on the order of several hundred microns and in which the pixel spacing is negligible [67]. The purpose of the present work was to simulate the behavior of larger strip detectors with strip widths on the order of a millimeter and thicknesses approaching a centimeter since such geometries are appropriate for the single-slice implementation of the ETCT system. In larger detectors, electron trapping is significant because electrons can become trapped before they enter the signal induction region surrounding the anode. In addition, the effect of significant inter-pixel space is of interest; in particular, it is possible that narrowing of the anode strip without changing the detector pitch will improve the performance of the detector.

The simulation methods presented in this chapter extend previously reported simulation studies [64, 65, 67] in several ways. First, a convenient method of potential calculation is adopted from the microwave literature [68, 69]. Next, an efficient method for treating charge-carrier transport within the detector subject to both trapping and detrapping is proposed. Finally, the simulation can be easily modified to treat non-uniform electric fields, multiple trapping sites, and spatially varying trapping behavior.

4.1 Detector Model

Accurate modeling of detector response requires an understanding of the mechanism responsible for signal induction by a moving charge carrier within a detector [70, 71]. Since the carrier velocity is low compared to the velocity of light, the

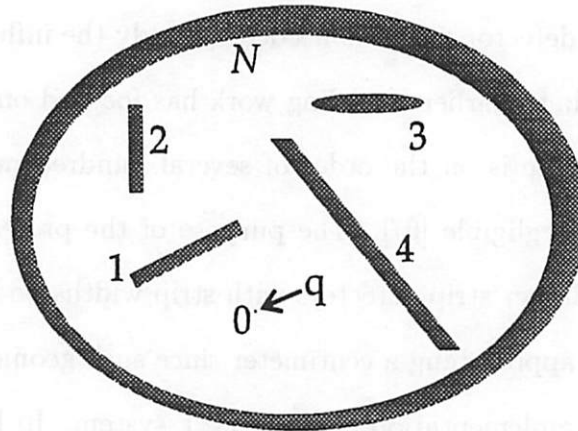


FIGURE 4.1: An arbitrary electrode geometry.

problem can be treated by electrostatic considerations. In order to determine the induced signal charge, first consider a charge within an interelectrode space, and assume that the charge resides on an infinitesimal electrode. Let the infinitesimal electrode be denoted by index 0, the sensing electrode by 1, and the others by 2... N as shown in figure 4.1. In the general case, the charges and the potentials on the electrodes are related by the matrix equation

$$\mathbf{Q} = \mathbf{C}\Phi, \quad (4.1)$$

where \mathbf{Q} is a vector containing the charge on each electrode; Φ is a vector of potentials, and \mathbf{C} is the capacitance matrix.

Now consider two situations. In the first situation, conductor 0 possesses charge q_0 , and all other conductors are grounded. The induced charge on conductor 1 is given by Q_1 , and the potential on the infinitesimal conductor is denoted by ϕ_0 . In this case, equation 4.1 gives two relevant equations:

$$q_0 = C_{00}\phi_0 \quad (4.2)$$

$$Q_1 = C_{01}\phi_0, \quad (4.3)$$

where Green's reciprocity theorem is used implicitly to write $C_{01} = C_{10}$ in the second of these equations. In the second situation, conductor 0 is uncharged; conductor 1 is at potential V_s , and all other conductors are grounded. Denote the potential induced on conductor 0 by $V_0(\vec{r})$. In this case, equation 4.1 yields

$$0 = C_{00}V_0(\vec{r}) + C_{01}V_s, \quad (4.4)$$

where C_{00} is the self-capacitance of electrode 0, and C_{01} is the partial capacitance between electrode 0 and electrode 1.

Elimination of ϕ_0 from equations 4.2 and 4.3 and use of equation 4.4 yields an expression for the charge induced on the sensing electrode

$$Q_1 = \frac{C_{01}}{C_{00}}q_0 = -\frac{V_0(\vec{r})}{V_s}q_0. \quad (4.5)$$

Usually given the symbol $\Phi_w(\vec{r})$, the quantity $\frac{V_0(\vec{r})}{V_s}$ is called the weighting potential. It is a normalized measure of the partial capacitance of the infinitesimal electrode and the sensing electrode; hence, it determines the electrostatic coupling of the charge carrier to the sensing electrode. It must be emphasized that the weighting potential is a mathematical construct rather than a real physical potential: it is generally quite different than the operating potential within the detector. Generated by the applied bias, the operating potential determines the motion of the charge carriers. The total signal charge induced by a charge carrier of charge q_0 moving from position \vec{r}_1 to position \vec{r}_2 is given in terms of the weighting potential by

$$\Delta Q_{sig} = q_0 [\Phi_w(\vec{r}_1) - \Phi_w(\vec{r}_2)]. \quad (4.6)$$

Equation 4.6 provides a means of calculating the induced charge on a sensing electrode as a function of carrier position within the detector.

The computation of induced signal charge represents only a small part of the calculation of detector response. The simulation of measured spectra requires several

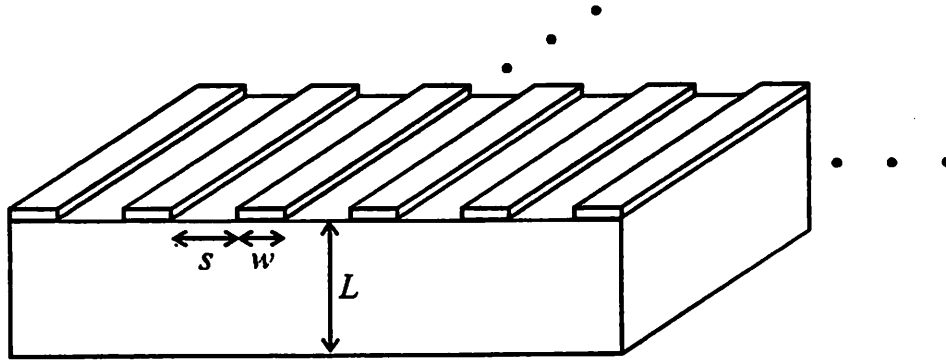


FIGURE 4.2: The strip detector geometry.

steps. First, both the weighting potential and the operating potential must be calculated using methods of electrostatics. Next, the radiation transport within the detector must be simulated to determine where charge carriers are produced. Finally, the equations of motion governing charge transport must be solved in order to estimate the measured signals. Each of these parts of the simulation will be discussed in the following subsections.

4.1.1 Potential Calculations

Figure 4.2 shows the strip detector geometry. The detector thickness is denoted by L ; the anode strip width is given by w , and s is the strip spacing. The length of the detector conveniently can be considered infinite. Thus, the calculation of the operating and weighting potentials reduces to solving the two dimensional Laplace equation,

$$\frac{\partial^2 \Phi(x, y)}{\partial x^2} + \frac{\partial^2 \Phi(x, y)}{\partial y^2} = 0, \quad (4.7)$$

subject to appropriate boundary conditions. The geometries and boundary conditions for determining the operating and weighting potentials are shown in figures 4.3a.

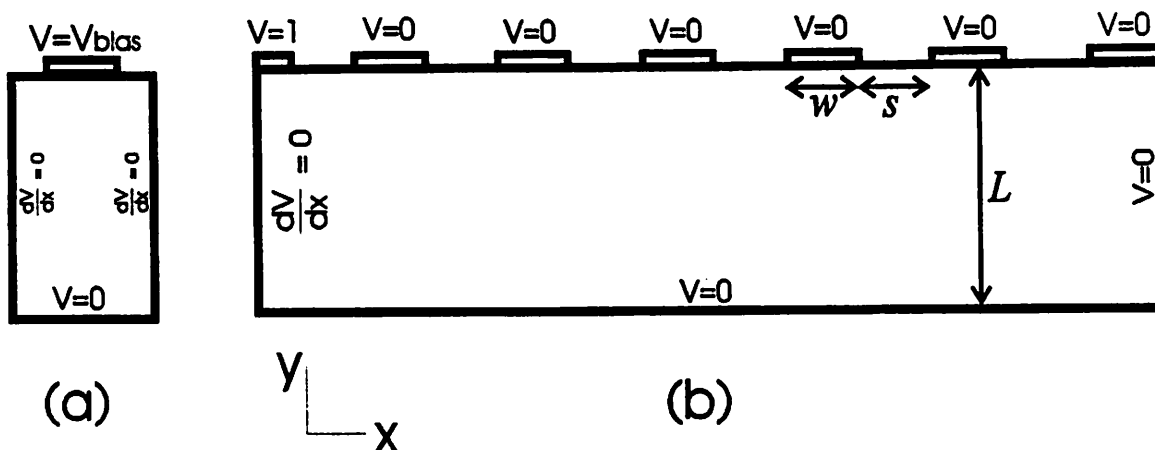


FIGURE 4.3: The strip detector boundary conditions used for calculating (a) the operating potential and (b) the weighting potential.

and 4.3b. The operating potential is determined by applying the high voltage bias to all anode strips. Thus, the geometry is periodic, and only one strip needs to be considered. The boundary condition $\frac{\partial V}{\partial x} = 0$ expresses this symmetry. On the other hand, the weighting potential is calculated by applying unit potential to the sensing electrode of interest while all other electrodes are grounded. Thus, there is no periodicity. The geometry for the calculation must include enough strips that the weighting potential can be assumed to be zero at the right edge.

The fact that the potential in the dielectric regions between strips is unknown *a priori* leads to mixed boundary conditions. As a result, an analytic solution is impossible. However, an efficient numerical technique can be used to estimate the potential distribution within the detector. The following strategy is used to compute both the weighting potential and the operating potential. The first step is to determine an expression for the potential in the detector volume as a function of the potential at the electrode boundary. Next, the potential at the boundary can be related to the charge distribution at the boundary. Finally, the charge distribution

can be estimated as an expansion of known basis functions; it will be shown that this calculation is easily performed in the Fourier domain. Thus, knowledge of the electrode charge yields the potential throughout the detector volume. Reference [69] contains a detailed discussion of this method.

By Fourier transforming the Laplace equation with respect to the x variable and applying the appropriate boundary conditions, it can be shown that for both geometries the solution takes the form

$$\tilde{\Phi}(k_x, y) = \tilde{\Phi}_o k_x \frac{\sinh(k_x y)}{\sinh(k_x L)}, \quad (4.8)$$

where k_x is the transform-domain analog of x , and $\tilde{\phi}_o$ is the Fourier transform of the potential at the $y = L$ boundary. It can also be shown that the potential at the boundary is related to the charge at the boundary by

$$\tilde{\Phi}_o(k_x) = \frac{1}{\epsilon_o k_x [1 + \epsilon_r \coth(k_x L)]} \tilde{\rho}(k_x) = \tilde{G}(k_x) \tilde{\rho}(k_x), \quad (4.9)$$

where ϵ_o is the permittivity of free space, ϵ_r is the relative dielectric constant of the semiconductor material, and $\tilde{\rho}(k_x)$ is the Fourier transform of the charge distribution [72]. The function multiplying $\tilde{\rho}(k_x)$ is the spectral domain Green's function for the problem; it can be represented by $\tilde{G}(k_x)$.

Starting from equation 4.9, the potential at the boundary can be estimated using the spectral domain Galerkin method, a technique which is well known in the microwave literature [68, 69]. In this approach, $\tilde{\rho}$ is expanded in terms of known basis functions as

$$\tilde{\rho}(k_x) = \sum_{m=1}^M a_m \tilde{\rho}_m(k_x) \quad (4.10)$$

where the a_m are unknown coefficients, and M is the number of functions in the basis set. The functions $\tilde{\rho}_m$ are chosen such that their inverse transforms ρ_m are nonzero only over the strips.

Next, equation 4.10 is substituted into equation 4.9, and the inner product of each side with $\tilde{\rho}_j$ is calculated. When using a finite Fourier transform in which the variable k_x is discrete and indexed by n , this manipulation leads to a set of linear equations of the form

$$\sum_{n=0}^{n=\infty} \tilde{\phi}_0(k_{x,n}) \tilde{\rho}_j(k_{x,n}) = \sum_{n=0}^{n=\infty} \tilde{G}(k_{x,n}) \sum_{m=1}^{m=M} a_m \tilde{\rho}_m(k_{x,n}) \tilde{\rho}_j(k_{x,n}). \quad (4.11)$$

Application of Parseval's theorem to the left hand side leads to

$$\frac{P}{2} \int_0^P \phi_o(x) \rho_j(x) = \sum_{n=0}^{n=\infty} \tilde{G}(k_{x,n}) \sum_{m=1}^{m=M} a_m \tilde{\rho}_m(k_{x,n}) \tilde{\rho}_j(k_{x,n}). \quad (4.12)$$

Since $\rho_j(x)$ is zero outside the strips and $\phi_o(x)$ is known on the strips, evaluation of the left-hand side of equation 4.12 is straightforward. The resulting equations defining a_m are then easily solved if there are a limited number of basis functions.

For calculation of the operating potential, the basis functions are defined by

$$\begin{aligned} \rho_1(x) &= \frac{1}{w} \\ \rho_2(x) &= 1 - \frac{2}{w} \left| x - \frac{s}{2} - \frac{w}{2} \right| \\ \rho_3(x) &= \frac{w^4}{32} \left| \left(x - \frac{s}{2} - \frac{w}{2} \right)^3 \right| \\ \rho_4(x) &= \frac{1}{\pi \sqrt{\left| x - \frac{s}{2} - \frac{w}{2} \right| - \frac{w}{2}}}. \end{aligned} \quad (4.13)$$

on the strip and by $\rho_i(x) = 0$ off of the strip. This set of basis function reflects the fact that there is a strong charge concentration near the edges of the strips. The choice of physically realistic basis functions (rather than sines and cosines, for example) yields a reasonably accurate answer with only a few basis functions[69]. Alternatively, the Chebyshev polynomials are a possible choice for a complete set. The basis set for calculation of the weighting potential is similar to the set defined by equation 4.13. However, there are four basis functions for each strip, and the

functions are asymmetric since the charge concentration is peaked towards one side of the strips.

Once the a_m are determined from equation 4.12, $\tilde{\rho}(k_x)$ is known from equation 4.10. Next, equation 4.9 determines $\tilde{\phi}_o(k_x)$. Finally, application of equation 4.8 and inverse transformation yield the potential distributions throughout the detector volume.

4.1.2 Radiation Transport

The EGS4 Monte Carlo code [45] was used to simulate the radiation transport within the detector. The code accounts for geometric effects within the detector such as transmission losses, Compton photon escape, and K x-ray escape. The code was modified in order to account for charge trapping effects. Rather than scoring the deposited energy each time an interaction occurs, the energy is first converted to a deposited charge. The charge transport part of the simulation is then used to determine the signal induced at the sensing electrode due to this deposited charge. The total measured signal is then scored for each event. Thus, the charge transport behavior of the detector is fully integrated into the Monte Carlo simulation. Note that the spreading of charge within the detector is neglected since this effect becomes significant only for strip widths below approximately $300 \mu\text{m}$ [67].

4.1.3 Charge Transport

Several techniques are available to calculate the induced signal due to charge transport. For one-dimensional transport in a linear electric field subject to a single trapping state, the solution is known analytically [73]. For more complicated geometries and trapping distributions, numerical techniques are necessary. One pos-

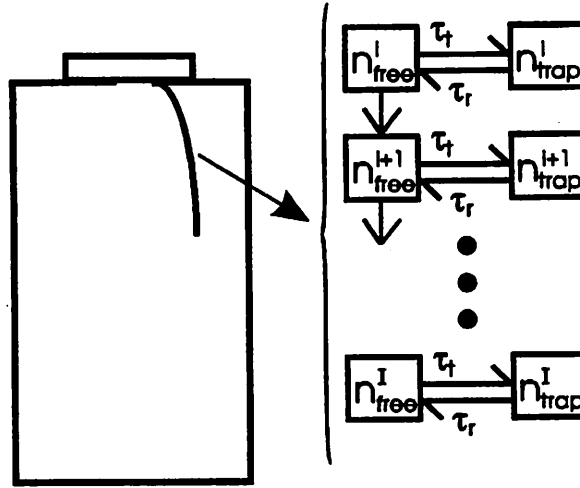


FIGURE 4.4: The charge-carrier path is partitioned into a discrete column geometry in order to simulate the charge transport within the detector.

sible approach is to transport the charge using Monte Carlo techniques. Although this technique yields accurate results, it is computationally intensive. Therefore, a different approach to the charge transport calculations is desirable.

Once the interaction position is known, the paths of the charge carriers are determined by calculating the gradient of the operating potential. The curved path of the electrons and of the holes are then each mapped into a one-dimensional column of discrete cells as shown in figure 4.4. Representing a segment of the path, each cell contains a number of free carriers n_{free}^i and a number of trapped carriers $n_{trapped}^i$, where i denotes the i th cell. The distribution of carriers as a function of time can be determined by updating the contents of each cell after a time step according to the equations

$$\Delta n_{free}^i = -\frac{v_i \Delta t}{L_i} n_{free}^i + \frac{v_{i-1} \Delta t}{L_{i-1}} n_{free}^{i-1} - \frac{\Delta t}{\tau_{trap}} n_{free}^i + \frac{\Delta t}{\tau_{release}} n_{trapped}^i \quad (4.14)$$

$$\Delta n_{trapped}^i = \frac{\Delta t}{\tau_{trap}} n_{free}^i - \frac{\Delta t}{\tau_{release}} n_{trapped}^i, \quad (4.15)$$

where τ_{trap} is the mean free trapping time; $\tau_{release}$ is the mean free release time;

v_i is the velocity of charge carriers in the i th cell; L_i is the length of the i th cell, and Δt is the integration time step. While the first term on the right hand side of equation 4.14 is the number of free carriers leaving the i th cell, the second term represents the number of free carriers entering the i th cell. Likewise, the third term represents the number of carriers that are trapped in the i th cell during a unit time step, and the last term is the number of carriers that are released from traps. The interpretation of equation 4.15 is similar. During the mapping, the length of each cell is determined as a function of the carrier velocity within the cell; it is chosen such that the fraction of carriers leaving a cell in a single time step is constant throughout the column. This choice enhances the numerical stability of the computation.

The simulation is started with all of the charge carriers free in the top cell. Then, the time-step iteration is repeated until the measurement time is reached. The measurement time is assumed to be 6 μsec , which is approximately the maximum pulse-shaping time that would be used with Cd(Zn)Te detectors. At this point in the simulation, the induced signal charge due to the electrons is calculated from equation 4.6 according to

$$Q_{sig}^{e^-} = - \sum_{i=1}^I q_o [n_{free}^i + n_{trapped}^i] [\Phi_w(\vec{r}_i) - \Phi_w(\vec{r}_0)], \quad (4.16)$$

where I is the total number of cells along the electron path; q_o is the charge on an electron; \vec{r}_i is the spatial location of the i th cell, and \vec{r}_0 is interaction position of the radiation. The charge due to hole motion is calculated similarly, and the total signal charge is the sum of the electron and hole charges. If desired, the induced current waveform can be determined by first calculating the total induced signal charge at each time step and then differentiating.

Adoption of this kinetic model of charge transport has several advantages. First, integration of the equations of motion becomes straightforward. Next, the mapping

of the carrier path to a one-dimensional column allows treatment of non-linear electric fields or spatial variations in the electric field. In addition, the model can be easily modified to account for multiple trapping levels by adding terms to equations 4.14. Finally, spatial variations in the trapping behavior can be treated by making the rate constants in equations 4.14 a function of cell position. Thus, the simulation can be modified to determine the effects of spatially localized defects such as grain boundaries.

4.2 Simulation Results

The simulation methods described above were used to investigate the effect of strip width, strip spacing, and detector thickness on the shape of the weighting potential and on the spectral response. As an example, figure 4.5 shows a contour plot of the weighting potential for a detector with strip width $w = 1$ mm, strip spacing $s = 1$ mm, and thickness $L = 8$ mm. The weighting potential is sharply peaked in the vicinity of the strip. Thus, signal induction occurs mainly by the motion of electrons near the anode. The finite strip spacing leads to a number of small "bumps" in the weighting potential on either side of the main lobe.

Although the shape of the weighting potential provides insight into the small anode effect, simulation of spectra is the best way to determine the effect of geometry on detector performance. Therefore, model spectra were generated for a number of different geometries. The number of photon histories was kept constant. Figure 4.6 shows the response of an 8 mm thick detector to 140 keV photons incident uniformly on the front face of the detector for strip widths of 1 mm, 1.5 mm, and 2 mm. The strip spacing was assumed to be negligible when generating these three spectra; in

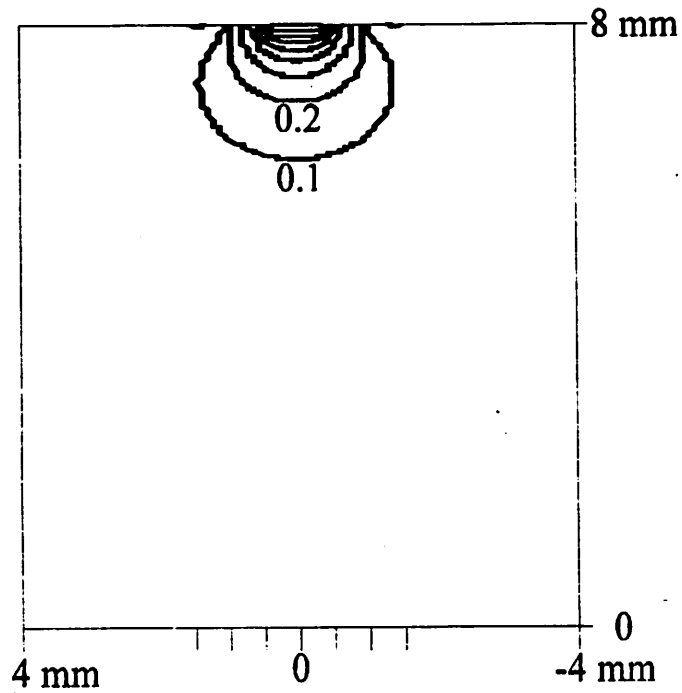


FIGURE 4.5: The calculated weighting potential for a detector with $w = 1$ mm, $s = 1$ mm, and $L = 8$ mm.

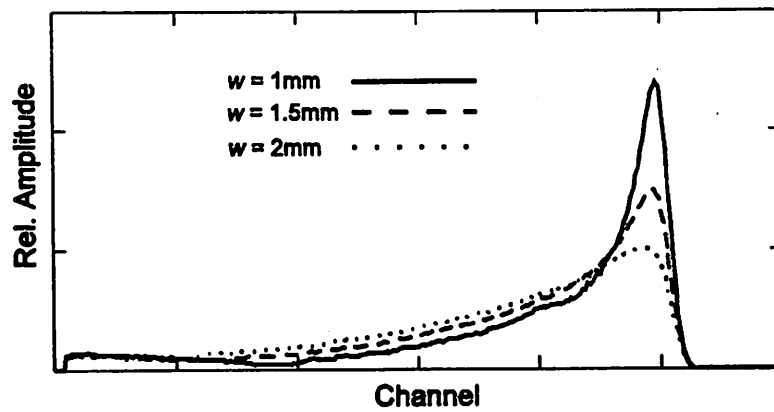


FIGURE 4.6: Simulated spectra from 8 mm-thick detectors with different strip widths and negligible interstrip space.

other words, the weighting potential was assumed to drop immediately to zero at the edge of a strip. The material parameters in the simulation are consistent with those reported in the literature[43, 44]. The carrier mobilities are $\mu_e = 1100\text{cm}^2/\text{v}\cdot\text{sec}$ and $\mu_h = 90\text{cm}^2/\text{v}\cdot\text{sec}$ for electrons and for holes respectively, and the mean trapping lifetimes are $\tau_e = 1\mu\text{sec}$ and $\tau_h = 200\text{ nsec}$. The mean release time for both electrons and holes is assumed to be $20\mu\text{sec}$ (a typical value found in the literature), and the electric field is set to 1500 V/cm . A noise level corresponding to 5 keV FWHM energy resolution is assumed. The results show that the spectra improve significantly as the strip width is decreased from 2 mm to 1 mm . The decreased low-energy tailing leads to an increase in photopeak efficiency.

Although decreased strip width leads to improved performance, it also leads to an increase in the number of channels if the strip spacing is left unchanged. The associated increase in electronics cost may be unacceptable for many applications. In order to minimize this problem, one might consider reducing the strip width while leaving the strip pitch constant (*i.e.*, increasing the strip spacing). To simulate this effect, we generated spectra for detectors with a thickness of 8 mm , a strip pitch of 1.5 mm , and strip widths of 1.5 mm , 1 mm , and 0.75 mm as shown in figure 4.7. As the strip width is reduced, the tailing decreases; however, the efficiency also decreases since there is poor collection from the inter-strip regions. The optimum choice of strip spacing appears to be approximately a third to a half of the strip width for the dimensions considered here.

The thickness of the detector affects the spectral response in two ways. First, there is a straightforward increase in detection efficiency with thickness. In addition, the tailing behavior for a given w/L ratio does not remain constant as the detector thickness increases. Rather, as the thickness increases, electron trapping becomes

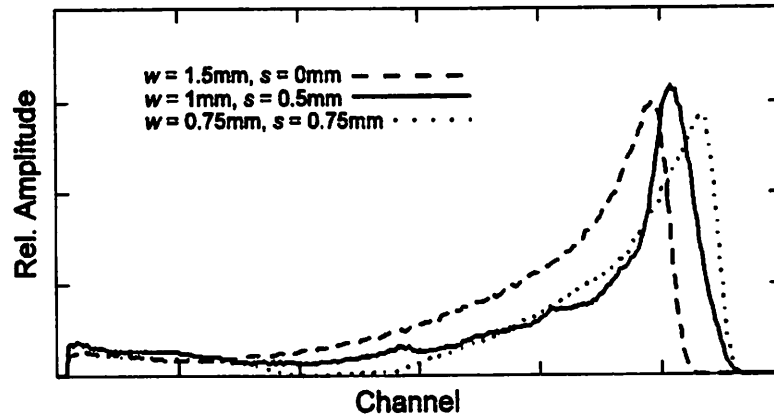


FIGURE 4.7: Simulated spectra from detectors with constant strip pitch and different interstrip spacing.

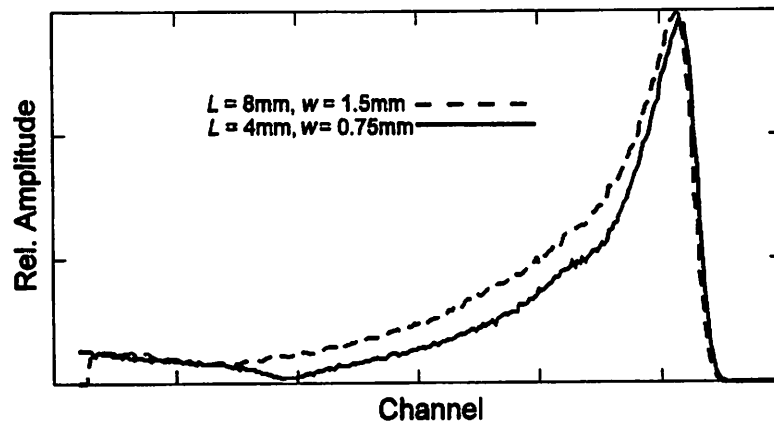


FIGURE 4.8: Simulated spectra from detectors of different thickness.

more significant; more electrons become trapped before entering the signal induction region near the anode. Figure 4.8 shows spectra for a 4 mm-thick detector and for an 8 mm-thick detector with the same w/L ratio. The spectrum from the thick detector displays more tailing and higher overall efficiency than that of the thin detector.

In order to quantify the behavior of the various geometries, the photopeak efficiency was calculated for each case described above. Table 4.1 shows the results. For

L	w	s	Efficiency	
8 mm	1 mm	0 mm	50%	
8 mm	1.5 mm	0 mm	39%	
8 mm	2 mm	0 mm	32%	
8 mm	1 mm	0.5 mm	42%	
8 mm	0.75 mm	0.75 mm	32%	
8 mm	1 mm	0 mm	80%	No Trapping

TABLE 4.1: Calculated photopeak efficiency at 140 keV for various detector parameters

comparison, the table includes the photopeak efficiency of an 8 mm thick detector with $w = 1$ mm and $s = 0$ mm when there is no charge trapping.

Although the goal of this work is to determine detector geometries which maximize the photopeak efficiency, it should be noted that the small-anode effect also provides potential improvement in count-rate performance. In a planar detector, the signal rise time is dictated by the transit time required for the charge carriers to traverse the device. In the small-anode geometry, however, signal induction occurs mainly when the electrons are within close proximity to the anode. Thus, the signal rise time can be quite short. Figure 4.9 (taken from reference [67]) shows the collected charge signal corresponding to three interaction depths for both planar ($\frac{w}{L} = 10$) and small anode ($\frac{w}{L} = 0.1$) geometries. While the signal in a planar detector rises nearly linearly, the signal in a small-anode geometry rises sharply following a delay determined by the interaction depth. The fast rise-time may allow the use of short pulse shaping times in order to reduce pile-up at high count rates. However, the depth-dependent delay most likely precludes the use of these detectors for fast timing measurements.

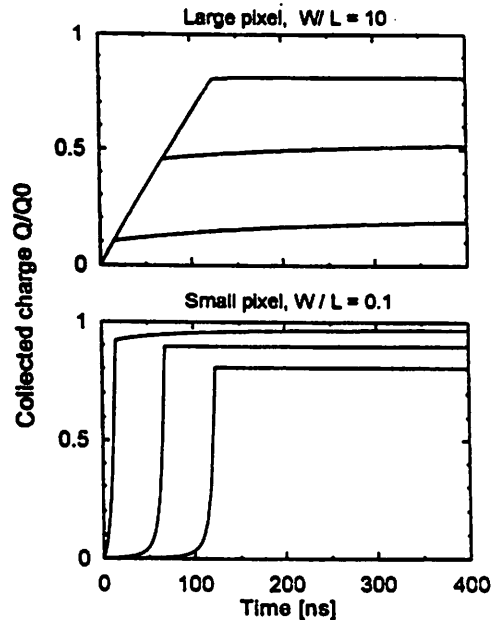


FIGURE 4.9: Simulated charge pulse shapes are shown for interaction depths $0.2L$, $0.5L$, and $0.8L$. While the signal in a planar detector rises nearly linearly, the signal in a small-anode geometry rises sharply following a depth-dependent delay [67].

4.3 Conclusion

The simulations described in this chapter represent a flexible method for predicting the behavior of compound semiconductor strip detectors. The model accounts for both trapping and detrapping, non-linear electric fields, and significant inter-pixel space. In addition, the simulation can be easily modified to treat spatial variations in trapping behavior.

The model is a useful tool for predicting the performance of detectors for the ETCT system. The major limitation of Cd(Zn)Te for many applications, including emission-transmission imaging, is the loss of photopeak efficiency caused by charge trapping. Simulations predict that the use of strip geometries with thin anodes will somewhat alleviate the charge trapping problem. In particular, the results indicate that a detector with $L = 8$ mm, $w = 1$ mm, and $s < 3$ mm will have a photopeak

efficiency in excess of 50% at 140 keV. Although this efficiency is well below the 80% that would be possible without charge trapping, it is better than the 39% photopeak efficiency of the current HPGc detector. The small-anode geometry may also enable the use of fast pulse-counting. Thus, these values will provide a starting point for future fabrication of devices.

Of course, it may prove difficult to produce 8 mm-thick Cd(Zn)Te with adequate uniformity and limited defects. Ultimately, the viability of CdTe and CZT will be determined by the ability of developers to fabricate devices in a reproducible manner with excellent material properties, reliable ohmic contacts, and good dependability at a reasonable cost.

Chapter 5

Simulation Studies of Scatter

Various physical factors limit the quantitative accuracy of radionuclide uptake measurements with SPECT. Among these are photon attenuation, photon noise, finite spatial resolution, and scattered radiation. With the addition of the new triple-mode IC electronics, the ETCT system has the potential to distinguish the effects of different perturbations. The new electronics allow excellent scatter rejection, while the x-ray transmission measurement permits accurate attenuation correction. In addition, the use of iterative collimator response compensation, coupled with region-of-interest definition on the CT images, reduces the error due to finite spatial resolution. The incremental application of these corrections to SPECT data yields knowledge of the relative error introduced by each effect.

Such knowledge is important for two reasons. First, it allows more accurate estimation of uncertainties in general SPECT measurements. Second, it provides a guideline for determination of priorities in the design of future imaging systems. For example, in the investigation of novel detector technologies for the ETCT system, one question naturally arises: how good does the system energy resolution need to

be for quantitative measurements?

Scatter and scatter correction have been discussed extensively in the literature [74, 75]. Researchers have considered the qualitative effect of scatter on SPECT images [76] as well as the quantitative effect of energy resolution on scatter fraction [54, 77]. Much effort has been devoted to the development of software schemes for scatter correction [14, 13]. Yet, the fundamental design question concerning the desired energy resolution has not been answered. Indeed, it is often assumed that the energy resolution should be made as good as possible. In reality, there is a diminishing return as the energy resolution is improved. At some energy resolution, the error due to scatter is small compared to the error due to other physical perturbations and compared to the statistical uncertainty arising from photon noise. In fact, as the energy resolution is improved, the system will begin to reject forward-scattered photons that contribute potentially useful information to the image.¹ It is possible that this reduction in useful counts increases the noise in the image. One goal of this thesis research was to estimate the desirable energy resolution for quantitative SPECT measurements based both on simulations and on experimental measurements with the ETCT system.

The excellent energy resolution of the ETCT electronics allow the rejection of scattered photons from the data set. This “scatter-rejection” approach is much different than the “scatter-correction” methods used with conventional SPECT systems. Correction techniques attempt to overcome the limited energy resolution of the conventional Anger camera (12-13 keV FWHM at 140 keV) by post-processing

¹It is important to distinguish between “energy resolution” and “energy window settings”. Energy resolution refers to the ability of a detection system to differentiate photons of different energies. The window settings refer to the width of region of the recorded spectrum over which photons are included in the data. In practice, the energy window is often chosen to be twice the FWHM energy resolution. This choice ensures that while nearly all of the primary counts are recorded in the data, there is not an excessive number of scatter counts in the data.

the SPECT data. Because scatter rejection approximates the ideal case of scatter-free data, it may produce more accurate SPECT measurements than scatter correction. Scatter-rejected data, however, contains fewer photons than scatter-corrected data. Therefore, the noise properties of scatter-corrected images may be better. Thus, the choice between scatter rejection and scatter correction is not clear, and a preliminary comparison is presented in the present work.

After reviewing the physics that governs photon scatter within the body, this chapter describes a number of simulations that were developed to investigate the role of scatter in radionuclide imaging. Next, the specific results are discussed and extrapolated to general SPECT imaging. Finally, the next chapter contains both experimental results that parallel the simulations and a discussion of scatter rejection and correction.

5.1 The Physics of Photon Scatter

The dominant scattering mechanism in tissue-like materials is the Compton interaction. During a Compton event, a photon with energy $h\nu_0$ interacts with an atomic electron as shown in figure 5.1. The interaction sets the electron in motion with kinetic energy T at an angle ϕ ; the photon scatters at an angle θ with energy $h\nu'$. The energy of the scattered photon is given by

$$h\nu' = h\nu_0 \left(\frac{1}{1 + \alpha(1 - \cos\theta)} \right), \quad (5.1)$$

where α is given by $\frac{h\nu_0}{m_0c^2}$, the ratio of the incident photon energy to the electron rest mass energy. This function is graphed in figure 5.2 for an incident photon energy of 140 keV. The Klein-Nishina formula yields the differential number of photons

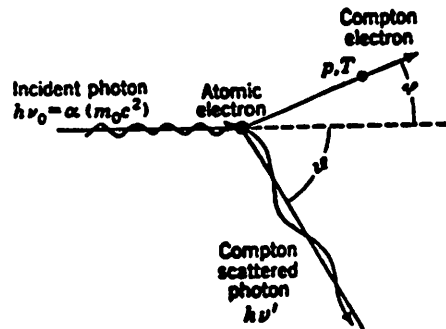


FIGURE 5.1: The Compton scattering process [78].

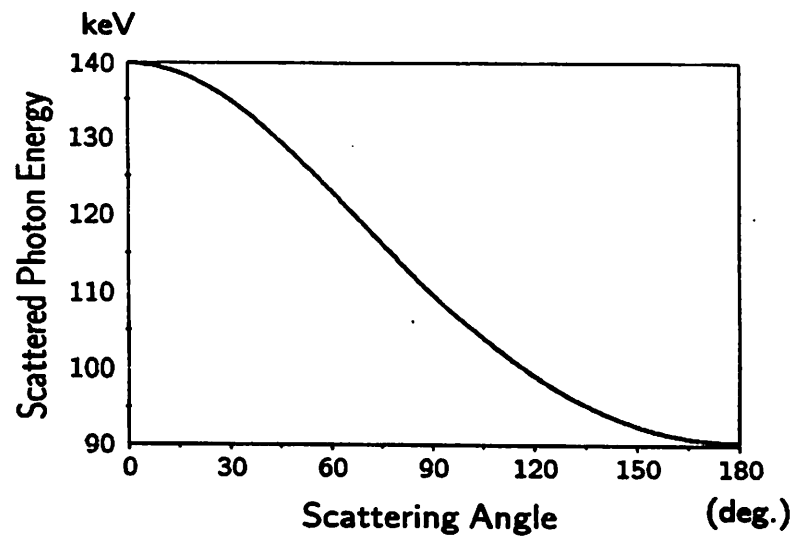


FIGURE 5.2: The relationship between the scattering angle and the energy of the scattered photon for an incident photon energy of 140 keV.

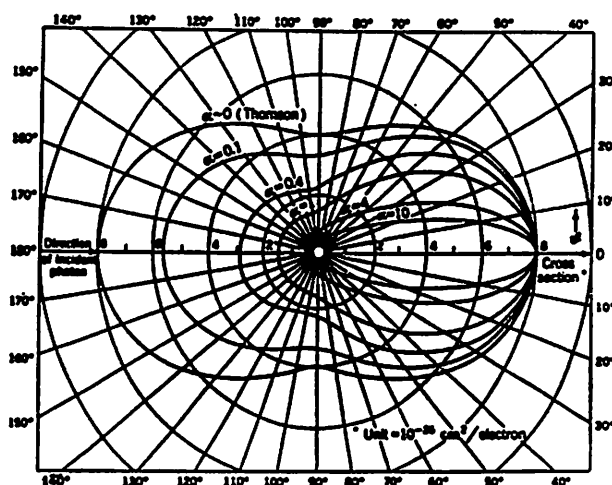


FIGURE 5.3: The number of photons scattered into unit solid angle as a function of the mean scattering angle θ [78].

scattered into a unit solid angle $\frac{d\sigma}{d\Omega}$ at a mean scattering angle θ :

$$\frac{d\sigma}{d\Omega} = \frac{r_0^2}{2} \left(\frac{\nu'}{\nu_0} \right)^2 \left(\frac{\nu_0}{\nu'} + \frac{\nu'}{\nu_0} - \sin^2\theta \right), \quad (5.2)$$

where r_0 is the classical electron radius [78]. Figure 5.3 is a polar plot of equation 5.2. Note that the distribution is somewhat forward peaked at diagnostic energies ($0.1 < \alpha < 1$). Thus, scattered photons do carry some useful spatial information, and complete scatter rejection may be undesirable.

5.2 Simulation Methods

5.2.1 Projection Data Analysis of a Myocardial Phantom

Because scatter is highly object-dependent, the problem must be restricted to a specific geometry. Myocardial perfusion imaging was chosen as a particularly important application of quantitative SPECT. The goal of SPECT perfusion studies is to quantitate the uptake of radionuclide in the heart muscle in order to estimate the

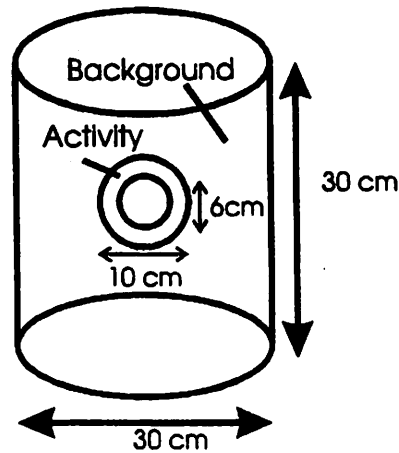


FIGURE 5.4: The myocardial simulation phantom. It consists of a spherical shell of radionuclide within a uniform cylindrical background.

amount of tissue perfusion from the coronary arteries. It is hoped that improvement in the quantitative accuracy of the measurement will lead to better risk classification of patients.

Figure 5.4 shows the cylindrically symmetric myocardial phantom that was used to generate data efficiently. The phantom consists of a spherical shell of radionuclide in the center of a water cylinder. The detector views the side of the cylinder. The inner and outer radii of the shell are 3 cm and 5 cm, respectively. The cylinder has a radius of 15 cm and is 30 cm long. The relatively small radius compensates for the lack of lungs in the phantom. A more anatomically accurate phantom would include air-filled cavities and would have a larger radius; it might also include a lower region of higher activity to represent radiopharmaceutical uptake in the liver. The target to background ratio is 5:1. The collimator's aspect ratio is 20:1, which matches the aspect ratio of the collimator in the ETCT system. The septal spacing is 0.17 cm, and the septal height is 3.3 cm. The distance from the center of the cylinder to the face of the collimator is 15 cm. The collimator has infinitesimally

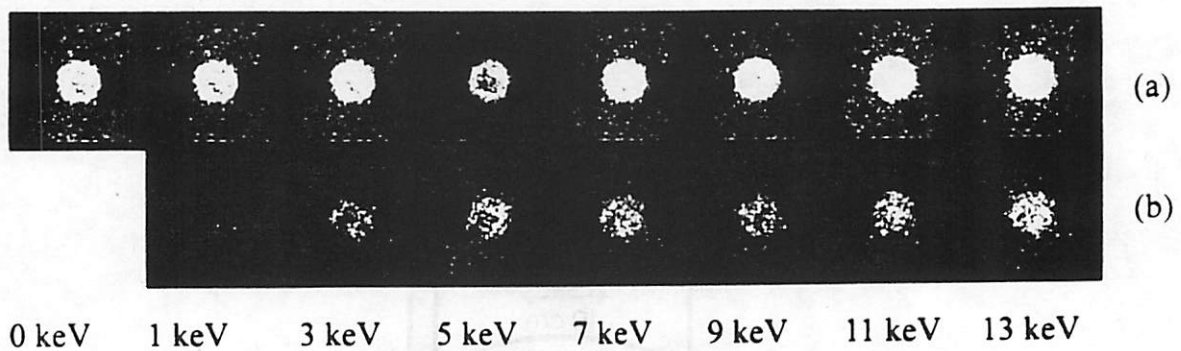


FIGURE 5.5: (a) Projection images at various energy resolutions. (b) The contribution of scatter to each image.

thin, but perfectly absorbing, walls. In other words, the geometric response of the collimator is included, but septal penetration is neglected.

With the assumption of a 140 keV photon energy (*i.e.* ^{99m}Tc) and photon transport in three dimensions, the EGS4 Monte Carlo Code was used to generate 90×90 pixel projections of the phantom at various detector energy resolutions. In order to simulate the effect of the detector energy resolution, the recorded spectra are blurred with a Gaussian kernel with an appropriate width. Photons are included in the image if they fall within a symmetric energy window centered around the photopeak. The window width is twice the full-width, half-maximum (FWHM) energy resolution. Low noise projection images containing approximately 2×10^7 primary counts were generated by using a very large number of photon histories (4×10^9). Projections with realistic count densities were then obtained by scaling and adding Poisson noise to these reference projections.

Sample projection images are shown in figure 5.5a. figure 5.5b shows the same projections with the primary counts removed. (Note that the images in the figure were rebinned to a 64×64 pixel grid for display purposes.) The projections were scaled consistently such that the projection corresponding to 13 keV FWHM en-

ergy resolution contained approximately 3×10^5 detected counts. Projection images obtained with better energy resolution contained fewer counts due to the narrower energy window. A projection containing only a large number ($> 2 \times 10^7$) of primary counts was also generated as a reference.

Rather than an immediate investigation of reconstructed images, the study was begun with an analysis of the projection data for several reasons. First, a quantitative comparison of scatter error to photon noise in reconstructed images is problematic because the reconstruction algorithm influences the propagation of noise into the final image. As a result, the image noise cannot be described by simple Poisson statistics [19], and it is difficult to assign noise variances to the images for the purpose of comparison. On the other hand, the projection data exhibits purely Poisson noise; a count measurement with mean N has variance N . Thus, a quantitative comparison is straightforward.

In addition, investigation of the projection data is sufficient to set a bound on the required energy resolution. The goal of this study is to determine the energy resolution at which the scatter error is statistically significant compared to the noise in the projection data. This level of energy resolution is most likely better than the level of energy resolution at which scatter error is statistically significant compared to noise in the reconstructed images. Because reconstructed images have higher noise levels (due to the effect of the reconstruction), more scatter can be tolerated. In other words, an investigation of the projection data provides a bound to the required energy resolution.

In order to analyze the myocardial phantom data, the projection images were compared to the reference image using a chi-squared measure defined by

$$\chi^2 = \sum_i \frac{(\alpha N_{i,ref} - N_{i,proj})^2}{\alpha^2 N_{i,ref}} \quad (5.3)$$

where $N_{i,ref}$ and $N_{i,proj}$ are the number of counts in the i^{th} pixel of the reference and projection images, respectively. The scaling constant α accounts for the fact that the total number of counts varies in the projection images; it is chosen in such a way as to minimize χ^2 . Differentiation of equation 5.3 yields

$$\alpha = \frac{\sum_i \frac{N_{i,proj}^2}{N_{i,ref}}}{\sum_i N_{i,proj}}. \quad (5.4)$$

5.2.2 Image Reconstructions of a Myocardial Phantom

Although projection data provides some useful information, a quantitative comparison of scatter error to attenuation and collimator errors demands analysis of reconstructed images. Replication of the reference projection data with appropriate levels of added noise produced data sets suitable for reconstruction. Images were reconstructed using an iterative maximum-likelihood expectation-maximization (MLEM) algorithm. A novel feature of the code is the inclusion of a multi-ray integrator that accurately models the collimator response in order to improve the spatial resolution [11]. Images were reconstructed under various conditions: with and without attenuation correction, with and without collimator response, with and without added noise, and with various levels of energy resolution. Reconstructions including the collimator response were run for 100 iterations; 30 iterations were used to reconstruct images without collimator response. Figure 5.6 shows two sample images. The image on the left is a “best-case” reference image that was reconstructed with perfect attenuation correction, accurate collimator response, low noise, and perfect energy resolution. On the other hand, the image on the right was formed without corrections from noisy (*i.e.* low count density) data with the assumption of 13 keV FWHM energy resolution. There are approximately 500,000 counts in the data set. Clearly, it is difficult to determine the individual contribution of scatter to

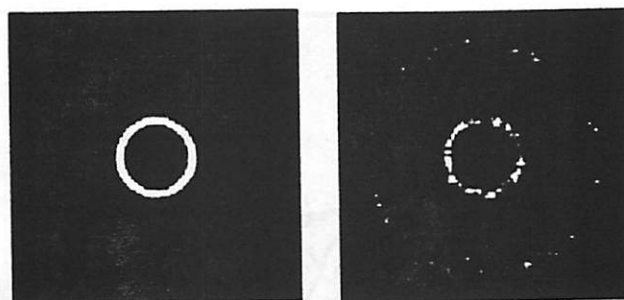


FIGURE 5.6: Reconstructed images. The image on the left is a “best-case” reconstruction, while the image on the right is degraded by attenuation, scatter, collimator blur, and noise.

the degradation in this more realistic image. Thus, the ability to separate physical effects through simulations proves to be quite useful.

5.2.3 Point-Spread-Function Simulations

The results of the simulation study apply only to the specific myocardial phantom shown in figure 5.4. Further Monte Carlo simulations were used to predict how the result would change for larger or smaller phantoms. In this part of the study, the EGS4 code was used to generate the point spread function (PSF) of a radiomimetic point source imbedded in the middle of a slab of water-equivalent scattering material. In order to decrease the computational burden, the collimator response was modeled by weighting the photon detection by a Gaussian function of the angle of incidence; the parameters of the Gaussian function were chosen to correspond to a 20:1 collimator. PSF's were generated for different detector energy resolutions and different thicknesses of scattering material. The source-to-detector distance was kept constant as the slab thickness increased. Sample PSF's are shown in figure 5.7. A thickness of x cm corresponds to a point source in the middle of a $2x$ thick slab; thus, back-scatter is included in the measurements. Note that the central peak of the

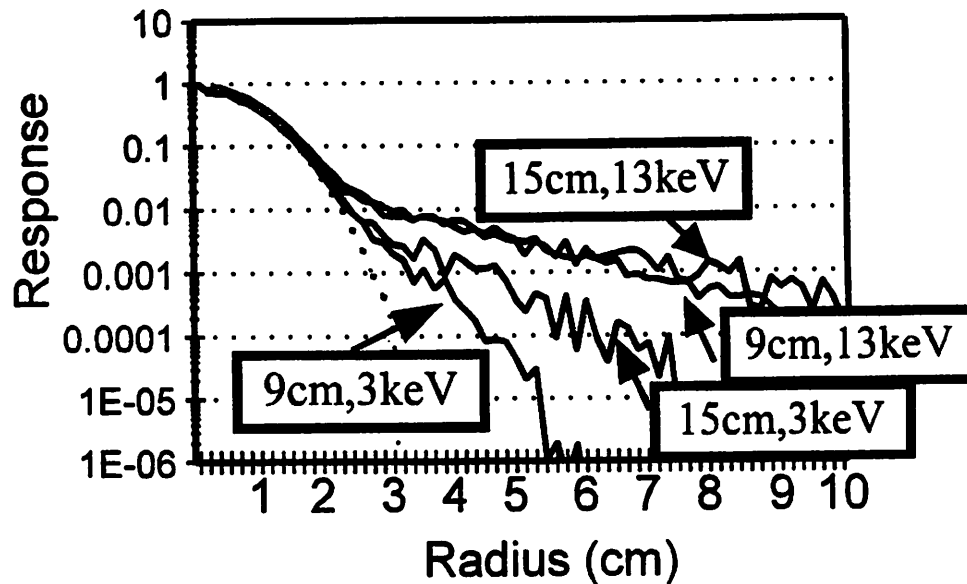


FIGURE 5.7: The point spread functions corresponding to a ^{99m}Tc point source imbedded in a slab of scattering material for various slab thicknesses and detector energy resolutions. The dotted line shows the geometrical response due to the collimator.

point spread function is dominated by the collimator response. Scatter contributes long tails to the distribution; the tails grow broader as the thickness of the scattering material increases and as the energy resolution deteriorates. These tails result in variations in the scattering distribution and, hence, quantitative variation in the projection data. The variation in the point spread function allows the prediction of scatter variation with object size.

5.3 Results

5.3.1 Projection Data Analysis

Fifty projection images containing approximately 2.3×10^5 primary counts were generated for energy resolutions ranging from 0 to 14 keV FWHM, and values of

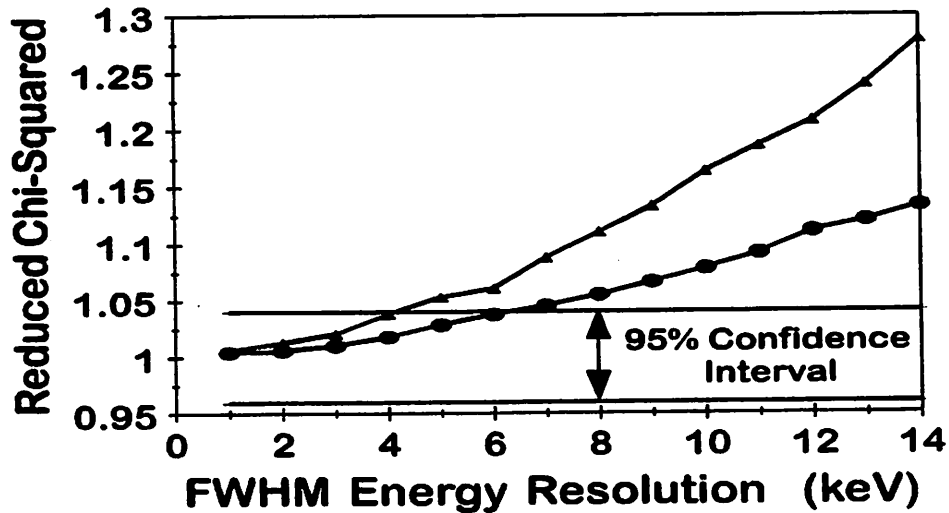


FIGURE 5.8: A plot of the average value of χ^2 representing the match between projection images and a reference primary image. The bottom curve shows the results for approximately 2.3×10^5 counts in each projection image, and the top curve corresponds to approximately 4.6×10^5 counts in each image. The confidence interval represents the uncertainty due to Poisson noise.

χ^2 were calculated from equation 5.3 for each image. Figure 5.8 shows the average reduced values of χ^2 as a function of the simulated detector energy resolution. The results can be understood as follows. Due to Poisson noise, the value of χ^2 will vary from projection to projection even with perfect energy resolution. The confidence interval shown in the figure is defined such that the value will fall within the interval 95% of the time if scatter is not a factor [79]. For points outside the confidence interval, one can reject with probability $p < 0.05$ the hypothesis that the projection image is consistent with the reference image. For relatively poor energy resolution, the error due to scatter overwhelms the uncertainty due to Poisson noise. Thus, the value of χ^2 lies well outside the confidence interval and reflects the mismatch between the scatter-corrupted image and the reference image. As the energy resolution of

the system improves, the relative effect of scatter decreases. With excellent energy resolution, the error due to scatter becomes negligible, and Poisson noise determines the quantitative uncertainty. As figure 5.8 shows, 3-4 keV FWHM energy resolution is sufficient to ensure that the average value of χ^2 falls well within the confidence interval. Thus, at this energy resolution, it is possible to neglect the effect of scatter on quantitation for this phantom geometry.

An advantage of the χ^2 statistic is that it is normalized to its expected value. Thus, there is an approximately equal contribution to χ^2 from all parts of the image. In other words, although χ^2 was calculated by summing over all pixels in the image, the results were essentially unchanged if only pixels in a small region centered on the "myocardium" were used.

The upper curve in figure 5.8 shows data obtained by repeating the simulations with approximately 4.6×10^5 primary counts in each projection image. Because the Poisson noise is lower, better energy resolution is required in order to render the scatter bias small with respect to the statistical uncertainty. The scaling of the required energy resolution can be estimated as follows. Suppose that the number of primary counts in the projection image is denoted by P , and the FWHM energy resolution is denoted by ΔE . The number of scatter counts in the image, given by S , is an approximately linear function of the energy resolution [54]; *i.e.*

$$S = \beta \Delta E P \quad (5.5)$$

where β is a proportionality constant. At some energy resolution ΔE_0 , the scatter component of the image is equal to the uncertainty due to Poisson noise; in other words,

$$\beta \Delta E_0 P = \sqrt{P}. \quad (5.6)$$

Solving for ΔE_0 yields

$$\Delta E_0 = \frac{1}{\beta\sqrt{P}}. \quad (5.7)$$

Thus, the energy resolution required to render scatter negligible compared to Poisson noise varies approximately inversely with the square root of the number of primary counts in the projection image. For example, figure 5.8 shows that doubling the number of counts calls for a factor of $\sqrt{2}$ improvement in the energy resolution.

5.3.2 Analysis of Reconstructed Images

Figure 5.9 shows profiles of reconstructed images which illustrate the effect of various perturbations. While profile 'a' corresponds to the "best-case" reference image described above and shown in figure 5.6, the other profiles are taken from images degraded by one single physical perturbation. For instance, profile 'b' is taken from an image that was not corrected for attenuation (but otherwise matched case 'a'). In addition to producing a very low estimate of the true activity, attenuation leads to a cupping artifact in the image; activity in the center of the cylinder is suppressed relative to activity at the borders. Profile 'c' corresponds to an image reconstructed without compensation for the collimator response; it can be seen that the collimator leads to a broadening of the radionuclide distribution. An energy resolution of 13 keV FWHM was used to generate profile 'd', which shows that scatter results in a capping artifact as well as some broadening of the activity in the myocardial region. Finally, profile 'e' shows that noise due to poor photon statistics leads to large fluctuations in the measured activity distribution; in this case, the image contained approximately 5×10^5 counts.

The images were automatically segmented in order to separate the "myocardium" from the background, and annular ROI's were used to determine activity levels.

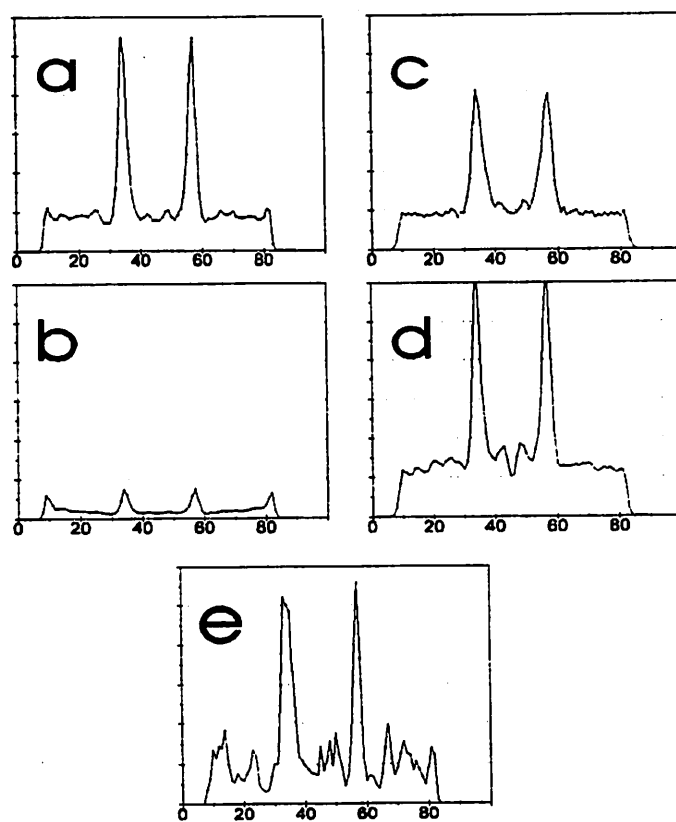


FIGURE 5.9: Profiles taken across the reconstructed images for various cases. Case 'a' is a reference image; cases 'b'-'e' show the effect of collimator blur, attenuation, scatter, and photon noise, respectively.

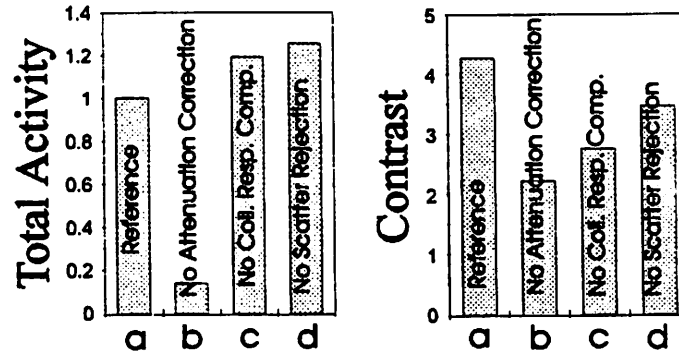


FIGURE 5.10: The effect of various errors on measurements of total myocardial activity and contrast. Case 'a' corresponds to no perturbation; cases 'b', 'c', and 'd' reflect only one perturbation.

The outer edge of the myocardium was determined adaptively from histograms of pixel values, and a simple threshold of 35% of the maximum activity was used to determine the inner edge. The left side of figure 5.10 shows the total activity in the myocardial ROI for the cases discussed above. Attenuation clearly represents the largest perturbation in the radionuclide measurement. Scatter and collimator blur contribute errors of similar magnitude.

Although the absolute total activity in an ROI is a potentially important parameter in a quantitative study, relative quantitation (or contrast) is often more important. The right side of figure 5.10 shows the target-to-background ratio for each case. This ratio is sensitive to the particular method used to define the ROI; so, even the reference case does not exactly reproduce the 5:1 target to background ratio in the phantom. The background was measured in an annular ROI approximately 4 cm from the outer edge of the phantom. Both scatter and collimator lead to a loss of contrast because activity in the myocardium is smeared into the background region.

An important consideration is the change in measured activity as the energy

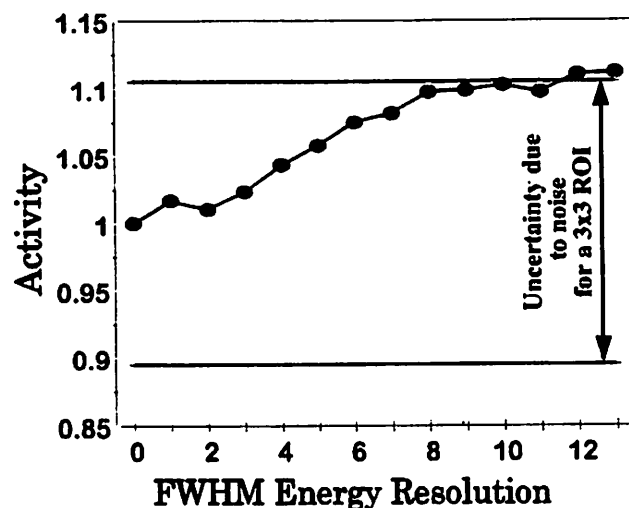


FIGURE 5.11: Mean activity in the myocardium as a function of system energy resolution. The error bar shows the uncertainty due to noise.

resolution improves. Figure 5.11 shows the mean activity in the myocardial ROI as a function of the simulated energy resolution. The approximately linear rise in mean activity with decreasing energy resolution (increasing FWHM) is consistent with the observation that the scatter fraction is approximately a linear function of the energy resolution. The drop in slope beyond 8 keV energy resolution is a consequence of the segmentation routine used to define the ROI; it was not observed for other segmentation techniques (*e.g.* a fixed ROI).

Although the error due to scatter decreases as the energy resolution improves, at some point this improvement is inconsequential since it is overwhelmed by the statistical uncertainty introduced by photon noise. This uncertainty was estimated by reconstructing 100 different data sets containing a realistic number ($\approx 3.5 \times 10^5$) of only primary counts. This number corresponds to approximately 5×10^5 total counts at 13 keV FWHM energy resolution. For each reconstruction, fixed ROI's of various sizes were used to determine a myocardial activity. The ROI's were

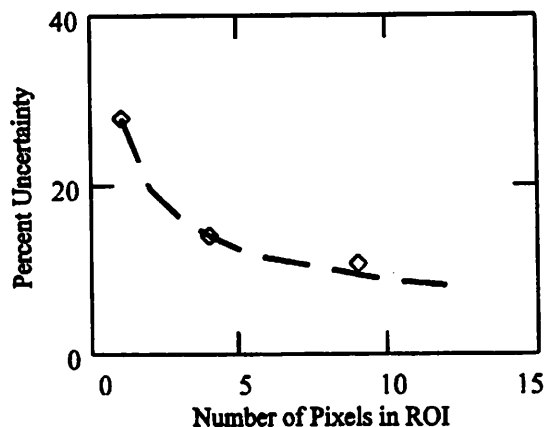


FIGURE 5.12: Statistical uncertainty as a function of ROI size.

placed in the center of the known myocardial region. The standard deviation of these measurements across the 100 realizations yields an estimate of the statistical uncertainty in the measured activity. The arrow in figure 5.11 corresponds to a plus or minus one standard deviation error bar for measurements made with an ROI containing 9 pixels. This size ROI is approximately equivalent to the effective area of averaging for the smoothing filters that are typically applied in clinical perfusion studies. At approximately 5 keV, the scatter error is small compared to the statistical uncertainty.

The statistical uncertainty is obviously a function of the ROI size. Figure 5.12 shows the standard deviation of the activity measurement for various ROI sizes. As indicated by the dashed line, the uncertainty varies as the inverse of the square root of the number of pixels in the ROI. In other words, the noise in adjacent pixels is approximately independent. Not shown in the graph are additional values of 2.8% and 2.3% for 100 and 152 pixel ROIs, respectively, that further confirm the $\frac{1}{\sqrt{N}}$ dependence.

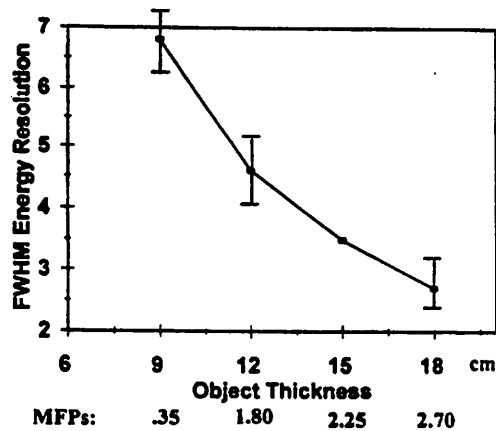


FIGURE 5.13: A plot of the FWHM energy resolution needed to maintain a point spread function equal to that of a point source imbedded in 15 cm of scattering material measured with 3.5 keV FWHM energy resolution. The x -axis is labelled in units of mean free path, as well as in centimeters.

5.3.3 Point Spread Function Analysis

For analysis of the point spread data, the PSF corresponding to 3.5 keV and 15 cm thickness was chosen (somewhat arbitrarily) as a reference. The energy resolution required to give an essentially identical point spread function for different thicknesses of scattering material was then determined. The results are shown in figure 5.13. Qualitatively, one can conclude that smaller objects require less energy resolution to maintain the same level of error due to scatter. Because the x -axis of figure 5.13 is labelled in mean-free-path (MFP) units, one can also gauge how the energy-resolution requirements vary with photon energy by knowing the size of the object relative to the MFP of the photon energy of interest.

The results of the PSF simulations show the variation of energy resolution requirements with object size. Because smaller objects produce less scatter, they can be accurately imaged with less energy resolution. Thus, for example, because the thorax is larger than the head, a cardiac imaging system requires better energy resolution than a brain imaging system in order to achieve the same level of

performance.

5.4 Conclusion

The simulation results presented in this chapter lead to several preliminary conclusions about the relative importance of scatter in quantitative ^{99m}Tc SPECT imaging. First, figure 5.10 shows that attenuation is clearly the largest perturbation on the radionuclide measurement. In addition, for the thresholding choice evaluated, the errors in total activity and in contrast due to collimator blur are comparable in magnitude to the scatter error at the 13 keV energy resolution of clinical gamma cameras. Thus, accurate compensation for attenuation correction and collimator response is necessary if one hopes to gain an advantage by improving the energy resolution of SPECT systems.

Next, figures 5.8 and 5.11 provide a comparison of scatter error to photon and reconstruction noise. The χ^2 test provides a bound on the energy resolution needed to render the scatter error small compared to the statistical uncertainty. For the myocardial phantom, an image reconstructed with 0.5 keV energy resolution will be qualitatively indistinguishable (other than a scaling factor) from an image reconstructed with 3.5 keV energy resolution due to random fluctuations. The same statement holds true for the quantitative value of a single pixel. Although the χ^2 test is easy to apply, it is insufficient to consider the statistical uncertainty in the activity of a region of interest in a reconstructed image. In this case, reconstruction of 100 different realizations of the phantom data revealed that an energy resolution of 5 keV is adequate to render the statistical error small in comparison to the statistical error for an ROI size typical of myocardial perfusion studies. This estimate

accounts for the fact that the reconstruction process tends to increase the noise, while averaging over a region decreases the uncertainty.

Further discussion of the role of scatter in SPECT will be given following the presentation of experimental results in the next chapter.

Chapter 6

Experimental Studies of Scatter

Although simulations represent a useful approximation of the SPECT imaging process, experimental work is necessary in order to truly demonstrate the effect of scatter on quantitation. With low-noise electronics, the ETCT system represents a unique “gold-standard” instrument for quantitative measurements. While the electronics offer excellent scatter rejection, the x-ray transmission source yields data for object-specific attenuation correction. In addition, iterative reconstruction algorithms provide a means of correction for the diverging field of view of the collimator. This chapter describes preliminary imaging experiments aimed at assessing the value of scatter rejection for the ETCT system. In particular, images of a concentric-cylinder phantom, a cold-lesion phantom, and a thorax-like phantom were analyzed; these three phantoms were chosen to evaluate the effect of scatter on quantitative accuracy, contrast, and spatial resolution, respectively. In addition, scatter rejection was compared to two scatter correction techniques. The chapter ends with a discussion of the relative importance of scatter for SPECT imaging.

6.1 Methods

Three phantoms were chosen for this experimental study: a concentric-cylinder phantom, a cold-lesion phantom, and a thorax-like phantom. Figure 6.1 shows cross-sectional images of each phantom. The concentric-cylinder phantom includes a cylindrical central chamber within a concentric cylindrical background. The inner diameter of the central chamber is 5.35 cm, and the outer diameter is 6.00 cm. The inner and outer diameters of the cylindrical tank are 19.4 and 20.0 cm respectively, and the height is 20 cm. The wall material is methyl methacrylate, which is roughly tissue-equivalent. To obtain images, the chambers were filled with a 43 mCi ^{99m}Tc -pertechnetate solution such that the target-to-background concentration ratio was approximately 5:1.

The cold-lesion phantom comprises a water-filled cylinder and 7 acrylic rods parallel to the cylinder axis. Since the rods displace activity, they represent cold spots. The diameter of the outer tank is 20.0 cm; its height is 10 cm. The central rod has a diameter of 22.2 mm, and the diameters of the outer rods are 6.0, 7.4, 9.1, 11.5, 14.3, and 18.0 mm. A 40 mCi ^{99m}Tc pertechnetate solution filled the main tank during imaging experiments.

The thorax phantom is contained in a 20.0 cm diameter, 10 cm-tall cylindrical acrylic tank. Along one diameter, the outer tank contains three smaller cylinders, each with inner diameters of 4.32 cm, centered at 0.00 cm and ± 6.35 cm from the center of the outer tank. The peripheral cylinders contain air to simulate lungs, and the central chamber contains water to simulate the myocardium and blood-pool. Two Teflon rods are included along the diameter perpendicular to that of the three inner chambers in order to simulate spine and sternum. The rods have diameters of 2.54 cm and are located at ± 5.08 cm from the center of the outer tank. The inner

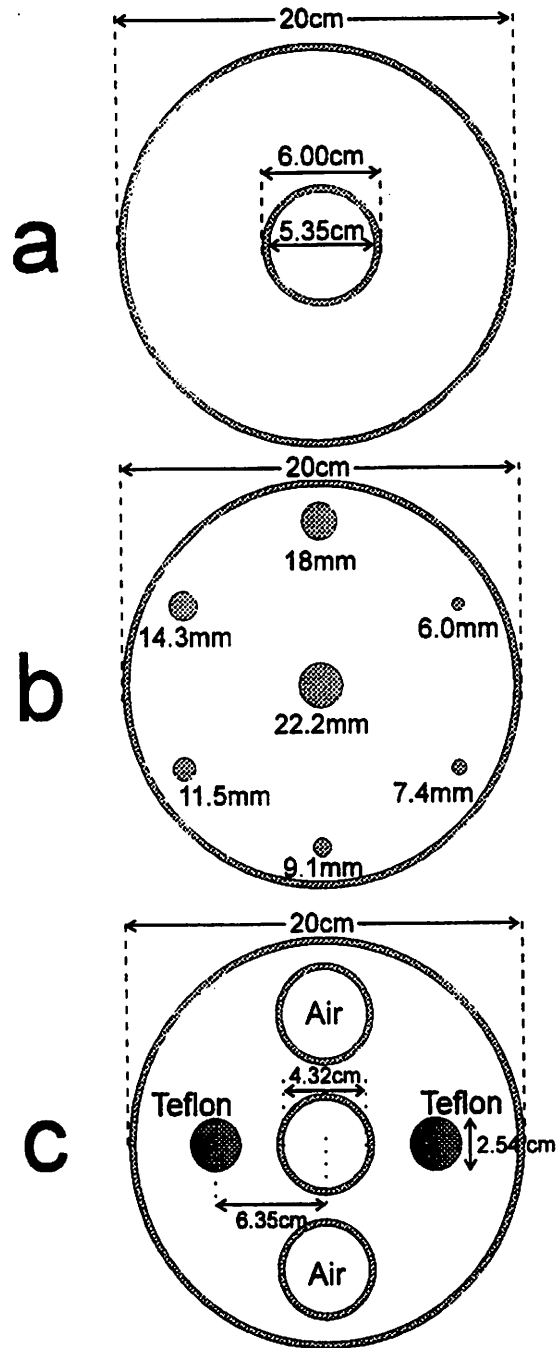


FIGURE 6.1: Phantoms used in the experiments. (a) A concentric-cylinder phantom. (b) A cold-lesion phantom. (c) A thorax-like phantom.

and outer chambers were filled with 5.6 mCi and 22.4 mCi of ^{99m}Tc -pertechnetate in order to yield a target-to-background concentration ratio of 5:1 for the image acquisition.

The phantoms were mounted such that the cylindrical axis coincided with the isocenter of the ETCT system, and data were collected with a single-channel of low-noise electronics connected to the central element of the HPGe detector array. Because the noise performance of the triple-mode IC was less than originally desired, commercial electronics were used for most experiments. The commercial electronics included a Tennelec TC170 JFET preamplifier and a Canberra 1416B shaping amplifier with a 2.5 μsec shaping time. Note that the commercial electronics are suitable for SPECT data collection but cannot be used for CT measurements. Signals from the shaping amplifier were sent to an Oxford PCAII multi-channel analyzer (MCA). The MCA recorded spectral information from approximately 90 keV to 160 keV for each detector position. The commercial electronics achieved an energy resolution of approximately 2.5 keV FWHM at 140 keV.¹ One goal of the experiments was to use the superior performance of the commercial electronics in order to determine whether the performance of the triple mode chip is adequate for the ETCT system. The concentric cylinder phantom was imaged with both sets of electronics in order to verify operation of the triple-mode chip. The chip achieved an energy resolution of 4.5 keV when coupled to the MCA with the entire system (*i.e.* computer, stepper motors, etc.) running. Because only a single channel of electronics was available, the SPECT studies took approximately 7 hours.

The collected spectra were blurred and windowed in order to simulate various lev-

¹The energy resolution of the commercial electronics provide further evidence of a poor grounding scheme as described in chapter 2 . One would normally expect the energy resolution of the HPGe detector to be approximately 1-1.5 keV when used with a discrete JFET preamplifier.

els of energy resolution. The radionuclide tomographs were reconstructed with an iterative maximum-likelihood expectation-maximization (ML-EM) algorithm that could include both object-specific attenuation correction and accurate collimator response compensation [11]. Rather than collect x-ray transmission data, attenuation maps were generated from the known phantom geometries. Since attenuation correction is largely a solved problem with the ETCT system [25], this procedure is not a drawback for the experiments.

6.2 Results

6.2.1 The Concentric Cylinder Phantom

The concentric cylinder phantom was chosen to evaluate the quantitative error introduced by photon scatter. Because the phantom is circularly symmetric, the projections can be added together in order to create a single low-noise reference projection. Multiple realizations can be generated by replicating this reference projection with appropriate levels of added noise. These multiple realizations then permit evaluation of statistical uncertainty. In particular, a comparison to the previous chapter's simulation results was desired. Figure 6.2 shows three images of the phantom. The image on the left was acquired with commercial electronics with 2.5 keV energy resolution, and the middle image was obtained with the triple-mode IC with 4.5 keV energy resolution. The image on the right was generated by blurring and windowing the 2.5 keV data in order to simulate the 12 keV FWHM energy resolution typical of commercial scintillation cameras.

In order to assess the quantitative accuracy as a function of energy resolution, the data were blurred and windowed to simulate various noise levels. Images were

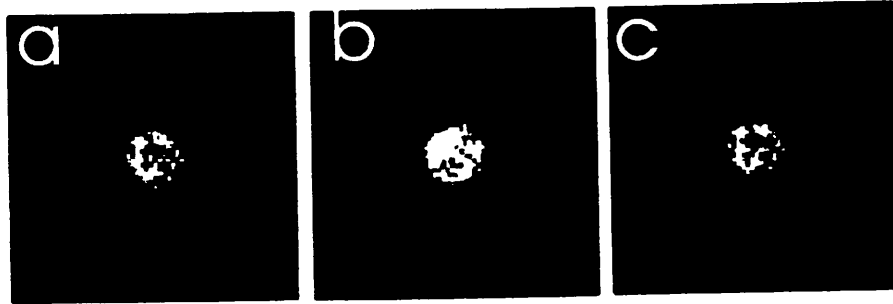


FIGURE 6.2: Concentric cylinder phantom images. The image on the left was obtained with 2.5 keV energy resolution using commercial electronics, and the middle image was acquired with 4.5 keV using the triple mode IC. The image at the right was obtained by blurring and windowing the 2.5 keV data in order to simulate 12 keV energy resolution.

reconstructed with the ML-EM algorithm including attenuation correction and collimator compensation, and the activities in a 9-pixel ROI near the edge of the inner cylinder were determined. The solid line in figure 6.3 shows the results; the dotted line is a linear extrapolation of the activity to ideal energy resolution. The dashed line in the figure shows the results when attenuation correction is not included in the reconstruction. Clearly, attenuation is a far more significant error than scatter. The error bars in the figure reflect the statistical uncertainty in the ROI activity; they are located at plus or minus one standard deviation as determined from 100 realizations of the 2.5 keV data. Since the noise is not a strong function of energy resolution, the uncertainty would be similar with ideal energy resolution. At 2.5 keV energy resolution, the scatter error is small compared to the statistical noise.

The previous chapter's simulation results predicted that 5 keV FWHM energy resolution is sufficient to render the scatter error small compared to the statistical noise. In order to compare the experimental result to simulation results, adjustment factors must be estimated to account for differences in count densities and geometry. The number of photons that contribute to the activity in a particular ROI is

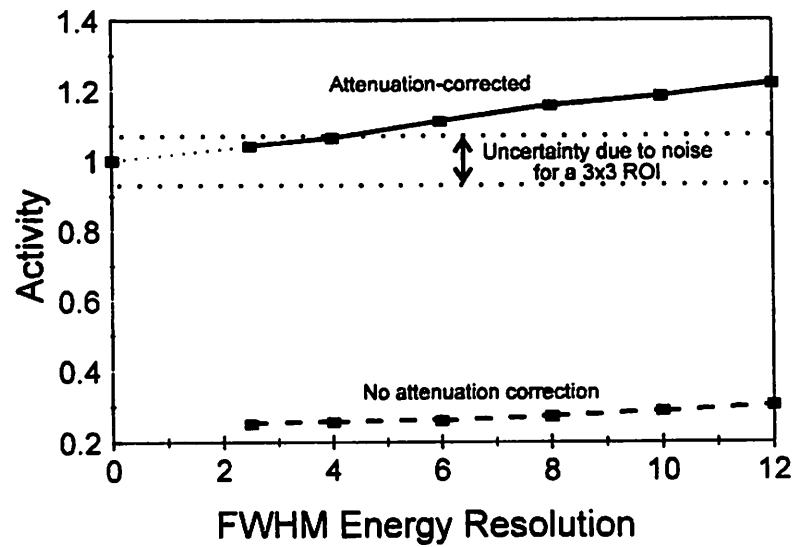


FIGURE 6.3: The activity in a 9-pixel ROI near the edge of the inner cylinder is plotted as a function of energy resolution; the dotted line is a linear extrapolation to ideal energy resolution. The error bars are located at plus or minus one standard deviation as determined from 100 realizations at 2.5 keV energy resolution. The dashed line shows the results when attenuation correction is not included in the reconstruction.

approximately

$$N_{contrib} = N_{total} \left(\frac{\sum_{ROI} \lambda_i p_i}{\sum_{Image} \lambda_i p_i} \right), \quad (6.1)$$

where N_{total} is the total number of counts in the image; λ_i is the activity in the i^{th} pixel, and p_i is the probability that a photon emitted from the i^{th} pixel is actually detected. The value of p_i is estimated during the ML-EM reconstruction process. Application of equation 6.1 indicates that approximately 2500 photons contribute to the ROI activity in the experimental measurements, and approximately 1000 photons contribute to the simulated ROI. Chapter 5 showed that the energy resolution needed to maintain a consistent ratio of scatter error to statistical uncertainty varies as the square root of the number of counts in the measurement.

Although the diameter of the experimental concentric-cylinder phantom (20 cm) is less than that of the simulated myocardial phantom (30 cm), there is a greater concentration of activity near the center of the experimental phantom; thus, the effective scattering sizes of the two phantoms are similar. This effective distance can be estimated by calculating a mean radial distance from an emission point to the surface of the outer cylinder for the two phantoms. The calculation yields an “effective scattering length” of 4.6 cm for the experimental phantom and 5.4 cm for the simulated phantom. Figure 5.13 shows that the energy resolution needed to maintain a particular level of performance scales roughly as the $\frac{5}{4}$ power of the object size.

These two adjustment factors allow the scaling of the simulation results to predicted experimental results according to

$$\Delta E_{pred} = (5 \text{ keV}) \left(\frac{1000}{2500} \right)^{0.5} \left(\frac{5.4}{4.6} \right)^{1.25} = 3.9 \text{ keV}, \quad (6.2)$$

where ΔE_{pred} is a prediction of the energy resolution needed in order to ensure that the scatter error is small compared to the statistical noise. Thus, the experimental

measurements indicate that scatter is somewhat more important than indicated by simulations. This discrepancy arises because the experimental measurements include additional scatter produced in the collimator and in the detector housing, which increases the scatter fraction by approximately 25% in the ETCT system. The effect is exacerbated by the small size of the ETCT detector. In a conventional Anger camera, the detector covers a large area; so, there is very little scatter from the detector housing into the projection image plane. Also, the count density of the experimental data is rather high. Thus, the level of statistical noise calls for relatively good energy resolution.

Although this analysis includes quantitative estimates of the energy resolution needed to render the scatter error statistically insignificant, it must be emphasized that these numbers are simply rough estimates. There will, of course, be object-specific variation. The point of the analysis is that an energy resolution of a few keV is sufficient to ensure that the scatter error is small compared to the statistical uncertainty. Even at moderate energy resolutions (6-8 keV), the scatter error is often comparable to the uncertainty. Thus, for quantitative SPECT tasks, there is no benefit offered by arbitrary improvement of the energy resolution.

6.2.2 The Cold-Lesion Phantom

The cold-lesion phantom images reveal the effect of scatter on contrast and signal-to-noise ratios. Attenuation-corrected images were reconstructed with various levels of energy resolution both with and without accurate collimator response. Figure 6.4 shows images corresponding to 2.5 keV and to 12 keV energy resolution without collimator response included.

An automatic segmentation routine was used to distinguish the lesions from the

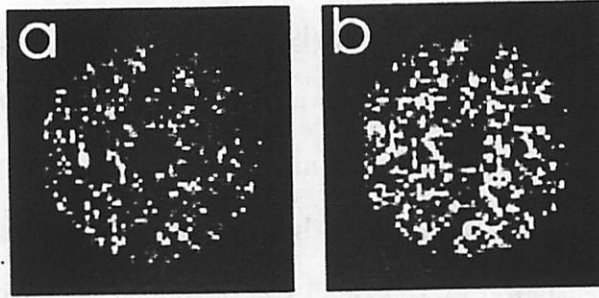


FIGURE 6.4: Images of the cold lesion phantom at (a) 2.5 keV and (b) 12 keV energy resolution.

background area. The algorithm involves first locating minima in circumferential profiles in order to identify the locations of lesions and of background regions. The mean and standard deviation of the background activity are then determined. Any pixels with an activity less than 2.5 standard deviations below the mean are identified as part of the lesions. The contrast C_i and the signal-to-noise ratio S_i of the i^{th} lesion are then determined according to

$$C_i = \frac{\mu_B - \mu_i}{\mu_B} \quad (6.3)$$

and

$$S_i = \frac{\mu_B - \mu_i}{\sigma_B}, \quad (6.4)$$

where μ_i is the mean activity in the i^{th} region; μ_B is the mean background activity, and σ_B is the standard deviation of the background activity. Alternatively, the minimum activity within a lesion can be used to define the contrast and SNR.

Figure 6.5 shows the lesion contrast as a function of diameter for 3 keV and 12 keV energy resolution. While the left side corresponds to images which were reconstructed without collimator compensation, the right side shows data which include collimator compensation. Although improved energy resolution clearly yields some improvement in contrast, collimator compensation has a greater effect, par-

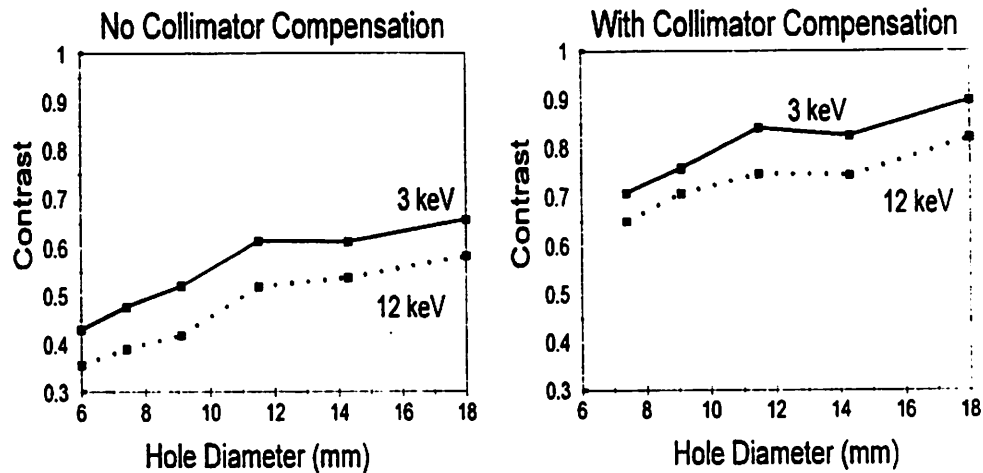


FIGURE 6.5: Contrast as a function of lesion size for 3 keV and 12 keV energy resolution. While the data on the left does not include collimator response compensation, the graph on the right corresponds to reconstructions with the compensation included.

ticularly for the smallest holes. Thus, the primary determinant of contrast is the limited spatial resolution of the collimator.

Figure 6.6 shows the signal to noise ratio as a function of energy resolution for various hole diameters. As the energy resolution improves, the signal level becomes higher due to the improved contrast. However, the noise level also increases somewhat because there are fewer photons in the image. The net result is that the SNR has a rather weak dependence on energy resolution.

6.2.3 The Thorax Phantom

Images of the thorax phantom provide an indication of the spatial extent of the scatter error. Figure 6.7 shows images corresponding to 2.5 keV and 12 keV FWHM energy resolution. Note that the largest scatter perturbation is the spill-in of activity into the Teflon rods, where there are voids in the actual radioactivity

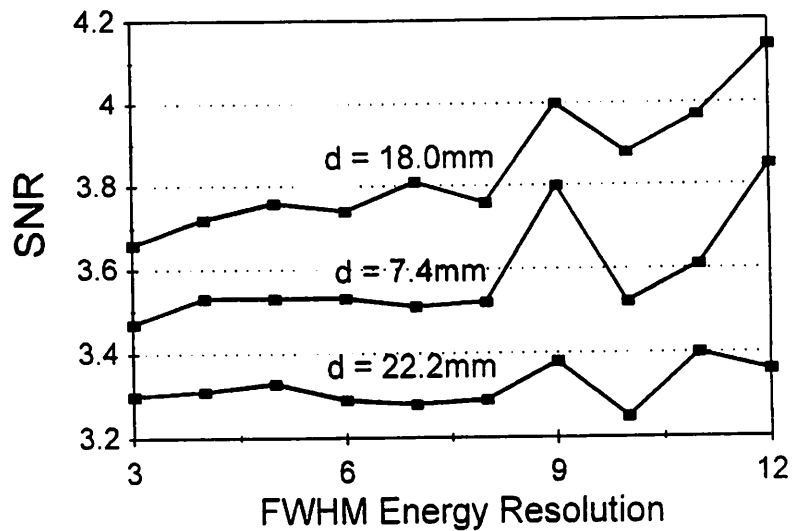


FIGURE 6.6: The SNR as a function of energy resolution for the cold lesion phantom. Results are shown for three different lesion sizes.

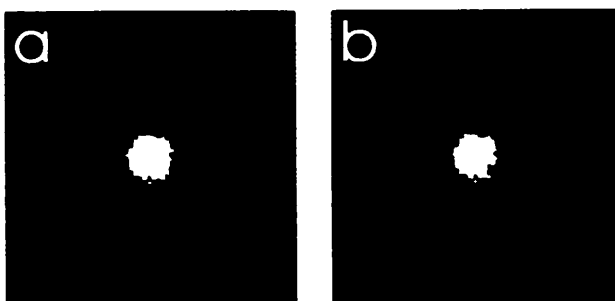


FIGURE 6.7: Images of the thorax phantom at (a) 2.5 keV and (b) 12 keV energy resolution.

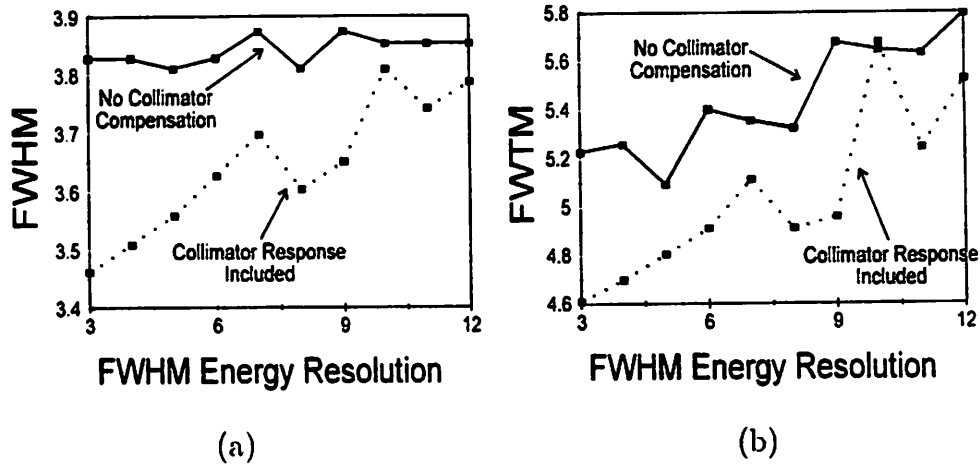


FIGURE 6.8: The full-width of the central region of the thorax phantom at (a) one-half and (b) one-twentieth of the maximum value after background subtraction. The results with and without collimator response are shown. Note that the inner diameter of the central chamber is 4.32 cm.

distribution.

The average full width of the central myocardial region was calculated as a function of energy resolution at both half of the maximum value and one-twentieth of the maximum value after background subtraction. Figure 6.8 shows the results with and without collimator compensation. While the full-width, half-maximum (FWHM) value depends weakly on the energy resolution, the full-width, twentieth-maximum value varies somewhat more strongly with energy resolution. In other words, the collimator is the primary determinant of the spatial resolution, but scatter contributes long tails to the image.

6.3 Scatter Correction vs. Scatter Rejection

Scatter rejection is a unique capability of the ETCT system. With conventional SPECT systems, scatter correction is necessary in order to alleviate the scatter error. Because scatter rejection decreases the number of photons in the image, it tends to increase the noise in the image. Similarly, subtraction techniques for scatter correction can also increase the noise in the image. Thus, it is interesting to compare the noise properties of scatter correction to scatter rejection.

In this study, two scatter-correction schemes were employed. The first is the well known dual energy window subtraction method [14]. With this method, counts are recorded both in the photopeak-energy window and in a low-energy (scatter) window. A fraction of the counts in the lower-energy window is then subtracted from the higher-energy window on a pixel-by-pixel basis in the projection data. The fraction is determined empirically. In this implementation, the technique was applied to data which simulated 12 keV energy resolution. Thus, the photopeak window ranged from 128 to 152 keV; the scatter window ranged from 110 to 125 keV, and the fraction was chosen somewhat arbitrarily to be 0.65. Since any practical scatter-correction technique must be robust for a range of operating conditions, no attempt was made to optimize these parameters.

The second method incorporates an estimate of the scatter distribution directly in the back-projector of the ML-EM algorithm as follows:

$$\lambda_{n+1}(b) = \frac{1}{\sum_{d=1}^{N_d} p(b, d)} \sum_{d=1}^{N_d} N(d) \left(\frac{p(b, d) \lambda_n(b)}{S(d) + \sum_{b'=1}^{N_b} p(b', d) \lambda_n(b')} \right), \quad (6.5)$$

where $\lambda_n(b)$ is the n^{th} iterative estimate of the activity in voxel b , $N(d)$ is the number of counts detected in projection d , and $p(b, d)$ is the probability that a photon emitted from voxel b is detected in projection d . The total number of projections in

the data is given by N_d , and the total number of voxels in the reconstructed image is N_b . This equation differs from the conventional ML-EM algorithm in that it includes a term $S(d)$, which is an estimate of the number of scattered photons detected by detector d in the primary energy window [10, 80]. The scatter sinogram $S(d)$ was estimated as 65% of the low energy window as above. Because the algorithm does not involve data subtraction, it achieves better noise performance than the dual energy window method.

Images of the cold-lesion phantom were reconstructed including attenuation correction for four cases: 3 keV energy resolution, 12 keV energy resolution with no scatter correction, 12 keV resolution with the dual energy window correction, and 12 keV resolution with the direct ML-EM correction. Because the modified ML-EM code did not include collimator compensation, all images were reconstructed without including the collimator response. Figure 6.9 shows the contrast as a function of lesion size for the four cases. Because the dual window method is a subtraction method, it produces excellent contrast. The ML-EM modification results in contrast levels comparable to approximately 5 or 6 keV energy resolution. Figure 6.10 shows the background noise levels for the four cases. Due to the decreased number of photons, the noise in the scatter-rejected image is greater than that in the 12 keV image. Similarly, the subtraction process leads to a relatively high noise level following dual energy window correction. On the other hand, the direct ML-EM modification offers scatter correction without a severe increase in noise.

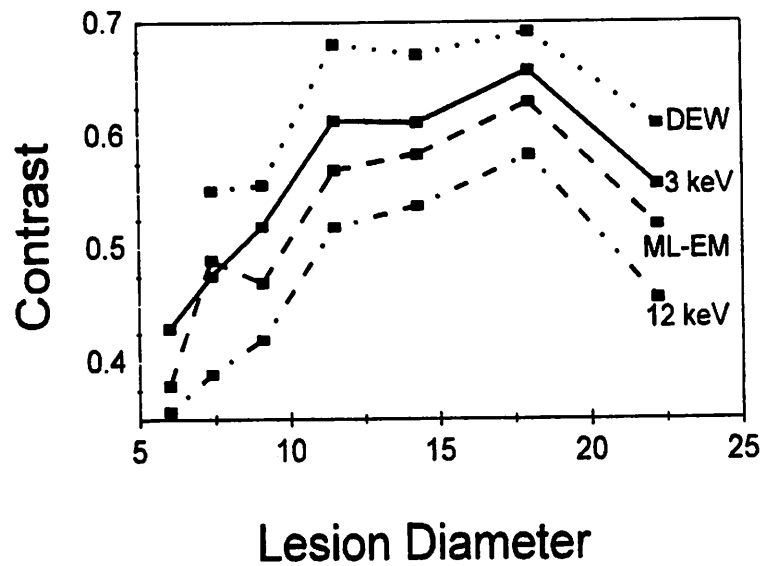


FIGURE 6.9: Contrast as a function of lesion size for both scatter correction and scatter rejection. DEW refers to the dual energy window method; ML-EM refers to scatter correction through modification of the ML-EM algorithm. The 3 keV case corresponds to scatter rejection, and the 12 keV case reflects data that would be obtained with a conventional scintillation camera.

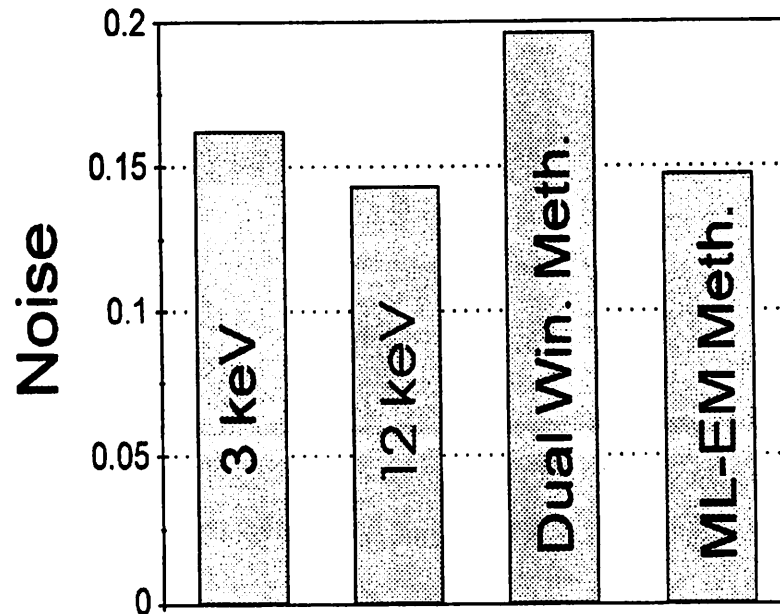


FIGURE 6.10: Background noise levels corresponding to scatter correction and scatter rejection. The noise level is defined as the fractional standard deviation of the activity in the background region between the lesions.

6.4 Discussion

Due to the small size of the ETCT system, the experimental results are limited to 20 cm diameter phantoms. The simulation results of the last chapter extend the consideration of scatter to larger objects. Thus, the combination of experimental and simulation work has considered a range of typical SPECT geometries. The results lead to several conclusions about the role of scatter in relation to other perturbations in SPECT imaging. First, attenuation is clearly the largest error in quantitative SPECT measurements. Next, the diverging field-of-view of the collimator is the primary determinant of contrast and spatial resolution for small objects. Thus, the use of attenuation correction and collimator compensation algorithms is necessary if one hopes to gain any advantage by improving the energy resolution of SPECT systems. In addition, unrestrained improvement of the energy resolution

is not beneficial. At some point, the statistical uncertainty overwhelms the quantitative error due to scatter. For the rather typical geometries and count densities considered here, a resolution of several keV appears sufficient. Finally, scatter-correction techniques can approach the performance of scatter-rejection methods with better image noise performance.

The results also have practical implications for the development of the ETCT system. First, the 4 keV energy resolution of the triple-mode chip is sufficient for most applications. In addition, the use of Cd(Zn)Te rather than HPGe does not represent a large sacrifice in performance in terms of energy resolution.

The analyses presented here are clearly application-specific. For example, a SPECT tumor dosimetry study might use a large ROI that encompasses the entire tumor volume. In this case, the statistical uncertainty of the measurement can be quite low, and there may be some advantage to further improvement of the energy resolution. In addition, the effective size of the patient varies according to the part of the body being imaged and with the photon energy of interest. The PSF analysis shows that there is a benefit to improving the energy resolution as the size scale of the problem increases. Next, the myocardial simulations considered the case of high activity in regions of lower background. In certain circumstances, the region of interest may actually exhibit lower activity than surrounding areas. For example, heart images made with ^{99m}Tc -teboroxime exhibit extremely high liver uptake [81]. If an ROI lies close to the liver, improved energy resolution may prove beneficial to reject scatter from the liver which would otherwise contaminate measurements of myocardial activity.

Chapter 7

Conclusion

This thesis project has led to a number of contributions in the areas of electronics design, detector development, and image analysis for emission-transmission imaging. Yet, all research leads to new questions and motivates new inquiries. This chapter summarizes the key contributions and discusses possibilities for future work.

7.1 Results

The key contribution in the area of electronics design is the conceptualization, implementation, and evaluation of the “triple-mode” architecture, which provides the flexibility of optimized x-ray and radionuclide data acquisition with a relatively small number of circuit blocks. The IC implementation demonstrated that CMOS technology can provide the desired flexibility at a reasonable cost with modest area and power requirements. Although the noise level of the prototype was higher than desired, the performance is adequate for most applications of the ETCT system. In addition, the increased noise can be attributed to the layout of the entire system; it does not represent a fundamental limit of IC technology.

In the area of detector development, CdTe and CZT have been analyzed extensively. The use of these detectors in the ETCT system will most likely prohibit fast pulse-counting; however, this sacrifice will be tolerable if current-mode operation is implemented. The most serious drawback of these materials is the low photoppeak efficiency due to charge trapping. Thus, several methods have been proposed to overcome the trapping problem. Singular value decomposition represents a software approach. Alternatively, a dual time constant method offers real-time correction of spectra. Although these methods work well, the best way to reduce charge trapping is to modify the device geometry. A flexible model has been developed to predict the performance of devices with small anodes. The results indicate that such devices may yield acceptable performance for the ETCT system.

The role of scatter in quantitative SPECT measurements has been extensively considered. These results indicate that in many typical cases, scatter represents a secondary error in comparison to attenuation and collimator blur. Also, the statistical uncertainty overwhelms the scatter error as the energy resolution is improved beyond several keV. In addition, scatter-correction techniques can approach the performance of scatter-rejection methods with better image noise properties. One practical implication of these results is that the energy-resolution capabilities of the triple-mode chip and of Cd(Zn)Te detectors are adequate for many applications of the ETCT system.

7.2 Future Work

Further work is necessary in order to develop an "off-the-shelf" multi-channel triple mode IC. In particular, the next design must include careful consideration

of grounding and packaging issues in order to ensure robust performance. Alternatively, a different architecture can be considered. For example, a charge-sensing sigma-delta converter under development at UC Berkeley offers the advantage of combined pulse-counting and current-mode operation coupled with inherent digitization of the detector signal [82].

The fact that scatter is a relatively small perturbation in SPECT measurements calls into question the utility of the triple-mode chip. Although originally developed for excellent scatter rejection, the chip may prove truly valuable due to the combination of pulse-counting and current-mode capabilities; it is this combination that may ultimately permit the use of Cd(Zn)Te in the ETCT system. Aside from the ETCT system, there are several potential applications of the triple-mode approach. For example, active-passive CT of waste barrels combines high-energy x-ray CT with SPECT reconstruction of the barrel contents [83]. The large size and high density of the barrels leads to a large scatter fraction; in addition, spectroscopic techniques are used to identify unknown contents. Thus, excellent energy resolution is desirable. Another possible application is extended monitoring of radiopharmaceuticals [84]. Quality-control procedures require measurements of doses ranging from several μCi to a few Ci. While the high-level measurement mandates current-mode operation, the low-level measurement requires pulse-counting.

Future detector development demands further analysis of the small-anode effect and investigation of the behavior of thick detectors. Also, the trapping correction techniques should be optimized. Since the original presentation of the dual time-constant sampling technique, one group has tested the method extensively for use in large-volume spectrometers [85]; the results are encouraging. More importantly, careful analysis of material properties is needed. The connection of material proper-

ties to detector performance must be determined in order to truly gauge the limits of these devices.

Further analysis of the role of scatter in SPECT is also worthwhile. For example, a receiver operator characteristic (ROC) study of scatter rejection would provide an interesting validation of this thesis research. In addition, specialized geometries should be studied. For example, high-resolution bone imaging may demand excellent energy resolution due to the presence of dense scattering material in the region of interest. Similarly, precise measurement of the scattering distribution in radionuclide imaging of the breast may yield valuable information about tissue composition.

All in all, an ETCT prototype built around Cd(Zn)Te detectors and flexible IC electronics would offer both a practical implementation and unique capabilities for highly accurate laboratory SPECT measurements.

Appendix A

Publications

Portions of this thesis research are discussed in the following publications:

- [A.1] J.A. Heanue, J.K. Brown, and B.H. Hasegawa, "Two-dimensional modeling of compound semiconductor strip detectors," in preparation for submission to *IEEE Trans. Nucl. Sci.*, 1996.
- [A.2] J.A. Heanue, J.K. Brown, K. Kalki, and B.H. Hasegawa, "The relative importance of energy resolution for quantitative ^{99m}Tc SPECT imaging," accepted for publication in *IEEE Trans. Nucl. Sci.*, 1996.
- [A.3] J.A. Heanue, J.K. Brown, and B.H. Hasegawa, "The use of CdTe or CdZnTe for pulse-counting and current-mode medical imaging applications," accepted for publication in *Nucl. Instr. Meth. A*, 1996.
- [A.4] J.A. Heanue, J.K. Brown, H.R. Tang, and B.H. Hasegawa, "A bound on the energy resolution required for quantitative SPECT," *Med. Phys.*, vol. 23, pp. 169-173, 1996.
- [A.5] J.A. Heanue, B.E. Boser, and B.H. Hasegawa, "CMOS detector readout electronics for an emission-transmission medical imaging system," *IEEE Trans. Nucl. Sci.*, vol. 42, pp. 1133-1138, 1995.
- [A.6] J.A. Heanue, B.E. Boser, K. Kalki, B.H. Hasegawa, J.K. Brown, X. Wu, and C. Cann, "An emission-transmission computed tomography system for correlated SPECT and x-ray CT," in *The Proceedings of the Frontiers in Medical Physics Conference*, La Jolla, CA 1993.

- [A.7] J.A. Heanue. "CMOS Readout Electronics for an Emission-Transmission Medical Imaging System". M.S. Report, The University of California at Berkeley. 1993.
- [A.8] P.R. Bennett, K.S. Shah, M.R. Squillante, J.A. Heanue, and B.H. Hasegawa. "Evaluation of CdTe for use in a prototype emission-transmission CT imaging system," accepted for publication in *IEEE Trans. Nucl. Sci.*, 1996.
- [A.9] B.H. Hasegawa, J.K. Brown, K. Kalki, J.A. Heanue, S. Blankespoor, X. Wu, H.R. Tang, M. Chin, C. Stillson, M. Dae, C.E. Cann, and R.G. Gould. "SPECT-CT: Research and development," accepted for publication in *Physica Medica*. 1996.
- [A.10] J.K. Brown, K. Kalki, J.A. Heanue, and B.H. Hasegawa. "Quantitative SPECT reconstruction using multiray projection integrators," in *The Proceedings of the IEEE Nuclear Science Symposium and Medical Imaging Conference*. San Francisco, 1995.
- [A.11] K. Kalki, J.K. Brown, S.C. Blankespoor, J.A. Heanue, X. Wu, C. Cann, B.H. Hasegawa, M. Chin, C.A. Stillson, M.W. Dae, J.M. Carver. "A combined SPECT and x-ray CT medical imaging system," *Proc. SPIE*, vol. 2432, pp. 367-375, 1995.
- [A.12] S.C. Blankespoor, B.H. Hasegawa, J.K. Brown, J.A. Heanue, R.G. Gould, C.E. Cann, and M.W. Dae, "Development of an emission-transmission CT system combining x-ray CT and SPECT", *Proceedings of the 1994 IEEE Nuclear Science Symposium and Medical Imaging Conference*, vol. 4, pp. 1758-1761. 1994.

Bibliography

- [1] E. Kramer and M. Noz, "CT-SPECT fusion for analysis of radiolabelled antibodies: applications in gastrointestinal and lung carcinoma." *Int. J. Radiation Appl. Instr. B: Nucl Med Biol*, vol. 18, pp. 27-42, 1991.
- [2] B. Tsui, G. Gullberg, E. Edgerton, J. Ballard, J. Perry, W. McCartney, and J. Berg, "Correction of nonuniform attenuation in SPECT imaging," *J. Nucl. Med.*, vol. 30, pp. 497-507, 1989.
- [3] D. Levin, C. Pelizzari, G. Chen, C. Chen, and M. Cooper, "Retrospective geometric correlation of MR, CT, and PET images," *Radiology*, vol. 169, pp. 817-823, 1988.
- [4] S. Webb, *The Physics of Medical Imaging*. Adam Hilger, Philadelphia, 1988.
- [5] M. Rosenthal, J. Cullom, W. Hawkins, S. Moore, B. Tsui, and M. Yester. "Quantitative SPECT imaging: a review and recommendations by the focus committee of the Society of Nuclear Medicine Computer and Instrumentation Council." *J. Nucl. Med.*, vol. 36, pp. 1489-1513, 1995.
- [6] B. Tsui, X. Zhao, E. Frey, and W. McCartney, "Quantitative single-photon emission computed tomography: basics and clinical considerations." *Semin. in Nucl. Med.*, vol. 24, pp. 38-65, 1981.
- [7] B. Hasegawa. Personal communication.
- [8] S. Bellini, M. Piacentini, M. Cafforio, *et al.*, "Compensation of tissue absorption in emission tomography," *IEEE Trans. Acoust., Speech, and Sig. Proc.*, vol. 27, pp. 213-218, 1979.
- [9] L. Chang, "A method for attenuation correction in radionuclide computed tomography," *IEEE Trans. Nucl. Sci.*, vol. 25, pp. 638-643, 1978.
- [10] L. Shepp and Y. Vardi, "Maximum likelihood reconstruction for emission tomography," *IEEE Trans. Med. Imag.*, vol. 1, pp. 113-122, 1982.

- [11] J. Brown, K. Kalki, J. Heanue, and B. Hasegawa, "Quantitative SPECT reconstruction using multiray projection integrators," in *Proceedings of the IEEE Nuclear Science Symposium and Medical Imaging Conference, San Francisco, 1995*.
- [12] C. Pelizzari *et al.*, "Accurate three dimensional registration of CT, PET, and/or MR images of the brain," *J. Comp. Assist. Tomog.*, vol. 89, pp. 20-26, 1989.
- [13] I. Buvat, M. Rodriguez-Villafuerte, A. Todd-Pokropek, H. Benali, and R. Di-Paola, "Comparative assessment of nine scatter correction methods based on spectral analysis using monte carlo simulations," *J. Nucl. Med.*, vol. 36, pp. 1476-1488, 1995.
- [14] R. Jaszczak, C. Floyd, and R. Coleman, "Scatter compensation techniques for SPECT," *IEEE Trans. Nucl. Sci.*, vol. 32, pp. 786-793, 1985.
- [15] F. Beekman, *Fully 3D SPECT Reconstruction with Object Shape Dependent Scatter Compensation*. PhD thesis, Universiteit Utrecht, 1995.
- [16] C. Floyd, R. Jaszczak, K. Greer, and R. Coleman, "Inverse Monte Carlo as an unified reconstruction algorithm for ECT," *J. Nucl. Med.*, vol. 27, pp. 1577-1585, 1986.
- [17] P. Maniawski, H. Morgan, and F. Wackers, "Orbit-related variations in spatial resolution as a source of artifactual defects in thallium-201 SPECT," *J. Nucl. Med.*, vol. 32, pp. 871-875, 1991.
- [18] Z. Cho, J. Jones, and M. Singh, *Foundations of Medical Imaging*. New York: John Wiley & Sons, 1993.
- [19] T. Budinger, "Physical attributes of single-photon tomography," *J. Nucl. Med.*, vol. 21, pp. 579-592, 1980.
- [20] J. Heanue, "CMOS readout electronics for an emission-transmission medical imaging system," Master's thesis, The University of California at Berkeley, 1993.
- [21] F. Fahey, R. Zimmerman, P. Judy, and R. Lanza, "Energy resolution in a high-pressure gas scintillation proportional chamber," *Med. Phy.*, vol. 13, pp. 25-34, 1986.
- [22] T. Newton and D. Potts, eds., *Radiology of the Skull and Brain: Technical Aspects of Computed Tomography*, vol. 5. St. Louis: The C.V. Mosby Company, 1981.

- [23] B. Holman, R. Zimmerman, K. Johnson, P. Carvalho, R. Schwartz, J. Loeffler, E. Alexander, C. Pelizzari, and G. Chen, "Computer-assisted superimposition of magnetic resonance and high-resolution technetium-99m-HMPAO and thallium-201 SPECT imaging of the brain," *J Nucl Med.* vol. 32, pp. 1478-1484, 1991.
- [24] S. Manglos, D. Bassano, and F. Thomas, "Cone-beam transmission tomography for nonuniform attenuation compensation of SPECT images," *J. Nucl. Med.*, vol. 32, pp. 1813-1820, 1991.
- [25] B. Hasegawa, J. Brown, T. Lang, S. Reilly, S. Liew, E. Gingold, and C. Cann, "Object-specific attenuation correction of SPECT with correlated dual-energy x-ray CT," *IEEE Trans. Nucl. Sci.*, 1993.
- [26] B. Hasegawa, E. Gingold, S. Reilly, S. Liew, and C. Cann, "Description of a simultaneous emission-transmission CT system," *Proc. SPIE*, vol. 1213, pp. 50-60, 1990.
- [27] S. Liew and B. Hasegawa, "Noise, resolution, and sensitivity considerations in the design of a single-slice emission-transmission computed tomographic system," *Med. Phys.*, vol. 18, pp. 1002-1015, 1991.
- [28] T. Lang, B. Hasegawa, S. Liew, J. Brown, S. Blankespoor, S. Reilly, E. Gingold, and C. Cann, "Description of a prototype emission transmission computed tomography imaging system," *J. Nucl. Med.*, vol. 33, pp. 1881-1887, 1992.
- [29] B. Hasegawa, B. Stebler, B. Rutt, A. Martinez, E. Gingold, C. Barker, K. Faulkner, C. Cann, and D. Boyd, "A prototype high-purity germanium detector system with fast photon-counting circuitry for medical imaging," *Med. Phys.*, vol. 18, pp. 900-909, 1991.
- [30] K. Kalki, J. Brown, S. Blankespoor, and B. Hasegawa, "Myocardial perfusion imaging with a correlated x-ray CT and SPECT system." submitted to *IEEE Trans. Nucl. Sci.*, 1996.
- [31] Communication from Eurosyst Measures, St. Quentin en Yvelines, France.
- [32] X. Wu, J. Brown, K. Kalki, and B. Hasegawa, "Characterization and correction of pulse pile-up in simultaneous emission-transmission computed tomography." *Med. Phys.*, vol. 23, pp. 569-575, 1996.
- [33] F. Goulding, "Pulse shaping in low-noise nuclear amplifiers: A physical approach to noise analysis," *Nucl. Instr. Meth. A*, vol. 100, pp. 493-504, 1972.
- [34] Z. Chang and W. Sansen, *Low-noise, Wide-band Amplifiers in Bipolar and CMOS Technologies*. Boston: Kluwer Academic Publishers, 1991.

- [35] P. Gray and R. Meyer, "MOS operational amplifier design - a tutorial overview," *IEEE J. Solid State Circ.*, vol. SC-17, pp. 969-982, 1982.
- [36] C. Britton *et al.*, "Design and characterization of the BVX: an 8-channel CMOS preamplifier-shaper for silicon strips," in *Proceedings of the IEEE Nuclear Science Symposium and Medical Imaging Conference, Orlando, 1992*.
- [37] G. Knoll, *Radiation Detection and Measurement*. New York: John Wiley & Sons, 1989.
- [38] "The MOSIS user manual." University of Southern California 1988.
- [39] M. Ismail and T. Fiez, *Analog VLSI: Signal and Information Processing*. McGraw-Hill, New York, 1994.
- [40] D. Binkley, J. Rochelle, M. Paulus, and M. Casey. "A low-noise, wideband, integrated CMOS transimpedance preamplifier for photodiode applications." in *Proc. IEEE 1991 Nucl. Sci. Symp., Santa Fe, 1991*.
- [41] R. Yarema, T. Zimmerman, W. Williams, M. Binkley, T. Huffman, and R. Wagner, "A high-performance multi-channel preamplifier ASIC," in *Proceedings of the 1991 IEEE Nuclear Science Symposium, 1991*.
- [42] E. Beuville, "Low noise front-end integrated circuit specification." User documentation for photodiode readout IC's produced by Lawrence Berkeley National Lab, 1996.
- [43] J. Butler, C. Lingren, and F. Doty, "CdZnTe gamma ray detectors," *IEEE Trans. Nucl. Sci.*, 1991.
- [44] M. Squillante, H. Cole, P. Waer, and G. Entine, "Performance characteristics of CdTe gamma-ray spectrometers," in *Semiconductors for Room-Temperature Radiation Detector Applications* (R. James, T. Schlesinger, P. Siffert, and L. Franks, eds.), vol. 302, Materials Research Society, 1993.
- [45] W. Nelson, H. Hirayama, and D. Rogers, "The EGS4 code system." SLAC Internal Report 265, 1985.
- [46] W. Akutagawa and K. Zanio, "Gamma response of semi-insulating material in the presence of trapping and detrapping," *J. Appl. Phys.*, vol. 40, pp. 3838-3854, 1969.
- [47] K. Shah, J. Lund, and F. Olschner, "Charge collection efficiency in a semiconductor radiation detector with non-constant electric field," *IEEE Trans. Nucl. Sci.*, vol. 37, pp. 183-186, 1990.

- [48] J. Iwanczyk, W. Schnepfle, and M. Masterson, "The effect of charge trapping on the spectrometric performance of HgI₂ gamma-ray detectors," *Nucl. Instr. Meth. A*, vol. 322, pp. 421-426, 1992.
- [49] H. Barrett, J. Eskin, and H. Barber, "Charge transport in arrays of semiconductor gamma-ray detectors," *Phys. Rev. Lett.*, vol. 75, pp. 156-159, 1995.
- [50] Y. Eisen, "Current state-of-the-art applications utilizing CdTe detectors," *Nucl. Instr. Meth. A*, vol. 322, pp. 596-603, 1992.
- [51] M. Squillante, J. Zhang, C. Zhou, P. Bennett, and L. Moy, "New compound semiconductor materials for nuclear detectors," in *Semiconductors for Room-Temperature Radiation Detector Applications* (R. James, T. Schlesinger, P. Siefert, and L. Franks, eds.), vol. 302, Materials Research Society, 1993.
- [52] K. Shah, Radiation Monitoring Devices, personal communication.
- [53] F. Casali *et al.*, "Characterization of small CdTe detectors to be used for linear and matrix arrays," in *Proceedings of the 1991 IEEE Nuclear Science Symposium, Santa Fe, NM*, 1991.
- [54] A. Kojima, M. Matsumoto, M. Takahashi, and S. Uehara, "Effect of energy resolution on scatter fraction in scintigraphic imaging: Monte Carlo study," *Med. Phys.*, vol. 20, pp. 1107-1113, 1993.
- [55] Product literature from DigiRad Corporation, San Diego, CA.
- [56] M. Martini and T. McMath, "Trapping and detrapping effects in lithium-drifted germanium and silicon detectors," *Nucl. Instr. Meth. A*, vol. 79, pp. 259-276, 1970.
- [57] G. Baldazzi *et al.*, "Front-end and signal conditioning electronics for a high-energy ct system using CdZnTe detectors," in *Proceedings of the IEEE Nuclear Science Symposium, Norfolk, VA*, 1994.
- [58] J. Lund, Personal communication.
- [59] R. Kurz, "A novel pulse processing system for HgI₂ detectors," *Nucl. Instr. Meth. A*, vol. 150, pp. 91-95, 1978.
- [60] J. Eskin, H. Barrett, and H. Barber, "Recovery of spectral information from an imperfect detector using the expectation-maximization algorithm," in *Proceedings of the IEEE Nucl. Science Symposium, Arlington, VA*, 1994.
- [61] W. Menke, *Geophysical Data Analysis: Discrete Inverse Theory*. Academic Press, San Diego, 1989.

- [62] M. Finger, T. Prince, L. Padgett, B. Prickett, and W. Schnepfle, "Energy resolution enhancement of mercuric iodide detectors," *IEEE Trans. Nucl. Sci.* vol. 31, pp. 348-352, 1984.
- [63] P. Bennett, K. Shah, J. Heame, and B. Hasegawa, "Evaluation of CdTe for a prototype emission-transmission CT imaging system," in *Proceedings of the IEEE Nuclear Science Symposium, San Francisco*, 1995.
- [64] L. Hamel and S. Paquet, "Charge transport and signal generation in CdTe pixel detectors." Submitted to *Nucl. Instr. Meth. A*, 1996.
- [65] Z. He, "Potential distribution within semiconductor detectors using coplanar electrodes." Submitted to *Nucl. Instr. Meth. A*, 1996.
- [66] P. Luke, "Unipolar charge sensing with coplanar electrodes - application to semiconductor detectors," *IEEE Trans. Nucl. Sci.*, pp. 207-213, 1995.
- [67] J. Eskin, H. Barrett, H. Barber, and J. Woolfenden, "The effect of pixel geometry on spatial and spectral resolution in a CdZnTe imaging array," *IEEE Trans. Nucl. Sci.*, 1996.
- [68] T. Itoh and R. Mittra, "Spectral-domain approach for calculating the dispersion characteristics of microstrip lines," *IEEE Trans. MTT*, vol. 21, pp. 496-499, 1973.
- [69] T. Itoh and A. Hebert, "A generalized spectral domain analysis for coupled suspended microstriplines with tuning septums," *IEEE Trans. MTT*, vol. 26, pp. 820-826, 1978.
- [70] W. Shockley, "Currents to conductors induced by moving point charge." *J. Appl. Phys.*, vol. 9, pp. 635-636, 1938.
- [71] S. Ramo, "Currents induced by electron motion," *Proc. IRE*, vol. 27, pp. 584-585, 1939.
- [72] E. Yamashita and R. Mittra, "Variational method for the analysis of microstrip lines," *IEEE Trans. MTT*, vol. 15, pp. 251-256, 1968.
- [73] L. Hamel, "Signal induced in semiconductor detectors with a linear field profile in the presence of trapping and detrapping." Submitted to *Nucl. Instr. Meth. A*, 1995.
- [74] J. Beck, R. Jaszczak, R. Coleman, C. Starmer, and L. Nolte, "Analysis of SPECT including scatter and attenuation using sophisticated Monte Carlo modeling methods," *IEEE Trans. Nucl. Sci.* vol. 29, pp. 506-511, 1982.

- [75] C. Floyd, R. Jaszczak, C. Harris, and R. Coleman, "Energy and spatial distribution of multiple order Compton scatter in SPECT: a Monte Carlo investigation." *Phys. Med. Biol.*, vol. 29, pp. 1217–1230, 1984.
- [76] S. Pang and S. Genna, "The effect of Compton scattered photons on emission computerized transaxial tomography," *IEEE Trans. Nucl. Sci.*, vol. 26, pp. 2772–2774, 1979.
- [77] V. Wirth, "Effective energy resolution and scatter rejection in nuclear medicine," *Phys. Med. Biol.*, vol. 34, pp. 85–90, 1989.
- [78] R. Evans, *The Atomic Nucleus*. McGraw Hill, New York, 1982.
- [79] K. Brownlee, *Statistical Theory and Methodology*. Wiley, New York, 1965.
- [80] D. Politte and D. Snyder, "Corrections for accidental coincidences and attenuation in maximum-likelihood reconstruction for positron-emission tomography." *IEEE Trans. Med. Imag.*, vol. 10, pp. 82–89, 1991.
- [81] J. Nuyts, P. Dupont, V. Maegdenbergh, S. Vleugels, P. Suetens, and L. Mortelmans, "A study of the liver-heart artifact in emission tomography," *J. Nucl. Med.*, vol. 36, pp. 133–139, 1995.
- [82] C. Boles, B. Boser, and S. Butala. Personal communication.
- [83] H. Martz *et al.*, "Quantitative waste assay using gamma-ray spectrometry and computed tomography," in *Proc. 14th European Safeguards Research and Development Assoc., Salamanca, Spain*, 1992.
- [84] S. Prussin, S. Lane, D. Kania, S. Han, J. Trebes, H. Spracklen, H. Moore, K. Burkes, and W. Porter, "An instrumented shield system for calibration of technetium-99m," *J. Nucl. Med. Technol.*, vol. 23, pp. 202–208, 1995.
- [85] J. Lund, R. James, J. Van Scyoc, and R. Olsen, "The use of pulse processing techniques to improve the performance of CdZnTe gamma-ray spectrometers." Submitted to *IEEE Trans. Nucl. Sci.*, 1996.